EUROPEAN RESPIRATORY *journal*

FLAGSHIP SCIENTIFIC JOURNAL OF ERS

Early View

Original research article

Human lungs show limited permissiveness for SARS-CoV-2 due to scarce ACE2 levels but virus-induced expansion of inflammatory macrophages

Katja Hönzke, Benedikt Obermayer, Christin Mache, Diana Fathykova, Mirjana Kessler, Simon Dökel, Emanuel Wyler, Morris Baumgardt, Anna Löwa, Karen Hoffmann, Patrick Graff, Jessica Schulze, Maren Mieth, Katharina Hellwig, Zeynep Demir, Barbara Biere, Linda Brunotte, Angeles Mecate-Zambrano, Judith Bushe, Melanie Dohmen, Christian Hinze, Sefer Elezkurtaj, Mario Tönnies, Torsten T. Bauer, Stephan Eggeling, Hong-Linh Tran, Paul Schneider, Jens Neudecker, Jens C. Rückert, Kai M. Schmidt-Ott, Jonas Busch, Frederick Klauschen, David Horst, Helena Radbruch, Josefine Radke, Frank Heppner, Victor M. Corman, Daniela Niemeyer, Marcel A. Müller, Christine Goffinet, Ronja Mothes, Anna Pascual-Reguant, Anja Erika Hauser, Dieter Beule, Markus Landthaler, Stephan Ludwig, Norbert Suttorp, Martin Witzenrath, Achim D. Gruber, Christian Drosten, Leif-Erik Sander, Thorsten Wolff, Stefan Hippenstiel, Andreas C. Hocke

Please cite this article as: Hönzke K, Obermayer B, Mache C, *et al*. Human lungs show limited permissiveness for SARS-CoV-2 due to scarce ACE2 levels but virus-induced expansion of inflammatory macrophages. *Eur Respir J* 2022; in press (https://doi.org/10.1183/13993003.02725-2021).

Human lungs show limited permissiveness for SARS-CoV-2 due to scarce ACE2 levels but virus-induced expansion of inflammatory macrophages

Katja Hönzke[1§], Benedikt Obermayer[2§], Christin Mache[3§], Diana Fathykova[1], Mirjana Kessler[1,4], Simon Dökel[5], Emanuel Wyler[6], Morris Baumgardt[1], Anna Löwa[1], Karen Hoffmann[1], Patrick Graff[1], Jessica Schulze[3], Maren Mieth[1], Katharina Hellwig[1], Zeynep Demir[1], Barbara Biere[3], Linda Brunotte[7], Angeles Mecate-Zambrano[7], Judith Bushe[5], Melanie Dohmen[1,9], Christian Hinze[8,9], Sefer Elezkurtaj[10], Mario Tönnies[11], Torsten T. Bauer[11], Stephan Eggeling[12], Hong-Linh Tran[12], Paul Schneider[13], Jens Neudecker[14], Jens C. Rückert[14], Kai M. Schmidt-Ott[8,9], Jonas Busch[15], Frederick Klauschen[10], David Horst[10], Helena Radbruch[16], Josefine Radke[16], Frank Heppner[16], Victor M. Corman[17], Daniela Niemeyer[17], Marcel A. Müller[17], Christine Goffinet[17], Ronja Mothes[18,19], Anna Pascual-Reguant[18,19], Anja Erika Hauser[18,19], Dieter Beule[2], Markus Landthaler[6], Stephan Ludwig[7], Norbert Suttorp[1], Martin Witzenrath[1], Achim D. Gruber[5], Christian Drosten[17], Leif-Erik Sander[1], Thorsten Wolff[3], Stefan Hippenstiel[1], Andreas C. Hocke[1]

[§] contributed equally

[1] Department of Infectious Diseases and Respiratory Medicine, Charité - Universitätsmedizin Berlin, corporate member of Freie Universität Berlin, Humboldt-Universität zu Berlin, and Berlin Institute of Health, Berlin, Germany.

[2] Berlin Institute of Health at Charité – Universitätsmedizin Berlin, Core Unit Bioinformatics, Charitéplatz 1, 10117 Berlin, Germany.

[3] Unit 17 "Influenza and other Respiratory Viruses", Robert Koch Institut, Berlin, Germany.

[4] Department of Gynecology and Obstetrics, Ludwig-Maximilian University, Munich, Germany

[5] Department of Veterinary Pathology, Freie Universität Berlin, Berlin, Germany.

[6] Berlin Institute for Medical Systems Biology (BIMSB), Max Delbrück Center for Molecular Medicine in the Helmholtz Association (MDC) and IRI Life Sciences, Institute for Biology, Humboldt Universität zu Berlin, Berlin, Germany.

[7] Institute of Virology, Westfaelische Wilhelms Universität, Münster, Nordrhein-Westfalen, Germany.

[8] Department of Nephrology and Medical Intensive Care, Charité - Universitätsmedizin Berlin, corporate member of Freie Universität Berlin, Humboldt-Universität zu Berlin, and Berlin Institute of Health, Berlin, Germany.

[9] Max Delbrück Center for Molecular Medicine in the Helmholtz Association, Berlin, Germany.
[10] Department of Pathology, Charité - Universitätsmedizin Berlin, corporate member of Freie Universität Berlin, Humboldt-Universität zu Berlin, and Berlin Institute of Health, Berlin, Germany.
[11] HELIOS Clinic Emil von Behring, Department of Pneumology and Department of Thoracic Surgery, Chest Hospital Heckeshorn, Berlin, Germany.
[12] Department of Thoracic Surgery, Vivantes Clinics Neukölln, Berlin, Germany
[13] Department for Thoracic Surgery, DRK Clinics, Berlin, Germany.
[14] Department of General, Visceral, Vascular and Thoracic Surgery, Charité - Universitätsmedizin Berlin, corporate member of Freie Universität Berlin, Humboldt-Universität zu Berlin, and Berlin Institute of Health, Berlin, Germany.
[15] Clinic for Urology, Charité - Universitätsmedizin Berlin, corporate member of Freie Universität Berlin, Humboldt-Universität zu Berlin, and Berlin Institute of Health, Berlin, Germany.
[16] Institute for Neuropathology, Charité - Universitätsmedizin Berlin, corporate member of Freie Universität Berlin, Humboldt-Universität zu Berlin, and Berlin Institute of Health, Berlin, Germany.
[17] Institute of Virology, Charité - Universitätsmedizin Berlin, corporate member of Freie Universität Berlin, Humboldt-Universität zu Berlin, and Berlin Institute of Health, Berlin, Germany.
[18] Department of Rheumatology and Clinical Immunology, Charité - Universitätsmedizin Berlin, corporate member of Freie Universität Berlin and Humboldt-Universität zu Berlin, 10117 Berlin, Germany.
[19] Deutsches Rheuma-Forschungszentrum (DRFZ), a Leibniz Institute, Charitéplatz 1, 10117 Berlin, Germany

Correspondence: Andreas C. Hocke, MD; Charité - Universitätsmedizin Berlin, Department of Infectious Diseases and Respiratory Medicine, Charitéplatz 1, 10117 Berlin, Germany.
Phone: +49 (0)30 450 553 477; Email: andreas.hocke@charite.de

Shareable abstract

Scarce ACE2 expression limits alveolar SARS-CoV-2 permissiveness and related tissue damage. Instead, non-productive virus uptake by alveolar macrophages leads to a specific pulmonary immune activation. COVID-19 ARDS is most likely caused by immunopathogenesis rather than alveolar viral damage.

Abstract

Background SARS-CoV-2 utilizes the ACE2 transmembrane peptidase as cellular entry receptor. However, whether SARS-CoV-2 in the alveolar compartment is strictly ACE2-dependent and to what extent virus-induced tissue damage and/or direct immune activation determines early pathogenesis is still elusive.

Methods Spectral microscopy, single-cell/-nucleus RNA sequencing or ACE2 'gain-of-function' experiments were applied on infected human lung explants and adult stem cell-derived human lung organoids to correlate ACE2 and related host factors with SARS-CoV-2 tropism, propagation, virulence and immune activation compared to SARS-CoV, influenza and MERS-CoV. COVID-19 autopsy material was used to validate *ex vivo* results.

Results We provide evidence that alveolar ACE2 expression must be considered scarce, thereby limiting SARS-CoV-2 propagation and virus-induced tissue damage in the human alveolus. Instead, *ex vivo* infected human lungs and COVID-19 autopsy samples showed that alveolar macrophages were frequently positive for SARS-CoV-2. Single-cell/-nucleus transcriptomics further revealed non-productive virus uptake and a related inflammatory and anti-viral activation, especially in 'inflammatory alveolar macrophages', comparable to those induced by SARS-CoV and MERS-CoV but different from NL63 or influenza virus infection.

Conclusions Collectively, our findings indicate that severe lung injury in COVID-19 likely results from a macrophage triggered immune activation rather than direct viral damage of the alveolar compartment.

Introduction

Coronavirus disease 2019 (COVID-19) is caused by the severe acute respiratory syndrome coronavirus 2 (SARS-CoV-2). Depending on the virus variant, approximately 22 % of COVID-19 patients develop severe disease with a high risk of acute respiratory distress syndrome (ARDS) [1-5], which may be heterogeneous and differ from classical ARDS [6]. Both, SARS-CoV-2 and SARS-CoV use angiotensin-converting enzyme 2 (ACE2) as primary cellular entry receptor [7, 8]. However, it remains still elusive to which extent ACE2 contributes to alveolar pathogenesis which may result in subsequent lung failure. Thus, the actual role of ACE2 in COVID-19 pathogenesis is still a matter of debate [9-11]. While some studies suggested relatively high or induced ACE2 expression under healthy or pulmonary diseased conditions [12-18] others suggest relatively low, cell type-limited ACE2 expression in the alveolus [11, 14, 19-21]. This is complicated by the fact that some of these studies solely focus on *ACE2* mRNA analyses which might differ to the actual ACE2 protein expression level [11, 20, 22-24]. Consequently, to gain deeper insight into COVID-19 pathogenesis, further rigorous analyses of tissue- and cell type-specific ACE2 mRNA and protein expression in the context of SARS-CoV-2 tropism, replication and resulting tissue damage and/or induced immune response in the early phase of infection are required.

Similarly, there is still inconsistency about the actual SARS-CoV-2 tropism as well as replication efficacy in the human alveolar compartment and a debate if and to what extent alveolar epithelial type 1 (AT1), type 2 cells (AT2) or alveolar macrophages (AM) become productively infected and contribute to tissue pathology [20, 25-27]. Although it appears obvious that alveolar ACE2 is present and viral infection of alveolar cells occurs, it is critical to elucidate the role of direct infection versus indirect immunopathology in the pathogenesis of COVID-19 ARDS. Of note, some clinical trials demonstrated beneficial effects of dexamethasone in severe COVID-19, suggesting immune-related instead of direct viral replication-associated lung damage [28-31].

Therefore, we aimed at elucidating ACE2 dependency for alveolar SARS-CoV-2 tropism, productive infection, replication rate, tissue damage, and immune activation across cells of the alveolar space. By several independent methods using *ex vivo* infected human lung tissue, COVID-19 autopsy material and adult stem cell derived human lung organoids, we demonstrate scarce ACE2 mRNA and protein expression restricted to AT2 cells without statistically significant induction of ACE2 protein by interferon (IFN). Accordingly, SARS-CoV and SARS-CoV-2 propagated consistently less efficient compared to influenza (IAV) and MERS-CoV in human lung tissue. ACE2 overexpression in human lungs broadens SARS-CoV-2 tropism as well as tissue damage, similar to MERS-CoV. SARS-CoV-2 is predominantly endocytosed by AM leading to an expansion of inflammatory AM in human lung explants and COVID-19 autopsy lungs resulting in a coronavirus specific inflammatory and anti-viral gene expression signature.

Methods

Detailed information is outlined in the online supplement.

Used models

For *ex vivo* infection of human lung tissue samples fresh lung explants were obtained from 25 patients suffering from lung carcinoma (1 case metastatic osteo-sarcoma), who underwent lung resection at local thoracic surgeries. Lung explants from healthy patients were obtained from the International Institute for the Advancement of Medicine (IIAM, Edison, NJ). Clinical data of donors are included in Table S1 (ethics approval Charité EA2/079/13 and Ärztekammer Westfalen-Lippe AZ: 2016-265-f-S). Primary AM were isolated by repeated perfusion of the human explant lungs. For the alveolar and bronchial organoids, primary cells were isolated from non-cancerous (normal) parts of distal lung tissue obtained from lung cancer patients undergoing tumor resection surgery. Kidney tissue was collected from tumor nephrectomies (ethics approval EA4/026/18). Autopsy material was included from 25 cases of patients that had died after COVID-19 disease. Autopsies were performed on the legal basis of §1 SRegG BE of the autopsy act of Berlin and §25(4) of the German Infection Protection Act. This study was approved by the Ethics Committee of the Charité (EA 1/144/13 and EA2/066/20) as well as by the Charité-BIH COVID-19 research board and was in compliance with the Declaration of Helsinki.

Virus strains

Infection experiments were carried out by two independent laboratories in Berlin (Robert Koch Institute and Charité) and Muenster (Wilhelms-University in Muenster). For infection experiments SARS-CoV-2 (Munich 929 or BavPart1) [7], rSARS-CoV (generated in the Drosten Lab by reverse genetics based on the SARS-CoV Frankfurt-1 strain, Accession Number FJ429166.1 [32]), SARS-CoV-2 FI-200 isolate strain, rMERS-CoV (generated in the Drosten Lab by reverse genetics based on the MERS-CoV strain EMC/2012, Accession Number JX869059 [33]), HCoV-NL63 and the human seasonal influenza H3N2 virus A/Panama/2007/1999 (Pan/99[H3N2]) (further referred to IAV) strain were used.

Infection experiments and infectious particle quantification

Calu-3 cells were either mock-infected with infection medium or challenged with SARS-CoV-2, rSARS-CoV, rMERS-CoV or IAV (MOI 0.1). Lung tissue cultures were inoculated with control medium or SARS-CoV-2, rSARS-CoV, rMERS-CoV or IAV. Samples. Mature human lung organoids were collected, broken up and organoid fragments were either mock-infected or challenged with SARS-CoV-2. AM were infected with control medium, SARS-CoV-2 or hCoV-NL63. Samples were taken at the indicated time points.

IFN stimulation of lung tissue

Culture medium containing recombinant human IFNβ (100 U/ml) was injected into lung explants. The tissue was processed for RNA and protein analysis after additional 24 h or 96 h.

Bulk RNA sequencing and analysis

RNA from infected samples was purified. PolyA(+) RNA sequencing libraries were constructed using the NEBNext Ultra™ II Directional RNA Library Prep Kit for Illumina (New England Biolabs) according to the manufacturer's instruction and sequenced on a Nextseq 500 device using 1 x 76 cycles single-end sequencing.

Single-cell isolation and library preparation

Single cells from individual human lung tissue samples were isolated. AM were detached using a cell scraper. The single-cell capturing and downstream library constructions were performed using the Chromium Single Cell 3′ V3.1 library preparation kit according to the manufacturer's protocol (10x Genomics). The constructed libraries were either sequenced on the Nextseq 500 using 28 cycles for read 1.55 cycles for read 2, and 8 index cycles, or on the Novaseq 6000 S1 using 28 cycles for read 1.64 cycles for read 2, and 8 index cycles, to a median depth of 36000 reads per cell.

Single-nucleus isolation and library preparation

Single nuclei were isolated from snap-frozen autopsy samples as described before [34].

In situ hybridization

For RNA *in situ* hybridization (ISH), tissues were immersion fixed and embedded in paraffin. ISH for the detection of SARS-CoV-2 and MERS-CoV was performed using the ViewRNA ISH Tissue Assay (Invitrogen by Thermo Fisher Scientific) following the manufacturer's instructions (MAN0018633 Rev.C.0) as described [35].

Image segmentation

From each COVID-19 (n = 4) and NON-COVID-19 (n = 4) HE-stained tissue slide, two regions of interest (15,000 x 15,000 and 20,000 x 20,000 pixel / 19,360,000 µm^2 and 10,890,000 µm^2, in total 30.25 mm^2) were extracted and the number of cell nuclei was determined. Cell nuclei were separated from background by manual thresholding of hue and brightness channels in an HSB representation of the colored microscopy images. Cell nuclei were separated from each other by morphological filtering and distance transform watershed using the MorphoLibJ-Plugin [36] of Fiji [37].

Results

ACE2 is scarcely expressed in the human alveolar compartment

ACE2, transmembrane protease serine subtype 2 (TMPRSS2), furin and further host factors are considered as determinants of SARS-CoV-2 cellular entry and infection [7, 38]. To quantify their expression across alveolar space, we performed single-cell (scSeq) and single-nucleus RNA sequencing (snSeq) of human lung tissue samples (6 donors) and COVID-19 autopsy lungs (2 donors) (Figure 1A, Table S1 and S2) and annotated cell clusters (Figure 1B, Figure S1A and S1B, Table S3) [39]. While *TMPRSS2* was highly expressed in AT1 and AT2 cells, only 3 of 2199 AT2 cells were *ACE2* positive expressing only 1 unique molecular identifier each (Figure 1C) [18, 22, 23]. In contrast, the proposed alternative SARS-CoV-2 receptors *KREMEN1, ASGR1, CD147* (*BSG*) as well as *FURIN* were ubiquitously expressed in human lung explants and in autopsy lungs (Figure 1C) [40-43]. We confirmed this trend for *ACE2*, *BSG*, *TMPRSS2* and *FURIN* by RT-qPCR on bulk RNA of human lung tissue, human lung bronchial organoids as well as Calu-3 cells as positive control (Figure 1D). For ACE2 protein analysis, we evaluated 5 commercial ACE2 antibodies on Calu-3 cells and found the R&D AF933 as most sensitive and specific, which was chosen for further experiments (Figure S1C). Western blot analysis showed very high ACE2 protein amounts in kidneys [44], whereas levels in lung tissue and bronchial organoids were low or undetectable (Figure 1E/long exposure, S1D/short exposure, Table S1). Lung tissue explants obtained from cancer patients were referenced against “normal” lung tissue from transplant donors showing the same low ACE2 protein amounts (Figure S1E).

Since *ACE2* has been identified as an interferon-stimulated gene (ISG) [18, 23], we stimulated lung tissue with IFNβ (Figure 1F and 1G, Table S1). Although RT-qPCR analysis showed approximately 40-fold induction of *ACE2* after 96 h, no upregulation of ACE2 was detected on the protein level. Significant induction was observed for *BSG* and positive control gene *MX1*, but not for *TMPRSS2* or *FURIN* (Figure 1F).

We performed immunostaining and *in situ* hybridization for ACE2 and TMPRSS2 in lung tissue and bronchial organoids to evaluate cell type-specific expression patterns (Figure 2 and S2). In alveoli, ACE2 protein and mRNA expression levels were rather low and nearly undetectable by conventional, threshold based confocal microscopy (Figure S2B). Using spectral imaging and linear unmixing, ACE2 protein and mRNA could be detected in few AT2 cells (approx. 5.6 %) (Figure 2A and S2B, S2D). AT2 cells positive for *ACE2* mRNA did not necessarily exhibit ACE2 surface protein expression. To further demonstrate the importance of antibody evaluation we tested another ACE2 antibody (Thermo PA5-20046) with available blocking peptide (Figure S2C, insets). Immunostaining revealed a similar expression pattern as demonstrated by Hamming et al. with abolishment of the signal by blocking peptide pre-incubation [12]. However, further validation by Western blot revealed an indefinite band pattern completely abolished by blocking peptide indicating abundant, but likely unspecific antibody binding and false positive ACE2 expression in AT1 and AT2 cells in human lung tissue using this antibody. In line with scSeq, *TMPRSS2* was found frequently expressed in AT1 and AT2 cells but was not detected in AM (Figure 2B). Calu-3 cells and kidney served as positive control for *ACE2*, *TMPRSS2* and ACE2 protein expression (Figure S2A).

Scarce ACE2 expression limits SARS-CoV-2 replication, tropism, and tissue damage

In previous studies, we established *ex vivo* cultured human lung tissue as an infection model to assess the virulence of respiratory viruses such as IAV and MERS-CoV [45-47]. Replication of several IAV strains as well as MERS-CoV was observed in this model system, in line with alveolar expression of the corresponding receptors [46, 47]. Therefore, we infected lung tissue (5 donors) with SARS-CoV-2 and compared its replication to IAV, MERS-CoV, and SARS-CoV. We found highly variable and moderate replication for the ACE2-dependent SARS-CoV and SARS-CoV-2, whereas IAV and MERS-CoV replicated more efficiently (Figure 3A, Table S1). An external, independent validation experiment (3 donors) showed a similar kinetic of SARS-CoV-2 in human lung tissue (Figure S3A). We confirmed low replication (4 donors) by increasing the infection dose of SARS-CoV-2 (30-fold) resulting in only a minor increase of SARS-CoV-2 followed by a rapid decline below input, whereas replication of other viruses was similar (Figure 3B, Table S1). Calu-3 cells served as a positive control (Figure 3C).

In order to assess the role of low ACE2 expression in the limited permissiveness of lung tissue for SARS-CoV-2, we compared viral replication in wildtype and ACE2$^+$ human bronchial organoids. ACE2 overexpression led to comparable protein levels as shown for Calu-3 cells and apical ACE2 expression on a subpopulation of bronchial organoid cells (Figure 3D and E). Although *ACE2* mRNA was detectable in almost all organoid cells, apical ACE2 protein was expressed only on a subpopulation of cells (Figure 3E). SARS-CoV-2 S-protein was only observed in ACE2 protein positive bronchial organoid cells (Figure 3E) and only ACE2$^+$ bronchial organoids supported SARS-CoV-2 replication (Figure 3F). We corroborated the relevance of this finding for the permissiveness of lung tissue for SARS-CoV-2 in dependence of ACE2 by investigating human alveolar organoids, which support active replication of SARS-CoV-2 without ACE2 overexpression (Figure 3G). We profiled around 3,000 and 23,000 cells from alveolar and bronchial organoids, respectively, and annotated and quantified the cell type composition (Figure S3B, S3C and S3E). AT2-like cells with constitutive expression of ACE2 (mRNA scSeq and apical protein) were found exclusively in alveolar organoids (Figure 3H and S3D-F). Other relevant host factors such as *KREMEN1*, *ASGR1*, *TMPRSS2*, *FURIN*, *BSG,* and *NRP1* were equally well expressed in both organoid types (Figure S3D). Correspondingly, SARS-CoV-2 RNA could be detected in many cells of alveolar but not bronchial organoids (Fig. 3H and S3E). This is in line with SARS-CoV-2 N-protein detection by immunostaining in ACE2-positive cells of alveolar organoids (Figure 3I). However, ACE2 protein expression is detectable at a very low levels in alveolar organoids but not ACE2$^+$ bronchial organoids (Figure S3F).

Immunostaining and *in situ* hybridization was performed in human lung tissue explants to determine ACE2-dependent SARS-CoV-2 cellular tropism and tissue damage (Figure 4). In line with low alveolar ACE2 expression, we rarely found SARS-CoV-2 infected AT2 cells by complementary methods (*N-gene, S-gene,* N-protein, S-protein labeling) (Figure 4A and B), whereas MERS-CoV showed widespread infection (Figure S4A) [46]. Instead of broad epithelial infection, we frequently detected punctuated staining in AM positive for SARS-CoV-2 (viral RNA, viral proteins) (Figure 4A and B). Mock- and SARS-CoV-2-infected Calu-3 cells served as controls (Figure S4B).

To show that SARS-CoV-2 tropism is limited by ACE2 expression, we overexpressed ACE2 (ACE2$^+$) by adenoviral transduction in the explant tissue and detected strong apical ACE2 expression in AT1 and AT2 cells, endothelial cells, bronchial epithelium, and AM (Figure 4C and S4C). The punctuated staining pattern for SARS-CoV-2 in ACE2$^+$ AM (Figure 4B) changed to a cytosolic pattern comparable to AT2 cells and showed signs of AM apoptosis, indicating productive infection if ACE2 is present in these cell types (Figure 4C). We next investigated whether broadened alveolar ACE2 expression and subsequent SARS-CoV-2 tropism might lead to increased tissue damage by using delinearization and loss of epithelial occludin as surrogate [46]. In early infections (16-24 h) of wildtype and ACE2$^+$ lungs with SARS-CoV-2 and MERS-CoV, infected AT2 cells still showed a linear occludin pattern similar to mock infection (Figure 4D and S4C). In late infection (72 h), the ACE2$^+$ induced a broadened SARS-CoV-2 tropism, increased detachment of infected cells and loss of epithelial occludin, similar to the strong damage pattern of MERS-CoV (Figure 4D) [46].

Ex vivo infected tissue only partially reflects the pathophysiology of lungs in COVID-19 patients. Therefore, we investigated peripheral lung tissue of 25 confirmed COVID-19 autopsy cases by *in situ* hybridization against *N-gene* of SARS-CoV-2 and found just 2 patients (1 of them very moderately) positive for cellular SARS-CoV-2, although 18 of 25 exhibited viral RNA in the lungs (RT-qPCR, Figure 5 and S5) [48]. While 24 patients (P2 - P25) underwent intensive care treatment up to several weeks, 1 case (P1) underwent early death (6 days post diagnosis) after compassionate best supportive care. *In situ* hybridization on P1 lung sections revealed several SARS-CoV-2-positive cells within the alveoli, weaker signs of immune cell infiltration and alveolar epithelial damage (Figure 5A and S5C). Most SARS-CoV-2-positive cells resembled AM as well as some AT2 cells. We found punctuated staining pattern of SARS-CoV-2 S-protein in AM, similar to *ex vivo* infected lungs as well as a strong cytosolic signal in a minor fraction of AT2 cells (Figure 5B). SARS-CoV-2-positive AT2 cells were found to be endocytosed by AM. Similar to scarce ACE2 immunostaining of *ex vivo* lung tissue, ACE2 protein in infected areas of the autopsy lung was even undetectable, compared to highly positive autopsy kidney (same patient, Figure S5D).

SARS-CoV-2 leads to immune activation by induction of inflammatory alveolar macrophages

To further elucidate the impact of SARS-CoV-2 infection in alveoli, we analyzed infected explant and autopsy lungs (Figure 3A, 3B) by bulk RNA sequencing, scSeq, and snSeq (Figure 6, S6, 7, and S7). In line with replication data (plaque assay), we found high levels of viral reads for IAV and MERS-CoV, while SARS-CoV and SARS-CoV-2 RNA were poorly detectable by bulk RNA sequencing on lung explants (Figure S6A) (16 h post infection, equal viral input $1*10^6$ PFU, Figure 3A, Table S1). Analysis of subgenomic viral RNA indicating active replication [49] showed appreciable levels for MERS-CoV but only low levels for SARS-CoV or SARS-CoV-2 (Figure S6A). Infection of explants by SARS-CoV or SARS-CoV-2 resulted in a weak gene expression response (Figure S6B) with very few differentially expressed genes (Figure S6B, Table S4) in bulk transcriptomic data. Specifically, we observed a lack of characteristic anti-viral gene expression signatures or specific IFN response (Figure S6B and S6C), but weak, yet significant, induction of TNFα signaling (Figure S6B, Table S4). No significant change in gene expression for *ACE2, BSG, TMPRSS2,* or *FURIN* was detected (Figure S6C). In contrast, IAV and MERS-CoV infection induced robust and distinguishable transcriptomic responses, e.g.

upregulation of virus response genes such as *OAS1*, *MX1/2* and IFN-related pathways (Figure S6B).

To further dissect SARS-CoV-2 tropism and transcriptional response to infection, we performed scSeq of lungs infected with high virus load for SARS-CoV-2 (Figure 3B, 6 and S6). We combined single-cell data from uninfected control tissue with another 21 samples infected with IAV, MERS-CoV, SARS-CoV ($1*10^6$ PFU each), or SARS-CoV-2 ($30*10^6$ PFU), respectively. Data were integrated with snSeq data of lung autopsy material from 2 acute and 4 prolonged COVID-19 cases (Table S2). Clustering of almost 150,000 cells resulted in a consistent cell type annotation (Figure 6A). In lung explants, viral RNA from IAV and MERS-CoV was found in all cell types, but SARS-CoV and SARS-CoV-2 RNA was detected mainly in AM and a subpopulation of monocytes in line with microscopic analysis of *ex vivo* infected lung tissue and autopsy samples (Figure 6B). The rare detection of SARS-CoV-2 in AT2 cells appeared independent of *ACE2* mRNA expression (Figure 6B) [50].

For snSeq data from autopsy samples, it is challenging to distinguish cytoplasmic viral RNA from background ambient RNA to confidently identify virus-positive cells. Therefore, we compared the fraction of virus-positive cells before and after filtering of ambient RNA (CellBender) [50, 51] and found SARS-CoV-2 viral RNA just in the acute cases and predominantly in AM (Figure 6D). Analysis suggested that viral reads in the autopsy data in cells other than macrophages most likely originated from background RNA. Using filtered data, we consistently identified AM as the predominantly virus-positive cell type both in lung explants and autopsy material (Figure 6C) [50].

We next performed differential gene expression analysis between infected explants or autopsy lungs against respective controls (Table S5). Expression of host factors *ACE2*, *BSG/CD147*, *TMPRSS2,* and *FURIN* remained stable, with consistently low levels of *ACE2* (Figure 6D). Factors such as *NRP1* [52, 53] or *DPP4* [54] showed abundant expression in several lung cell types. In contrast to the bulk RNA sequencing data, we now observed strong induction of inflammatory and antiviral genes in several cell types of the lung explants as well as the acute (virus-positive) autopsy samples (Figure S6F).

Gene set enrichment analysis and summarized gene expression for antiviral and inflammatory pathways (Figure 6E) revealed that *OAS* and *RIG-I* antiviral response, IFN and cytokine signaling, as well as inflammatory response was upregulated in AT2 cells, AM, endothelial cells and fibroblasts as a result of coronavirus infection, whereas the response to IAV for these pathways was more pronounced in monocytes and fibroblasts. Our data show that acute COVID-19 autopsy samples exhibit a related gene expression response to the SARS-CoV-2-infected lung explants (Figure 6E). We finally analyzed intercellular receptor-ligand signaling interactions and their differences between cases and controls and identified regulated signaling between T cells and macrophages in the acute and prolonged autopsy cases (Figure S6H). Next to typical co-stimulatory activation (CD28/CD86), we observed enhanced integrin/TGF as well as downregulated CCL5/CCR1 signaling.

Macrophages showed strong viral uptake in explant and autopsy lungs and are considered to initiate the immune response in COVID-19. Especially the prolonged autopsy samples showed AM expansion, possibly reflecting systemic monocyte/macrophage recruitment in late stages of disease (Figure S6E). Differential gene expression analysis confirmed induction of IFN-stimulated genes both after MERS-CoV and SARS-CoV-2 infection, which, along with SARS-CoV, induced consistent responses in AM (Spearman correlation between the estimated log2 fold changes > 0.69; Figure S6G) differing from IAV-induced gene induction. We aimed to disentangle cell-intrinsic responses to infection from indirect signaling-mediated effects (cloglog regression [55]) to compare virus-positive (infected) against virus-negative (bystander) AM (Figure S6I, Table S6). We observed induction of genes such as *TNFAIP6*, *NFKB1* and *IL1A* as well as downregulation of the canonical AM marker *FABP4* in SARS-CoV-2-positive macrophages. Generally, gene induction in infected cells compared to bystanders was much less similar between the different viral strains than the response when comparing to uninfected control cells (Figure S6J).

Subclustering of the macrophage fraction revealed 4 major cell populations for both explant and autopsy lungs (Figure 7A). Marker expression and pathway analysis (Figure 7B and 7C) showed an inflammatory subpopulation expressing high levels of cytokines, ISGs as well as classical alveolar marker genes such as *FABP4* (inflammatory AM). A population of activated macrophages with high levels of TNFα signaling but weaker induction of other pro-inflammatory genes (act. MΦ) was identified. The other two populations were assigned as classical alveolar macrophages (AM) and a more heterogeneous population of *MERTK*-positive monocyte-derived macrophages (MΦ) [56]. Interestingly, we identified rare cell doublets with mixed AM-AT2 phenotype in the SARS-CoV-2-infected lung explant scSeq data, more frequently than in the controls or the autopsy snSeq data, suggesting that such doublets might represent AT2 cells phagocytosed by AM (Figure S7A, see also Figure 5B). These doublets exhibited similar marker expression and pathway scores to the act. MΦ population (Figure 7B and 7C). Further, we cross-checked our results with multiepitope ligand cartography (MELC) data for the acute COVID-19 autopsy samples (11 days *post symptom* onset). Indeed, macrophages identified by the typical lineage marker CD68 revealed corresponding inflammatory markers such as S100A9 and C1Q, as well as CCR2, CXCR3, and HLA-DR-Q (Figure S7B).

Inflammatory AM and activated macrophage subpopulations were underrepresented in autopsy samples but contained most virus-positive cells in explant lungs (Figure 7D) whereas MΦ in explant lungs were largely negative for SARS-CoV-2 (Figure S7C). We found a significant depletion of the AM population together with an expansion of inflammatory AM both in lung explants and in the acute autopsy samples (Figure 7E). Antiviral and inflammatory pathways as well as apoptotic genes were upregulated in inflammatory AM (Figure 7C). Regulatory network inference (SCENIC [57]) confirmed induction of IFN-regulated factors (*IRF2*, *IRF3*, *IRF5*) in inflammatory AM and NF-κB/TNF signaling regulators in activated MΦ (Figure S7D). Finally, we compared expression patterns of the macrophage subpopulations identified here to published scSeq and snSeq data from lung autopsies as well as broncho-alveolar lavages (BAL) [27, 50, 58, 59] (Figure S7E and S7F). Besides the expected correspondences within more AM-like and more monocyte-like populations, we found high similarity between the inflammatory AM population identified here and some inflammatory macrophage subtypes described previously (Figure S7E). Within this group, dataset-specific gene expression, regarding cytokine induction, indicates differences between lung autopsy tissue, BAL samples, and explant models at different stages of infection (Figure S7F). In particular, we detected early induction of genes such as *CCL3*, *CCL20*, *CXCL5*, *CXCL8* or *IL1B* in the inflammatory macrophages of the explant lungs, which seem not upregulated in later stages of infection in this macrophage subtype.

Next, we corroborated these findings by *ex vivo* infection of isolated AM from human lungs (ACE2$^-$/ACE2$^+$) with SARS-CoV-2 or NL63-CoV, respectively [60], in order to separate gene expression changes due to productive infection or immune response. ScSeq data of about 50,000 cells in 24 samples from two donors and two time points showed substantial differences between the conditions after accounting for variability between the donors (Figure S7G and S7H). ACE2$^+$ macrophages showed increased viral load for both viruses (Figure 7F). Although the levels were too low to reach statistical significance, we detect subgenomic viral RNA (Figure 7F), suggesting active viral replication when AM express apical ACE2 (Figure 4C) [49]. We exploited the increased coverage of the viral genome to inspect the genomic distribution of reads (Figure 7G and S7I) and observed a 3' bias as expected from the poly(A) selection strategy employed in our sequencing protocol. However, within ACE2$^+$ AM, we noted additional enrichment of reads near the 5' and 3' ends of the SARS-CoV-2 genome, confirming the presence of sub-genomic viral RNA [49]. A comparison of MERS-CoV *versus* SARS-CoV-2 in lung explants (Figure S7J), together with the pronounced differences in replication efficiency between MERS-CoV and SARS-CoV-2 (Figure 3B), also suggests productive infection in ACE2-positive *ex vivo* AM only, in agreement with imaging data (Figure 4).

While adenoviral ACE2$^+$ induction by itself induced inflammatory response genes (Figure S7H), ACE2$^-$ AM depicted a transcriptional response to SARS-CoV-2 leading to IFN and TNFα signaling which was absent for NL63-CoV (Figure 7H, Table S7), corroborating our observations in lung explants and autopsy samples.

Discussion

The present study depicts that ACE2 is scarcely expressed in a minor AT2 cell fraction, which correlates with a limited ability of SARS-CoV-2 to propagate in the human alveolar compartment, inferior to IAV and MERS-CoV. Instead, our data from *ex vivo* infected human lung tissue as well as from autopsies suggest that SARS-CoV-2 virions reaching the alveolus are primarily endocytosed by AM leading to induction of different inflammatory phenotypes. In particular, expansion of activated MΦ and inflammatory AM is observed in lung explants and autopsy samples from acute COVID-19 cases, which may play different roles. Based on these results, we conclude that in severe COVID-19, virus-activated AM rather than virus-induced epithelial tissue damage is a central starting point of alveolar pathogenesis. Presumably, the patient-specific risk factors and also the absolute viral load play a role in determining whether a well- or dysregulated immune response develops. Moreover, our infection experiments of AM ($ACE2^-$/$ACE2^+$) indicate non-productive SARS-CoV-2 uptake along with induction of antiviral and inflammatory response pathways.

Based on the study of Hamming *et al.* as well as some more recent studies, a constitutively high or comorbidity induced ACE2 expression should be expected within the alveolar compartment, leading to significant SARS-CoV-2 replication with resulting severe viral pneumonia and ARDS [12-18]. Interestingly, other recent studies revealed opposite findings and claimed a rather low alveolar ACE2 expression [11, 14, 19-21]. These contradictory findings have raised the question if and to what extent alveolar ACE2 matters for SARS-CoV-2 pathogenesis [9-11]. Since several of these studies focused exclusively on *ACE2* mRNA, which can be a hindrance to drawing definite conclusions, we carefully used several independent methods, models and tissue on both, mRNA and protein, to elucidate the alveolar role of ACE2 [11, 20, 22-24].

Our findings regarding ACE2 suggest four major conclusions: First, *ACE2* mRNA expression does not necessarily mount into detectable ACE2 protein expression in pulmonary epithelial cells, which we demonstrate in human bronchial organoids as well as lung tissue. And only ACE2 surface positive cells were susceptible to SARS-CoV-2 infection, which we further validated by forced ACE2 expression in human alveoli and ACE2-positive alveolar organoids.

Second, in line with recent studies such as by Ortiz *et al.*, etc., we found no evidence of *ACE2*/ACE2 expression by other cells such as AT1 cells, endothelial cells, AM or monocytes but only low levels in AT2 cells [19-21, 61]. We could therefore achieve productive SARS-CoV-2 infection only in AT2 cells and not, as described by other studies, in AT1 cells or alveolar macrophages [20, 25-27].

Third, scarce and AT2 cell-restricted ACE2, despite abundantly expressed alternative receptors such as BSG/CD147, NRP1, KREMEN1, or ASGR1, limits alveolar SARS-CoV-2 infection and tissue damage as shown by ‘ACE2 gain of function’ experiments in bronchial organoids and lung tissue [40, 43, 52, 53]. Notably, only if ACE2 expression in lung tissue is forced by overexpression to various other cell types including AT1 cells, macrophages and endothelium, a broadened SARS-CoV-2 tropism as well as an increased alveolar damage similar to the level of MERS-CoV can be observed [46]. This is of particular interest suggesting that permissiveness for the virus should be judged against direct evidence for ACE2 protein. Thus, while IAV H3N2 and MERS-CoV show substantial replication in human lung tissue, correlating with abundant corresponding receptor expressions, the low ACE2 expression limits permissiveness of the human alveolus for SARS-CoV-2 as well as SARS-CoV [45-47]. In further support of our hypothesis that it is primarily ACE2, and not alternative abundantly expressed receptors such as BSG/CD147, NRP1, KREMEN1 or ASGR1, that limit the tropism of SARS-CoV-2 in the human lung, a rapid saturation of the replication rate even for strongly increased viral load showed that the virus is not able to propagate in the human lung without sufficient ACE2 [8].

Fourth, although *ACE2* mRNA was slightly induced by interferon (IFN)-β, neither direct IFN stimulation nor indirectly induced IFNs by viral infection of IAV, SARS-CoV, SARS-CoV-2, or MERS-CoV could increase ACE2 protein in human lungs, as suggested by Ziegler *et al*. [18]. Likewise, no difference of ACE2 was found in autopsy lungs, which led us conclude that IFN-driven ACE2 induction is unlikely to foster disease severity. This mismatch in slight *ACE2* induction without increase of protein expression could probably be explained by the finding of Onabajo *et al.* who demonstrated the truncated ACE2 receptor deltaACE2 as the actual ISG [62]. The deltaACE2 lacks several hundred amino acids at the N-terminus thereby abolishing S-protein binding and cellular-viral fusion. These data show that further in-depth studies are needed to determine isoforms, regulatory mechanisms and the definite role of ACE2 domains regarding course of COVID-19.

Regarding the cellular tropism of SARS-CoV-2, spectral microscopic analyses of *in situ* hybridization and immunohistochemistry against *N-/S-genes* as well as corresponding viral proteins revealed very few virus-positive AT2 cells in lung explants and autopsy samples, which supports the findings of Hou *et al*. [20]. However, in contrast to Hui *et al*., the use of highly sensitive spectral imaging revealed a distinct punctuated pattern for SARS-CoV-2 in AM, including autopsy samples. This punctuate staining in wildtype AM, in contrast to the even cytosolic distribution in AT2 and ACE2^{+}-AM, is a morphological indicator of non-productive *versus* productive infection and raises another question: if limited presence of ACE2 in human AT2 cells allows only few replicative niches for SARS-CoV-2 with only minor virus-induced tissue damage, which mechanisms trigger severe inflammation of this compartment [9]? Several studies so far detected SARS-CoV-2 in lung monocytes and macrophages arriving at different conclusions regarding immune activation and productive infection of these cells [27, 50, 58, 59, 63-66]. Therefore, we tested the hypothesis that these cells adopt a very early pro-inflammatory phenotype as result of viral uptake rather than productive infection. Results from lung explants and autopsy indicate that SARS-CoV-2 RNA is predominantly found in macrophages but rarely in other cell types, while IAV or MERS-CoV RNA is present in almost all cell types. Comparison of macrophages from acute COVID-19 individuals and the explant model showed consistent activation of several pathways including chemo-/cytokine production, IFN signaling and response, TNF/NF-κB signaling and apoptosis. An in-depth characterization of macrophage subclusters in autopsy samples and explants further revealed a strong activated as well as inflammatory phenotype, which increase in abundance in the SARS-CoV-2 infected explants as well as in acute autopsy cases.

Whereas activated MΦ seem to obtain their phenotype mainly by phagocytosis of infected and apoptotic AT2 cells, endocytosis of SARS-CoV-2 virions predominantly induces the inflammatory AM phenotype, which is not present after uptake of NL63-CoV. Interestingly, this inflammatory activation seems independent of productive SARS-CoV-2 infection since SARS-CoV-2 subgenomic RNA was only noticed by ACE2 overexpression (ACE2^{+}-AM) and not in the wildtype AM population [64, 65]. In this regard, our conclusions differ from Grant *et al*. who used negative strand (antisense) viral RNA as indicator for productive infection. In our data, we found antisense RNA at similar levels in well-expressed housekeeping genes, likely due to limited strand specificity in library preparation. Likewise, infection neither with SARS-CoV-2 or the well-replicating MERS-CoV resulted in an increase of viral antisense RNA above this technical background level. Additionally, our conclusion is supported by a Syrian hamster model, in which SARS-CoV-2 uptake without productive infection is frequently observed leading to strong activation of macrophages [67]. Experiments in mice indicate that the detection of SARS-CoV-2 spike protein may be important for AM activation [68], and co-stimulation of AM with low fucosylated anti-spike IgG in early COVID-19 may further fuel subsequent development of lung damage [69]. Together, these data indicate that uptake of SARS-CoV-2 induces (next to activated MΦ) an inflammatory AM phenotype characterized by a subsequent pro-inflammatory response, although not driven by productive infection, probably contributing to severe lung and systemic inflammation dependent on underlying individual risk factors such as gender, age, and co-morbidities.

Indeed, a drawback of the explant model is that infection and pro-inflammatory activation of AM does not allow for recruitment of further immune cells such as neutrophils or T cells. However, by analyses of intercellular receptor-ligand interactions in the acute and prolonged autopsy cases we identified several up- and down-regulated signaling pathways, which are probably the outcome of the pro-inflammatory activation [70]. The identified integrin/TGF axis in COVID-19 has been associated with triggering vascular leakage and its blockage could attenuate viral replication in the airway epithelium [71, 72]. In addition, the identified low *CCL5* together with high viral load may direct to severe outcome in COVID-19 [73]. And although a benefit for the *CCL5*/*CCR1* axis disruption for COVID-19 outcome has been described, its functional role is so far not elucidated [74]. These and other signaling pathways need to be considered and analyzed in detail in subsequent studies.

Further factor specific analysis of SARS-CoV-2-positive AM revealed, compared to bystander cells, induction of endosomal TLR8 or the NLRP3 inflammasome activator P2X7 receptor (*P2RX7*), which may support subsequent cytokine and chemokine release [75, 76]. Notably, a recent study indicated NLRP3 inflammasome activation in human primary monocytes exposed to SARS-CoV-2 and CD14-positive cells in lung autopsy samples [76, 77]. In (virus-positive) macrophages, P2X7R is part of the STING signaling cascade [78], and SARS-CoV-2 seems to initiate cGAS-STING-related macrophage activation [79], which may contribute to COVID-19 immunopathology [80]. Along those lines, detection of SARS-CoV-2 N-protein may furthermore aggravate inflammation by inflammasome activation [81].

The observed upregulation of NF-κB1 (nuclear factor kappa B subunit 1) could further detrimentally enhance inflammation since inhibition of this pathway reduced lung inflammation and increased survival in SARS-CoV infected mice [82]. Severe inflammation caused by macrophage expression of cyclooxygenase-2 (*PTGS2*) contributed to avian H5N1 infection [83] and we noted pronounced *PTGS2* up-regulation in SARS-CoV-2-positive AM. In line, upregulation of myristoylated alanine-rich C kinase substrate (*MARCKS*) may contribute to increased macrophage pro-inflammatory cytokine expression [84], and we indeed noted increased expression of interleukin-1 alpha (*IL1A*) [85]. Upregulated molecules such as *MARCKS* and proline-serine-threonine phosphatase-interacting protein 2 (*PSTPIP2*) may increase the directed migration of those cells [86]. In H1N1 IAV-infected mice fatty acid binding protein 5 (*FABP5*)-deficiency caused excessive inflammation and we noted reduced *FABP5* presence in SARS-CoV-2-positive macrophages [87] indicating that down-regulation of genes in macrophages may also contribute to enhanced inflammation. On the other hand, augmented expression of TNF alpha-induced protein 6 (*TNFAIP6*) in SARS-CoV-2-positive AM may counter-regulate excessive inflammation, since deletion of this molecule in mice augmented inflammatory lung injury and mortality in an acute lung injury model [88].

Since several studies already reported monocyte/macrophage activation in COVID-19, we compared our annotated monocyte/macrophage datasets with that of the studies by Grant *et al*., Liao *et al*., Delorey *et al*., and Wendisch *et al*. [27, 50, 58, 59]. As expected, tissue-resident macrophages, monocytes and inflammatory macrophages are found with similar signatures in all datasets. However, relative comparison of inflammatory chemo- and cytokine induction in the inflammatory AM phenotype shows a different focus among the data sets. In particular, in the inflammatory AM of the explant lungs early induction of e.g. CCL3, CCL20, CXCL5, CXCL8 or IL-1β was detected, which seem less upregulated in later stages of infection, thereby reflecting the very early (immediately after virus ingestion) response in AM probably responsible for recruitment of systemic immune cells and further activation [89-92].

Thus, the observed pro-inflammatory phenotype of macrophages observed in our study (and other reports) may contribute to severe COVID-19 by creating a strong local pro-inflammatory environment contributing to alveolar malfunction, including impaired barrier function and endothelial activation [77, 93, 94]. Subsequent endothelial activation fueled by the pro-inflammatory macrophages may result in the reduction of thrombo-protective mechanisms, thereby promoting local coagulation [95, 96]. Indeed, increased expression of pro-coagulant markers, and chemokines in endothelial cells was noted in endothelium exposed to the culture medium of monocytes preincubated with SARS-CoV-2 spike S1 protein [97].

Studies of autopsy specimens from deceased COVID-19 patients suggest complex activation of various pro-inflammatory phenomena, some of which are based on direct local tissue responses, which in turn are highly dependent on recruited cells or systemic factors (e.g. complement) [97, 98]. Of note, even within severe COVID-19 courses, there can be considerable variation in the manifestation of the disease [7] and it is still unclear why severe COVID-19 results in some specific disease features, such as the massive occurrence of microthrombi in small vessels, that do not occur in classical ARDS. Similarly, it is important to clarify why other diseases with comparable activation of AM have a different phenotype and which factors ultimately determine the specific susceptibility of patient subgroups to severe COVID-19.

Collectively, our data strongly support our conclusion that, due to scarce alveolar ACE2 expression, direct SARS-CoV-2 infection of AT2 cells and related tissue damage is most likely not the driving force for an overwhelming cytokine release and macrophage inflammation leading to severe courses of COVID-19. When significant amounts of SARS-CoV-2 viruses may reach the alveoli from the upper respiratory tract, their uptake by AM induces specific pro-inflammatory phenotypes that appear to trigger the subsequent systemic responses. This presumably occurs without relevant viral replication, initial tissue damage and release of epithelial-derived danger-associated-molecular-patterns. However, the specific and strong induction of inflammatory macrophage phenotypes cannot alone explain which patients progress to severe disease. Therefore, individual risk factors in large cohorts need to be correlated with the specific activated pathways of macrophage subtypes.

Acknowledgements: The authors thank Doris Frey, Lisa Skrip, Gudrun Heinz for excellent technical assistance as well as Jeannine Wilde, Tatiana Borodina, Daniele Sunaga-Franze and Madlen Sohn from the MDC/BIH sequencing facility.

Availability of data and materials: All raw data are available by request to the corresponding author.

Conflict of interest: The authors declare no competing interests.

Support statement: A.C.H., L.E.S., S.H. were supported by Berlin University Alliance GC2 Global Health (Corona Virus Pre-Exploration Project).

A.C.H., S.H., T.W. and C.D. were supported by BMBF (RAPID) and A.C.H., S.H. by BMBF (alvBarriere-COVID-19).

K.H., L.B., S.L., S.H., C.D., C.G., T.W., A.C.H. were funded by BMBF (NUM-COVID 19, Organo-Strat 01KX2021).

K.H., N.S., L.E.S., M.W., S.H., A.D.G., C.D., T.W. and A.C.H. were supported by DFG (SFB-TR 84).

A.C.H. was supported by BIH and Charité-Zeiss MultiDim.

A.C.H. and S.H. were supported by Charite 3^R.

K.H., A.C.H., M.K., A.D.G. and S.H. were supported by Einstein Foundation EC3R.

K.H. and C.D. were supported by BMBF (Camo-COVID-19).

M.W., N.S. and S.H. was supported by BMBF (PROVID).

C.G. and A.C.H. were funded by BIH.

M.W. and N.S. was supported by BIH and BMBF (SYMPATH, CAPSyS, NAPKON).

B.O. and D.B. were funded through the BIH Clinical Single Cell Bioinformatics Pipeline. Computation has been performed on the HPC for Research cluster of the Berlin Institute of Health.

L.B. was supported by the BMBF (CoIMMUNE), the DFG (KFO 342) and the IZKF of the Medical Faculty of the WWU.

A.E.H., R.M. and A.P.R. were supported by funding from the DFG, HA5354/10-1, SPP1937 (HA5354/8-2) and TRR130 P17.

H.R. was supported by DFG (RA 2491/1-1).

Author contributions: K.H., C.M., D.F., M.K., S.D., K.H., M.B., J.S., B.B., M.M., K.H., A.M.Z., A.L., P.G., Z.D. and L.B. performed and analyzed experiments. E.W. performed sequencing and contributed to data analysis supervised by M.L. B.O. performed analysis of sequencing data, supervised by D.B. J.H. and A.D.G. performed the processing for histology and immunofluorescence and supported with probe design. M.D. did the computational analysis of the pathology samples. S.E., F.K., D.H., H.R., J.R., and F.H. provided the pathological patient samples. M.T., T.T.B., S.E, H.L.T., P.S., J.N. and J.C.R. provided the lung tissue explants and regarding meta-data. C.H., J.B. and K.S.O. provided kidney tissue and protein. D.N., C.D., M.M., V.C. and C.G. were responsible for virus sequencing, qPCR, and virus stock preparation. A.E.H., R.M. and A.PR performed the MELC studies. T.W., S.H., N.S., S.L., M.W. and L.E.S. provided conceptual advice. A.C.H., K.H. and B.O. wrote the manuscript. A.C.H. conceived and supervised the study. All authors revised and approved the final version of the manuscript.

Figure Legends

Figure 1

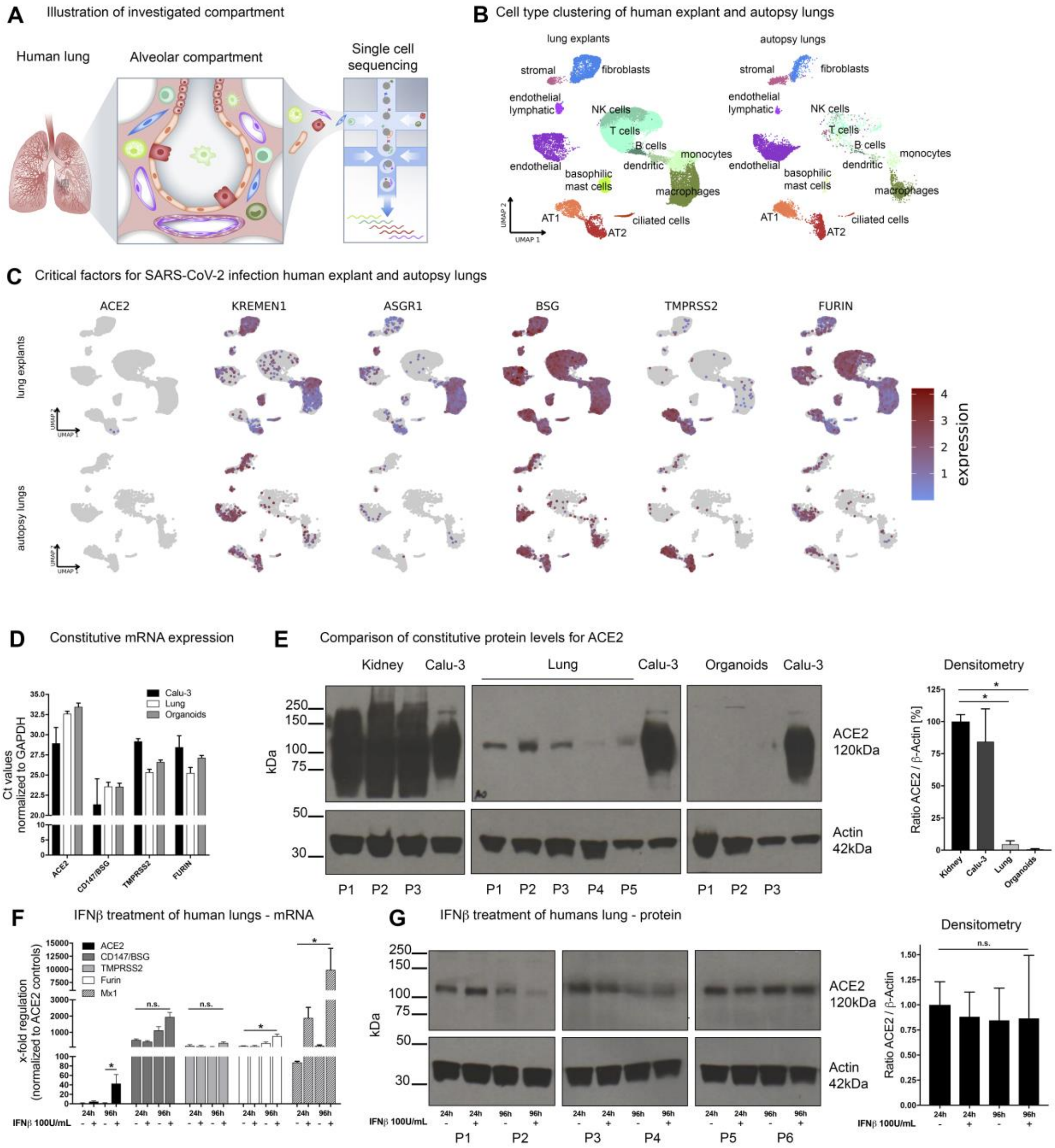

Figure 1. ACE2 expression is scarce in human lungs and cannot be induced by interferon on the protein level

(A) Schematic illustration of cell types of the investigated alveolar compartment as well as single-cell RNA sequencing (scSeq).

(B) Annotation of cell clusters from scSeq and single-nucleus RNA sequencing (snSeq) of human lung tissue and autopsy material, respectively. Confirmation of major cell types by related marker gene expression is presented in Figure S1A and S1B.

(C) Comparison of scarce *ACE2* expression in AT2 cells with abundant *KREMEN1, ASGR1, CD147/BSG, TMPRSS2* and *FURIN* expression by scSeq and snSeq.

(D) Analysis of *ACE2*, *CD147/BSG*, *TMPRSS2* and *FURIN* expression by qPCR on bulk RNA of normal human lung tissue, human bronchial organoids, and Calu-3 cells. Ct values are normalized to GAPDH expression to demonstrate absolute levels of ACE2 compared to other factors.

(E) Analysis of constitutive ACE2 expression by Western blot using the R&D AF933 antibody (left panel). Antibody evaluation is presented in Figure S1C. Shown are protein lysates from human kidneys (3 donors), human lungs (5 donors), human bronchial organoids (3 donors) and Calu-3 cells. Prolonged exposure time (30 sec) of membranes was carried out to demonstrate scarce ACE2 expression in lungs and bronchial organoids compared to kidneys and Calu-3. Exposure time of 1 sec is shown in Figure S1D. β-Actin served as loading control. Densitometric analysis shows semi-quantitative ACE2 expression normalized to β-Actin (right panel).

(F) Human lung tissue was stimulated for 24 h and 96 h with IFNβ and *ACE2*, *CD147/BSG*, *TMPRSS2*, *FURIN* and *Mx1* expression was analyzed by qPCR on bulk RNA.

(G) Western blot analysis of ACE2 expression in IFNβ-stimulated human lung tissue after 24 h and 96 h of 6 donors (left panel) and corresponding densitometric analysis normalized to β-Actin.

Data are represented as mean ± SEM, * $p < 0.05$.

Figure 2

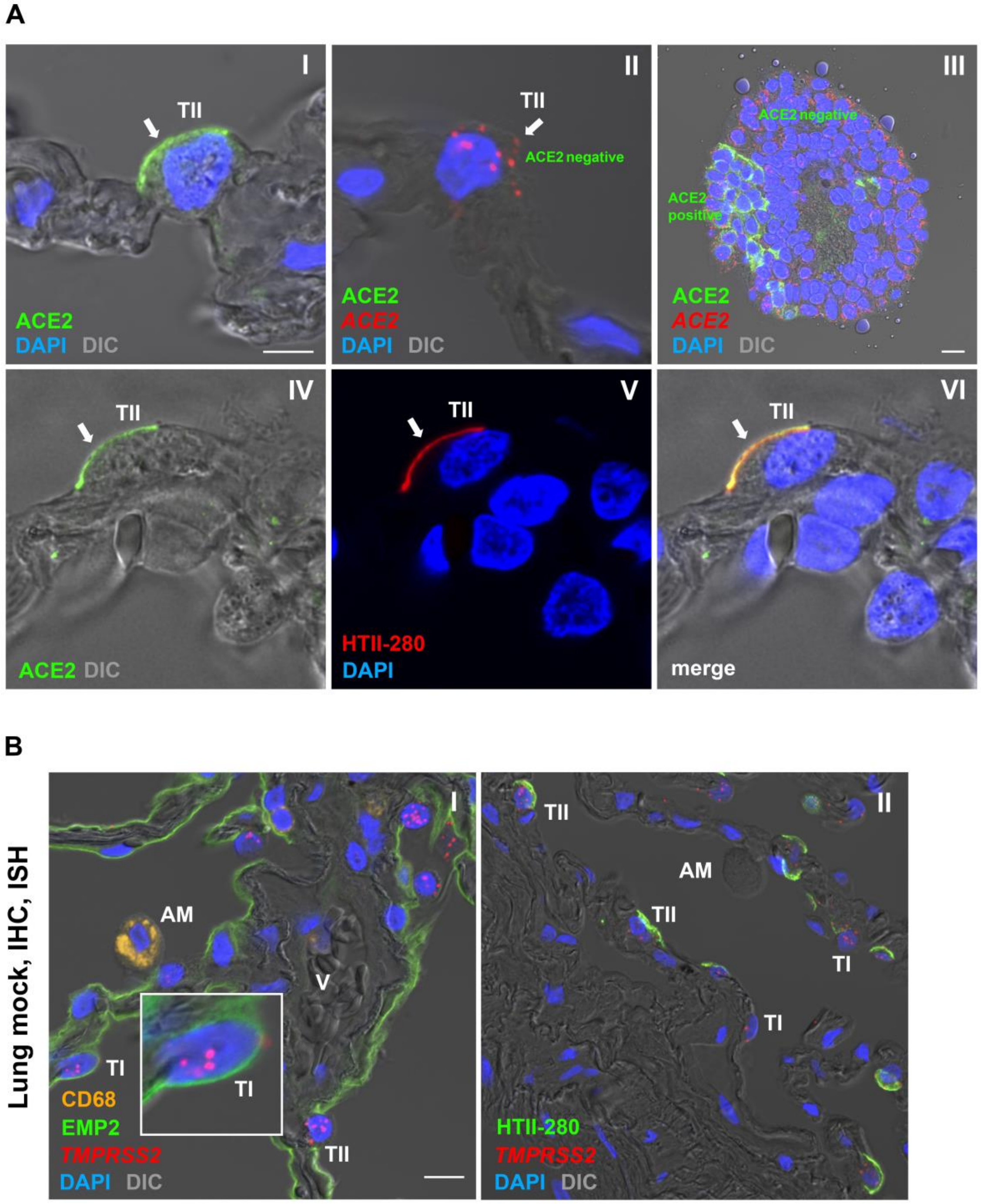

Figure 2. Spectral imaging reveals scarce apical ACE2 on AT2 cells, less congruence with *ACE2* as well as abundant *TMPRSS2* expression in AT1 and AT2

Immunohistochemistry and *in situ* hybridization were analyzed in human lung tissue and organoids by spectral microscopy and linear unmixing.

(A) Panel I shows single channel detection (to avoid antibody cross-reactivity) of ACE2 immunostaining (green) on the apical surface of an AT2 cell (TII). AT2 / ACE2 expression was confirmed by dual-channel detection with AT2 marker HTII-280 (red) in panels IV-VI (white arrows). Panel II shows *ACE2* mRNA (red) in an AT2 cell. Sequential immunostaining could not reveal ACE2 protein on the apical surface (white arrow). Lack of apical ACE2 protein in a fraction of *ACE2* mRNA (red) positive cells is demonstrated by lentiviral over-expression in a human bronchial organoid in panel III. Parts of the cells show apical ACE2 (green) as well. Cell nuclei are visualized by DAPI stain (blue). Scale bar for lungs 5 µm and bronchial organoids 10 µm.

(B) Immunostaining for CD68 (AM, orange) and EMP2 (AT1, green) as well as *in situ* hybridization for *TMPRSS2* (red, panel I) and HTII-280 (AT2, panel II, green) in human lung tissue shows *TMPRSS2* positive in AT1 (inset) and AT2, but not vessels (V) or AM. Cell nuclei are visualized by DAPI stain (blue), scale bar 10 µm.

ACE2 expression in Calu-3 cells and kidneys as well as ACE2 antibody tests are presented in Figure S2.

Figure 3

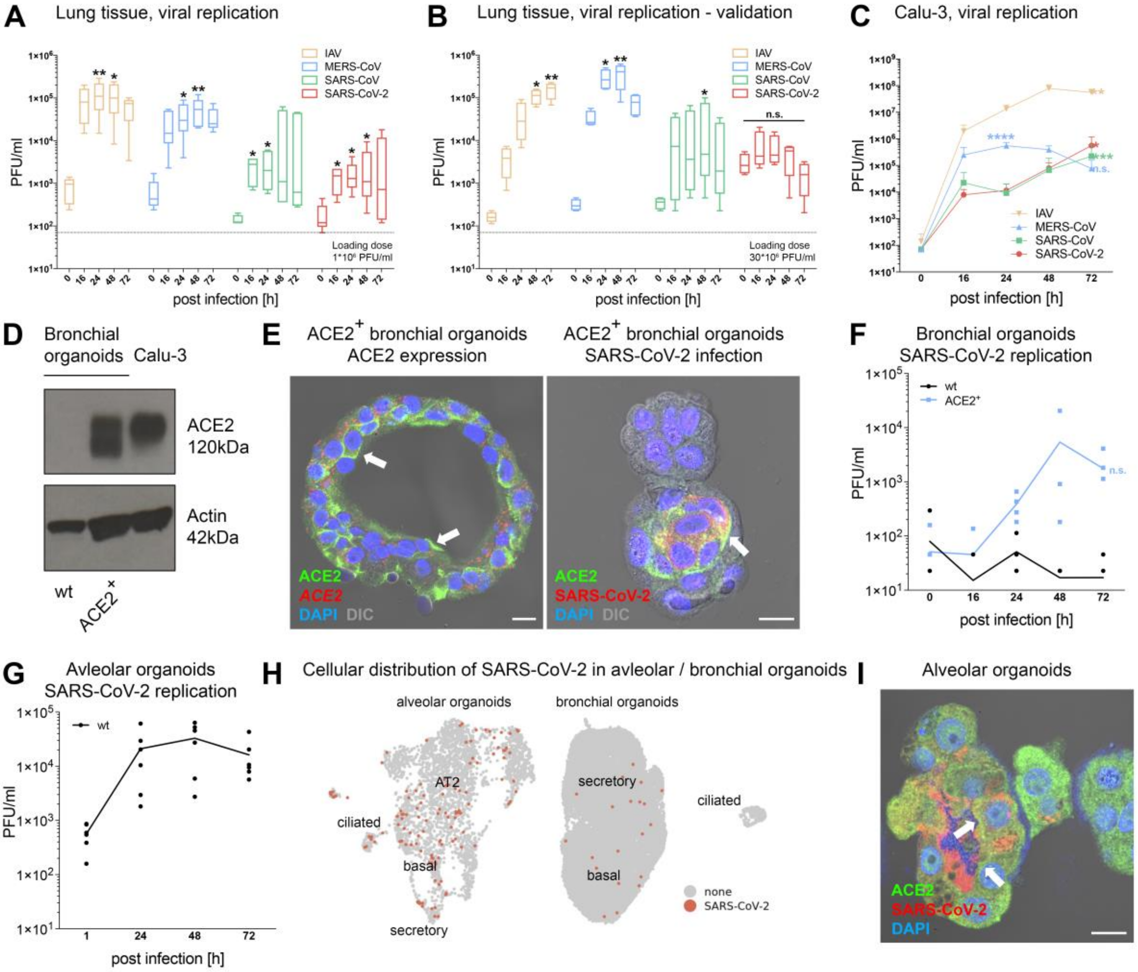

Figure 3. SARS-CoV-2 shows low replication on human lung tissue which can be increased by ACE2 overexpression

(A) Human lung tissue explants (5 donors) were infected with IAV (orange), MERS-CoV (blue), SARS-CoV (green) and SARS-CoV-2 (red) with $1*10^6$ PFU and viral replication was assessed.

(B) Human lung tissue explants (4 donors) were infected with IAV H3N2 (orange), MERS-CoV (blue), SARS-CoV (green) with $1*10^6$ PFU and SARS-CoV-2 (red) with $30*10^6$ PFU and viral replication was measured showing validation of Figure 3A for all viruses and loss of significance for SARS-CoV-2. External validation experiment of SARS-CoV-2 replication (3 donors) is shown in Figure S3A.

(C) Calu-3 cells were infected with IAV H3N2 (orange), MERS-CoV (blue), SARS-CoV (green) and SARS-CoV-2 (red) with MOI 0.1 and viral replication was assessed.

(D) ACE2 expression (Western blot) in wildtype human bronchial organoids (wt), organoids with lentiviral transduction and overexpression of ACE2 (ACE2$^+$) and Calu-3 cells. β-Actin served as loading control.

(E) ACE2 immunostaining (green) and *in situ* hybridization (red) in human ACE2$^+$ bronchial organoids (left panel) showing abundant *ACE2* mRNA expression with a sub-fraction of cells positive for apical ACE2 protein expression. The right panel demonstrates a partly apical expression of ACE2 in ACE2$^+$ bronchial organoids as well as a congruency for SARS-CoV-2 S-protein detection in these cells (16 h post infection, MOI 1). Cell nuclei are visualized by DAPI stain (blue), scale bar 10 µm.

(F) Wildtype (wt, black) and ACE2 overexpressing (ACE2$^+$, blue) bronchial organoids (4 independent experiments) were infected with SARS-CoV-2 with MOI 1 and viral replication was measured after 0, 16, 24, 48 and 72 h depicting no permissiveness for SARS-CoV-2 when ACE2 is missing and increased permissiveness after ACE2 overexpression.

(G) Wildtype (wt) alveolar organoids (6 independent experiments) were infected with SARS-CoV-2 with MOI 1 and viral replication was measured after 0, 24, 48 and 72 h.

(H) UMAP embedding of alveolar and bronchial organoid data shows cells positive for SARS-CoV-2 (red).

(I) ACE2 immunostaining (green, arrows show apical ACE2 expression in SARS-CoV-2 infected cells) and SARS-CoV-2 S-protein detection (red) in human alveolar organoids (24 h post infection, MOI 1, three independent experiments). Cell nuclei are visualized by DAPI stain (blue), scale bar 10 µm.

Data are represented as mean ± SEM, * $p < 0.05$, ** $p < 0.01$, *** $p < 0.001$.

Figure 4

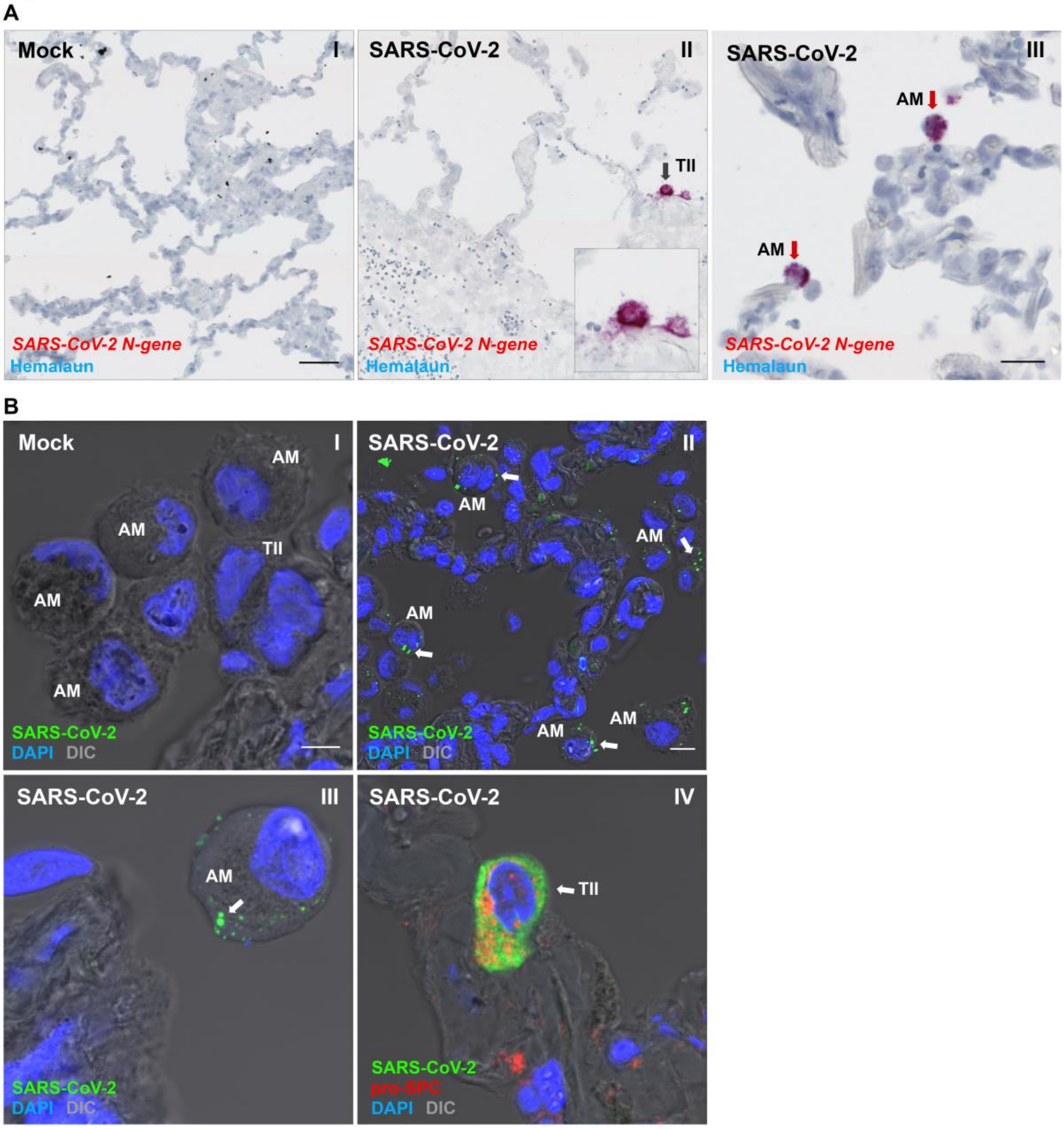
A
Mock
I
SARS-CoV-2 N-gene
Hemalaun
SARS-CoV-2
II
TII
SARS-CoV-2 N-gene
Hemalaun
SARS-CoV-2
III
AM
AM
SARS-CoV-2 N-gene
Hemalaun
B
Mock
I
AM
AM
TII
AM
AM
SARS-CoV-2
DAPI DIC
SARS-CoV-2
II
AM
AM
AM
AM
AM
SARS-CoV-2
DAPI DIC
SARS-CoV-2
III
AM
SARS-CoV-2
DAPI DIC
SARS-CoV-2
IV
TII
SARS-CoV-2
pro-SPC
DAPI DIC

Figure 4

C

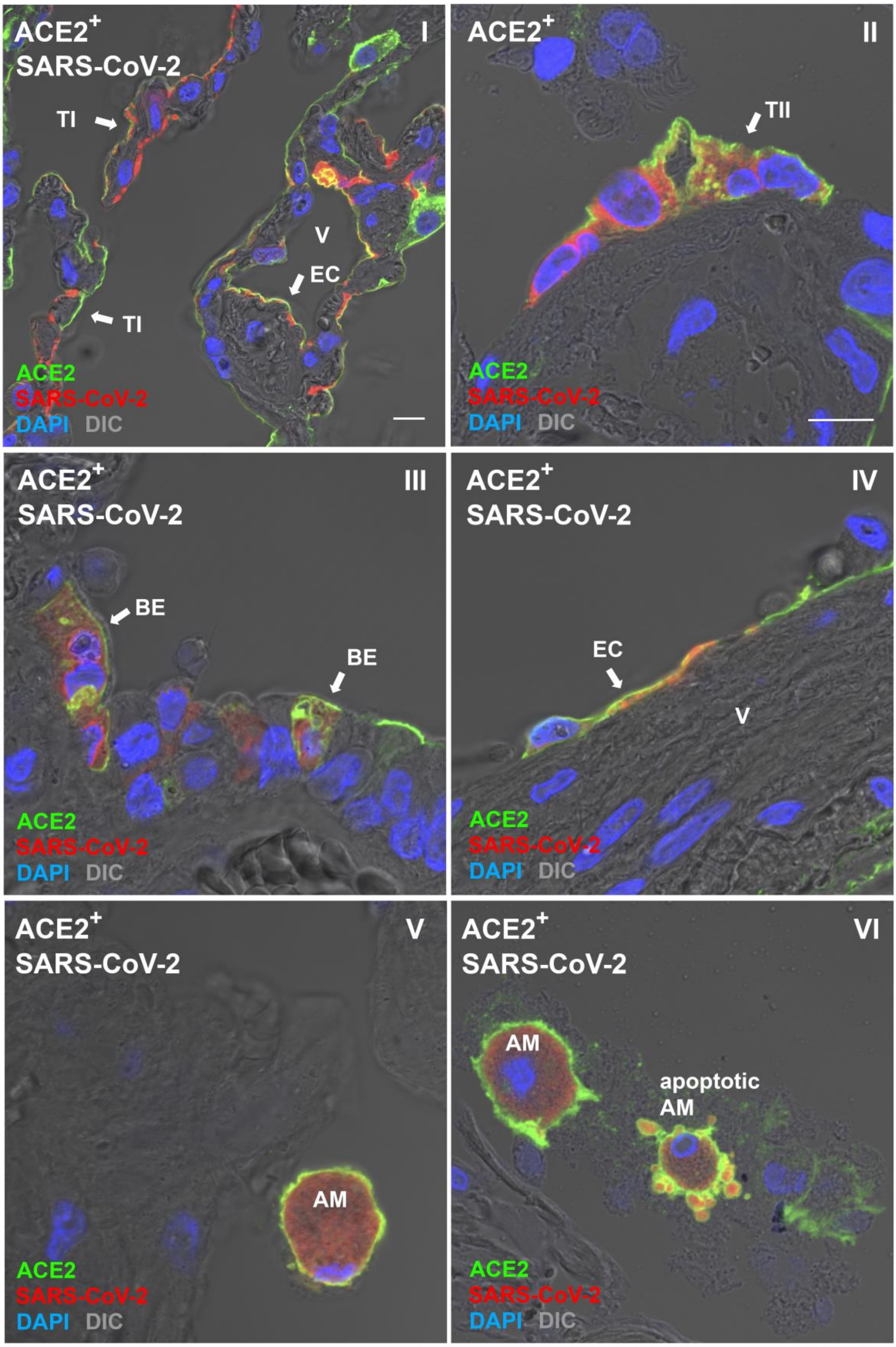
ACE2+ SARS-CoV-2
I
TI
TI
V
EC
ACE2
SARS-CoV-2
DAPI DIC
ACE2+
II
TII
ACE2
SARS-CoV-2
DAPI DIC
ACE2+ SARS-CoV-2
III
BE
BE
ACE2
SARS-CoV-2
DAPI DIC
ACE2+ SARS-CoV-2
IV
EC
V
ACE2
SARS-CoV-2
DAPI DIC
ACE2+ SARS-CoV-2
V
AM
ACE2
SARS-CoV-2
DAPI DIC
ACE2+ SARS-CoV-2
VI
AM
apoptotic AM
ACE2
SARS-CoV-2
DAPI DIC

D

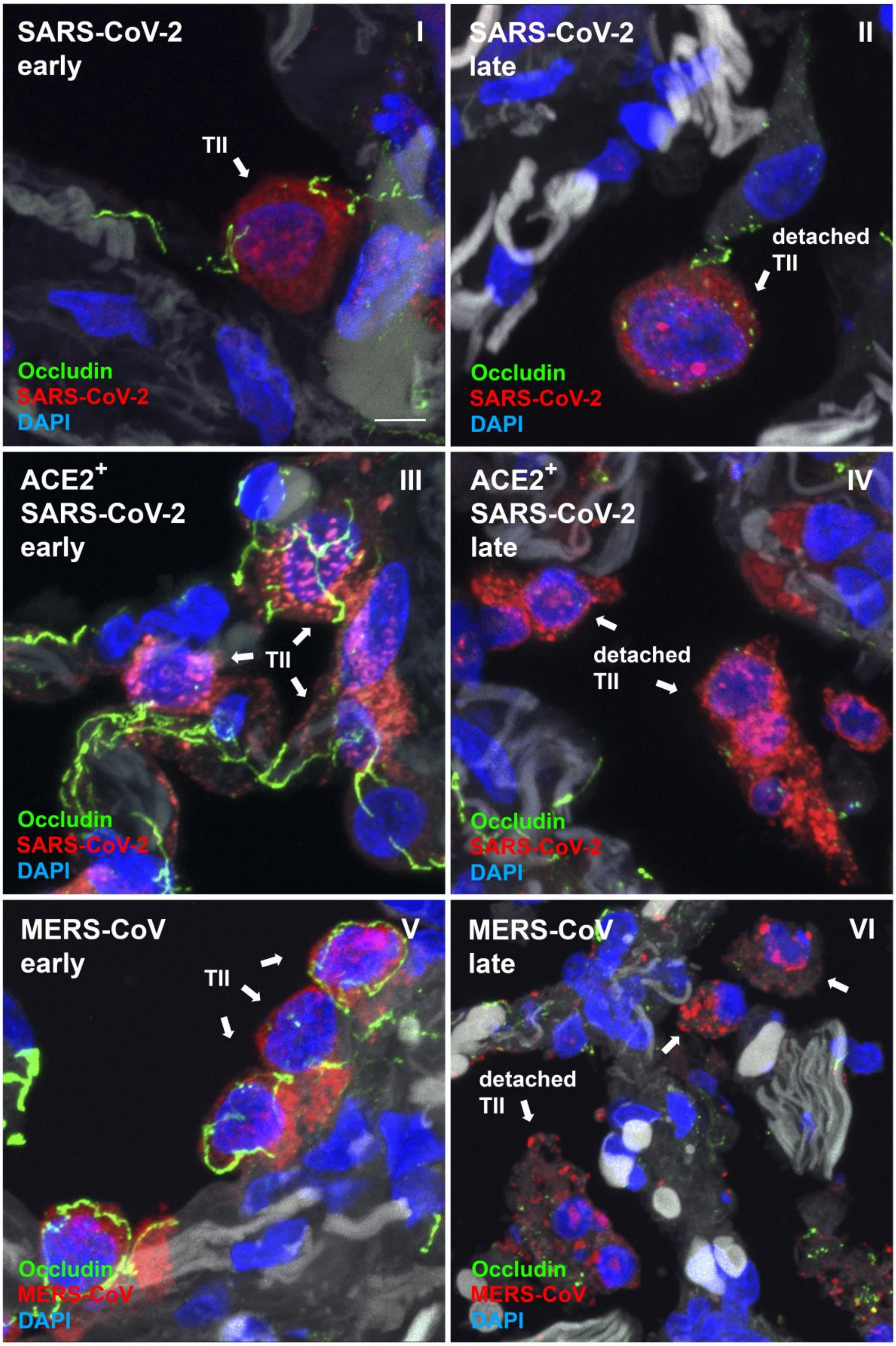
SARS-CoV-2
early
I
TII
Occludin
SARS-CoV-2
DAPI
SARS-CoV-2
late
II
detached
TII
Occludin
SARS-CoV-2
DAPI
ACE2$^+$
SARS-CoV-2
early
III
TII
Occludin
SARS-CoV-2
DAPI
ACE2$^+$
SARS-CoV-2
late
IV
detached
TII
Occludin
SARS-CoV-2
DAPI
MERS-CoV
early
V
TII
Occludin
MERS-CoV
DAPI
MERS-CoV
late
VI
detached
TII
Occludin
MERS-CoV
DAPI

Figure 4. SARS-CoV-2 has a rare tropism to AT2 but is frequently phagocytosed by alveolar macrophages (AM) in *ex vivo* infected human lungs

(A) *In situ* hybridization for *N-gene* of SARS-CoV-2 (red) in mock-infected (panel I) and SARS-CoV-2 infected ($30*10^6$ PFU, panel II and III) human lung tissue. Black arrows indicate AT2 cells (TII) and red arrows AM. Cell nuclei are visualized by Hemalaun stain (blue). Scale bar 50 µm for panel I and II and 20 µm for panel III.

(B) Spectral imaging of immunostained SARS-CoV-2 (N-protein, green) in mock-infected (panel I) and SARS-CoV-2-infected ($30*10^6$ PFU, panel II, III and IV) human lung tissue confirms rare AT2 tropism but punctuated viral staining pattern in AM. AT2 cells (TII) and AM are indicated in panel I, II and III. Pro-SPC staining (red) was used in panel IV as AT2 marker. Cell nuclei are visualized by DAPI stain (blue). Scale bars 5 µm for panel I, III and IV and 10 µm for panel II.

(C) Overexpression of ACE2 ($ACE2^+$, green) in human lung tissue results in broadening of $ACE2^+$ cell types. ACE2-positive AT1 (TI, panel I), endothelial cells (EC, panel I and IV), AT2 (TII, panel II), bronchial epithelium (BE, panel III) and AM (panel V and VI) show correlation with SARS-CoV-2 infection (red). Cell nuclei are visualized by DAPI stain (blue), scale bars 10 µm.

(D) Occludin lining and loss (green) indicate virus-induced tissue damage, which is moderate at early and late stages of SARS-CoV-2 infection in human lung tissue (panels I and II). Overexpression of ACE2 ($ACE2^+$) in human lungs leading to a broadened cellular tropism of SARS-CoV-2 (panel III) results in an increase of cellular damage at late stages of infection (panel IV), similar to MERS-CoV (panels V and VI). Cell nuclei are visualized by DAPI stain (blue), scale bars 5 µm.

MERS-CoV immunostaining and *in situ* hybridization in human lung tissue and SARS-CoV-2 immunostaining and *in situ* hybridization in Calu-3 cells as well as control staining for $ACE2^+$ and occludin are presented in Figure S4.

Figure 5

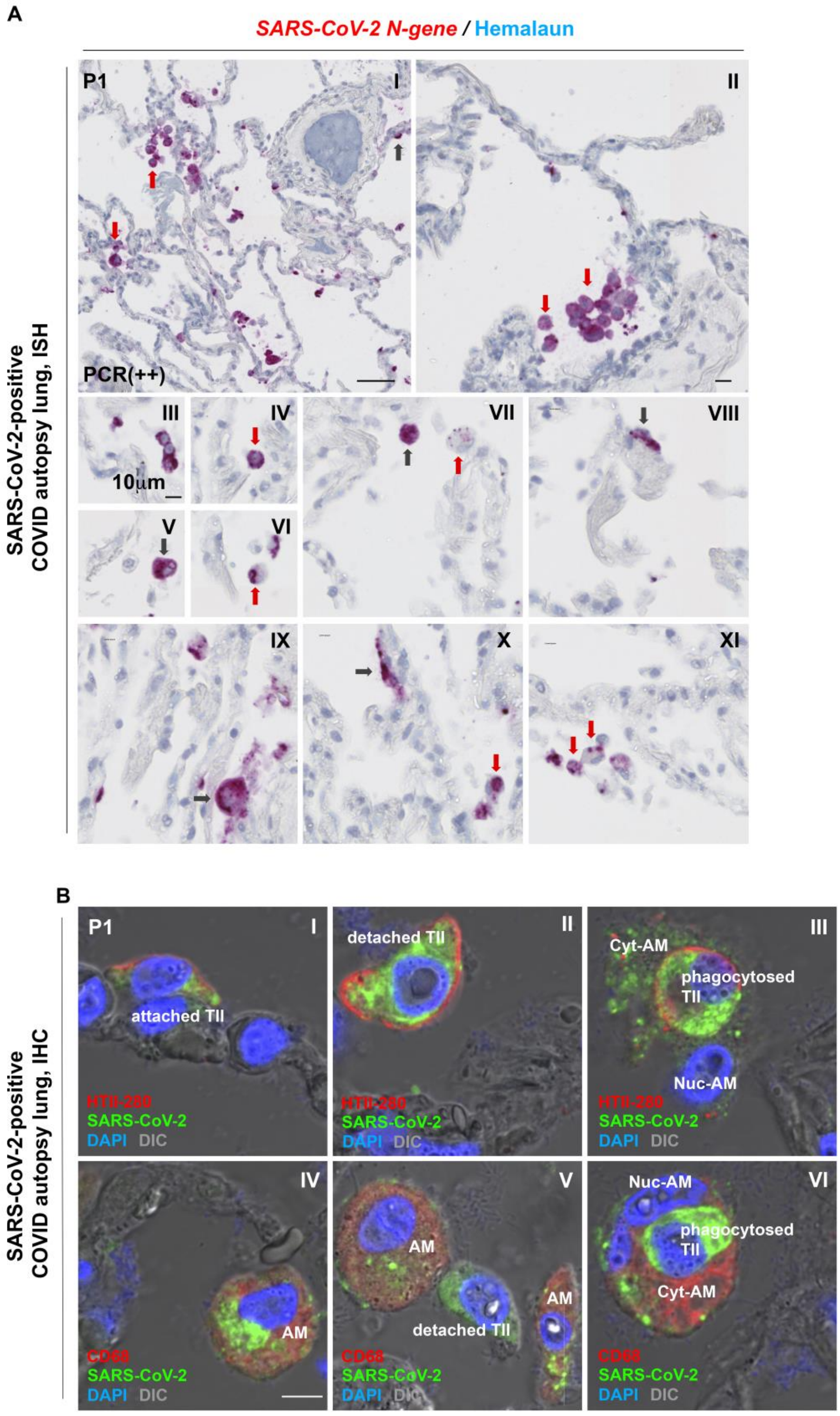
A
SARS-CoV-2 N-gene / Hemalaun
SARS-CoV-2-positive
COVID autopsy lung, ISH
P1
I
II
PCR(++)
III
10μm
IV
VII
VIII
V
VI
IX
X
XI
B
SARS-CoV-2-positive
COVID autopsy lung, IHC
P1
I
attached TII
HTII-280
SARS-CoV-2
DAPI DIC
II
detached TII
HTII-280
SARS-CoV-2
DAPI DIC
III
Cyt-AM
phagocytosed
TII
Nuc-AM
HTII-280
SARS-CoV-2
DAPI DIC
IV
AM
CD68
SARS-CoV-2
DAPI DIC
V
AM
detached TII
AM
CD68
SARS-CoV-2
DAPI DIC
VI
Nuc-AM
phagocytosed
TII
Cyt-AM
CD68
SARS-CoV-2
DAPI DIC

Figure 5. SARS-CoV-2 detection in AM and fewer AT2 cells in lungs of an early COVID-19 death

(A) *In situ* hybridization for *N-gene* of SARS-CoV-2 (red) in an autopsy lung 5 days after COVID-19 diagnosis. Black arrows indicate AT2 cells and red arrows AM. Cell nuclei are visualized by Hemalaun stain (blue), scale bar 50 µm for panel I and 10 µm for II - XI. Additional donors of SARS-CoV-2-positive COVID-19 autopsy lungs and non-COVID-19 autopsy lung are shown in Figure S5. Infected areas show highly positive cells but lack of inflammatory cell infiltration indicated by free alveoli and well-shaped alveolar septs.

(B) Immunolabeling of AT2 cells with HTII-280 (red, TII, panel I, II and III), AM with CD68 (red, AM, panel IV, V and VI) and SARS-CoV-2 (green, panel I - VI). Cytosolic staining pattern of AT2 indicate productive infection, whereas the punctuated patterns in AM indicate viral uptake. Note that infected AT2 (TII) detach from the basal membrane (panel II) and get endocytosed by AM (panels III and VI). Cell nuclei are visualized by DAPI stain (blue), scale bar 5 µm.

Control staining on autopsy material as well as all other cases are shown in Figure S5.

Figure 6

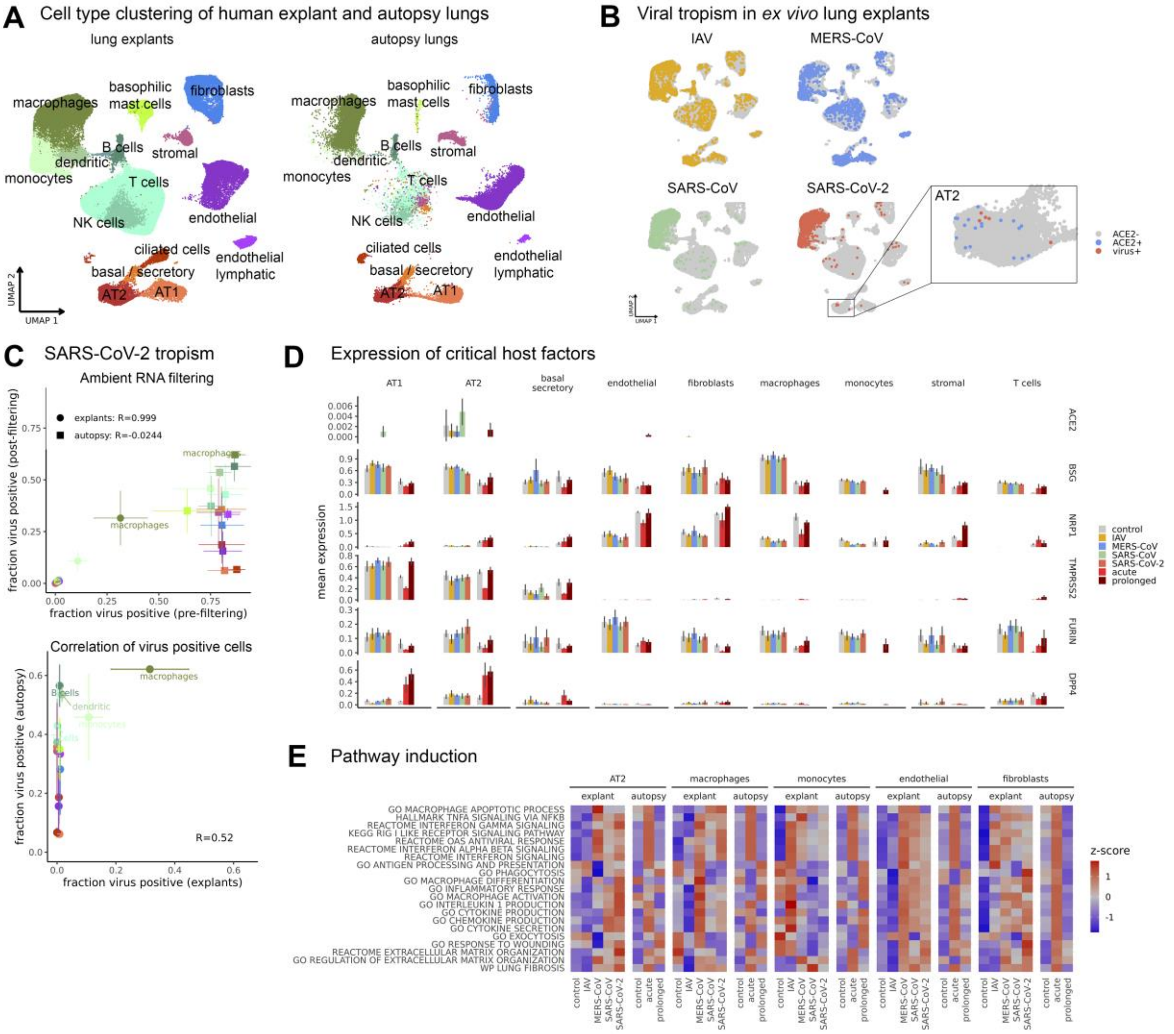

Figure 6. Single-cell and single-nucleus RNA sequencing reveals uptake of SARS-CoV-2 by alveolar macrophages and inflammatory response

Human lung tissue explants infected with IAV (orange), MERS-CoV (blue), SARS-CoV (green) at $1*10^6$ PFU and SARS-CoV-2 (red) at $30*10^6$ PFU as outlined in Figure 3B was used for scSeq and combined with snSeq data from COVID-19 lung autopsy material.

(A) ScSeq and snSeq of human lung tissue explants and autopsy lungs, respectively; UMAP embedding shows major cell types.

(B) UMAP embedding shows lung explant cells positive for IAV, MERS-CoV, SARS-CoV, or SARS-CoV-2, respectively; inset displays SARS-CoV-2-positive AT2 cells (red) overlayed on ACE2-positive cells (blue).

(C) Quantification of virus-positive cells per cluster (color key as in (A)). Upper panel: comparing results before and after ambient RNA filtering; lower panel: comparing lung explants to lung autopsy material. Error bars are standard deviation, Pearson correlation values are indicated.

(D) Quantification of the host factors *ACE2, CD147/BSG, NRP1, TMPRSS2, FURIN,* and *DPP4*. Expression is averaged for all cells within one cluster of one sample, and then averaged across samples. Error bars indicate standard deviation.

(E) Induction of antiviral and inflammatory pathways: gene expression scores for relevant pathways are averaged across all cells per cluster and condition; z-scores are computed separately for explant and autopsy data.

Further analysis is presented in Figure S6.

Figure 7

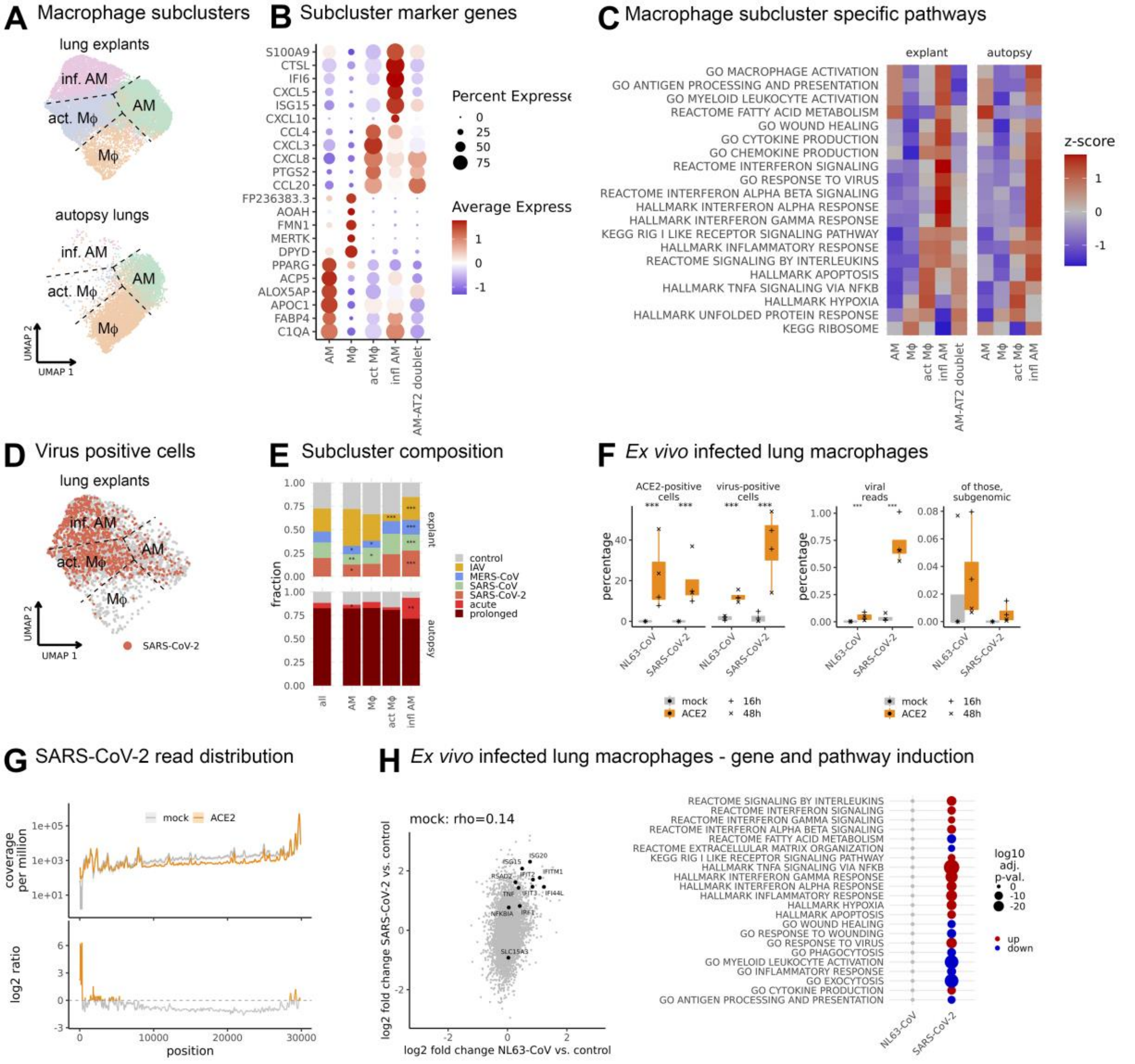

Figure 7. Single-cell RNA sequencing reveals inflammatory response of alveolar macrophages (AM) and non-productive uptake in the absence of ACE2

Subclustering of macrophages from Figure 6, and analysis of isolated lung macrophages infected *ex vivo* with SARS-CoV-2 (30*10^6 PFU) and NL63-CoV (1*10^6 PFU).

(A) Subclustering of macrophages reveals 4 subpopulations. Dashed lines serve as a guide to the eye.

(B) Expression of the top 5 marker genes for each subcluster in (A).

(C) Gene expression scores for marker-associated pathways from (B). Scores are averaged across all cells per subcluster and z-scores are computed separately for explant and autopsy data.

(D) SARS-CoV-2-positive cells in macrophages from lung tissue explants.

(E) Compositional changes of macrophage subclusters. P-values from a mixed-effects binomial model. *** $p < 0.001$, ** $p < 0.01$, * $p < 0.05$.

(F) *Ex vivo* infected lung macrophages. Left panel: percentage of ACE2- or virus-positive cells infected with NL63-CoV or SARS-CoV-2 under mock treatment or ACE2 overexpression, respectively. Right panel: viral reads (as percentage of total) and subgenomic reads (as percentage of viral) for NL63-CoV and SARS-CoV-2, respectively. P-values from binomial model. *** $p < 0.001$.

(G) Distribution of reads mapping to the SARS-CoV-2 genome for *ex vivo* infected AM under mock treatment or ACE2 overexpression. Top panel: coverage per million mapped reads smoothed with 10 nt moving average. Shaded area indicates mean ± SEM across replicates. Bottom panel: log2 ratio between ACE2 and mock conditions.

(H) Differential gene expression and pathway analysis for mock-treated *ex vivo* infected lung macrophages. Left panel: log2 fold change for NL63-CoV vs. control plotted against log2 fold change for SARS-CoV-2 vs. control. Interferon-stimulated genes (adj. p-value < 0.01) are highlighted. Right panel: pathway enrichment analysis for the log2 fold changes values with tmod [98].

Further analysis is presented in Figure S7.

References

1. Bellani G, Laffey JG, Pham T, Fan E, Brochard L, Esteban A, Gattinoni L, van Haren F, Larsson A, McAuley DF, Ranieri M, Rubenfeld G, Thompson BT, Wrigge H, Slutsky AS, Pesenti A, Investigators LS, Group ET. Epidemiology, Patterns of Care, and Mortality for Patients With Acute Respiratory Distress Syndrome in Intensive Care Units in 50 Countries. *JAMA* 2016: 315(8): 788-800.
2. Cummings MJ, Baldwin MR, Abrams D, Jacobson SD, Meyer BJ, Balough EM, Aaron JG, Claassen J, Rabbani LE, Hastie J, Hochman BR, Salazar-Schicchi J, Yip NH, Brodie D, O'Donnell MR. Epidemiology, clinical course, and outcomes of critically ill adults with COVID-19 in New York City: a prospective cohort study. *Lancet* 2020: 395(10239): 1763-1770.
3. Wu C, Chen X, Cai Y, Xia J, Zhou X, Xu S, Huang H, Zhang L, Zhou X, Du C, Zhang Y, Song J, Wang S, Chao Y, Yang Z, Xu J, Zhou X, Chen D, Xiong W, Xu L, Zhou F, Jiang J, Bai C, Zheng J, Song Y. Risk Factors Associated With Acute Respiratory Distress Syndrome and Death in Patients With Coronavirus Disease 2019 Pneumonia in Wuhan, China. *JAMA Intern Med* 2020.
4. Ulloa AC, Buchan SA, Daneman N, Brown KA. Estimates of SARS-CoV-2 Omicron Variant Severity in Ontario, Canada. *JAMA* 2022.
5. Wolter N, Jassat W, Walaza S, Welch R, Moultrie H, Groome M, Amoako DG, Everatt J, Bhiman JN, Scheepers C, Tebeila N, Chiwandire N, du Plessis M, Govender N, Ismail A, Glass A, Mlisana K, Stevens W, Treurnicht FK, Makatini Z, Hsiao NY, Parboosing R, Wadula J, Hussey H, Davies MA, Boulle A, von Gottberg A, Cohen C. Early assessment of the clinical severity of the SARS-CoV-2 omicron variant in South Africa: a data linkage study. *Lancet* 2022: 399(10323): 437-446.
6. Milross L, Majo J, Cooper N, Kaye PM, Bayraktar O, Filby A, Fisher AJ. Post-mortem lung tissue: the fossil record of the pathophysiology and immunopathology of severe COVID-19. *Lancet Respir Med* 2022: 10(1): 95-106.
7. Hoffmann M, Kleine-Weber H, Schroeder S, Kruger N, Herrler T, Erichsen S, Schiergens TS, Herrler G, Wu NH, Nitsche A, Muller MA, Drosten C, Pohlmann S. SARS-CoV-2 Cell Entry Depends on ACE2 and TMPRSS2 and Is Blocked by a Clinically Proven Protease Inhibitor. *Cell* 2020: 181(2): 271-280 e278.
8. Hofmann H, Pohlmann S. Cellular entry of the SARS coronavirus. *Trends Microbiol* 2004: 12(10): 466-472.
9. Nawijn MC, Timens W. Can ACE2 expression explain SARS-CoV-2 infection of the respiratory epithelia in COVID-19? *Mol Syst Biol* 2020: 16(7): e9841.
10. Perrotta F, Matera MG, Cazzola M, Bianco A. Severe respiratory SARS-CoV2 infection: Does ACE2 receptor matter? *Respir Med* 2020: 168: 105996.
11. Zhao Y, Zhao Z, Wang Y, Zhou Y, Ma Y, Zuo W. Single-cell RNA Expression Profiling of ACE2, The Receptor of SARS-CoV-2. *Am J Respir Crit Care Med* 2020.
12. Hamming I, Timens W, Bulthuis ML, Lely AT, Navis G, van Goor H. Tissue distribution of ACE2 protein, the functional receptor for SARS coronavirus. A first step in understanding SARS pathogenesis. *J Pathol* 2004: 203(2): 631-637.
13. Jacobs M, Van Eeckhoutte HP, Wijnant SRA, Janssens W, Joos GF, Brusselle GG, Bracke KR. Increased expression of ACE2, the SARS-CoV-2 entry receptor, in alveolar and bronchial epithelium of smokers and COPD subjects. *Eur Respir J* 2020: 56(2).
14. Lee IT, Nakayama T, Wu CT, Goltsev Y, Jiang S, Gall PA, Liao CK, Shih LC, Schurch CM, McIlwain DR, Chu P, Borchard NA, Zarabanda D, Dholakia SS, Yang A, Kim D, Chen H, Kanie T, Lin CD, Tsai MH, Phillips KM, Kim R, Overdevest JB, Tyler MA, Yan CH, Lin CF, Lin YT, Bau DT, Tsay GJ, Patel ZM, Tsou YA, Tzankov A, Matter MS, Tai CJ, Yeh TH, Hwang PH, Nolan GP, Nayak JV, Jackson PK. ACE2 localizes to the respiratory cilia and is not increased by ACE inhibitors or ARBs. *Nat Commun* 2020: 11(1): 5453.
15. Li G, He X, Zhang L, Ran Q, Wang J, Xiong A, Wu D, Chen F, Sun J, Chang C. Assessing ACE2 expression patterns in lung tissues in the pathogenesis of COVID-19. *J Autoimmun* 2020: 112: 102463.
16. Pinto BGG, Oliveira AER, Singh Y, Jimenez L, Goncalves ANA, Ogava RLT, Creighton R, Schatzmann Peron JP, Nakaya HI. ACE2 Expression Is Increased in the Lungs of Patients With Comorbidities Associated With Severe COVID-19. *J Infect Dis* 2020: 222(4): 556-563.

17. Smith JC, Sausville EL, Girish V, Yuan ML, Vasudevan A, John KM, Sheltzer JM. Cigarette Smoke Exposure and Inflammatory Signaling Increase the Expression of the SARS-CoV-2 Receptor ACE2 in the Respiratory Tract. *Dev Cell* 2020: 53(5): 514-529 e513.

18. Ziegler CGK, Allon SJ, Nyquist SK, Mbano IM, Miao VN, Tzouanas CN, Cao Y, Yousif AS, Bals J, Hauser BM, Feldman J, Muus C, Wadsworth MH, 2nd, Kazer SW, Hughes TK, Doran B, Gatter GJ, Vukovic M, Taliaferro F, Mead BE, Guo Z, Wang JP, Gras D, Plaisant M, Ansari M, Angelidis I, Adler H, Sucre JMS, Taylor CJ, Lin B, Waghray A, Mitsialis V, Dwyer DF, Buchheit KM, Boyce JA, Barrett NA, Laidlaw TM, Carroll SL, Colonna L, Tkachev V, Peterson CW, Yu A, Zheng HB, Gideon HP, Winchell CG, Lin PL, Bingle CD, Snapper SB, Kropski JA, Theis FJ, Schiller HB, Zaragosi LE, Barbry P, Leslie A, Kiem HP, Flynn JL, Fortune SM, Berger B, Finberg RW, Kean LS, Garber M, Schmidt AG, Lingwood D, Shalek AK, Ordovas-Montanes J, lung-network@humancellatlas.org HCALBNEa, Network HCALB. SARS-CoV-2 Receptor ACE2 Is an Interferon-Stimulated Gene in Human Airway Epithelial Cells and Is Detected in Specific Cell Subsets across Tissues. *Cell* 2020: 181(5): 1016-1035 e1019.

19. Hikmet F, Mear L, Edvinsson A, Micke P, Uhlen M, Lindskog C. The protein expression profile of ACE2 in human tissues. *Mol Syst Biol* 2020: 16(7): e9610.

20. Hou YJ, Okuda K, Edwards CE, Martinez DR, Asakura T, Dinnon KH, 3rd, Kato T, Lee RE, Yount BL, Mascenik TM, Chen G, Olivier KN, Ghio A, Tse LV, Leist SR, Gralinski LE, Schafer A, Dang H, Gilmore R, Nakano S, Sun L, Fulcher ML, Livraghi-Butrico A, Nicely NI, Cameron M, Cameron C, Kelvin DJ, de Silva A, Margolis DM, Markmann A, Bartelt L, Zumwalt R, Martinez FJ, Salvatore SP, Borczuk A, Tata PR, Sontake V, Kimple A, Jaspers I, O'Neal WK, Randell SH, Boucher RC, Baric RS. SARS-CoV-2 Reverse Genetics Reveals a Variable Infection Gradient in the Respiratory Tract. *Cell* 2020: 182(2): 429-446 e414.

21. Ortiz ME, Thurman A, Pezzulo AA, Leidinger MR, Klesney-Tait JA, Karp PH, Tan P, Wohlford-Lenane C, McCray PB, Jr., Meyerholz DK. Heterogeneous expression of the SARS-Coronavirus-2 receptor ACE2 in the human respiratory tract. *EBioMedicine* 2020: 60: 102976.

22. Lukassen S, Chua RL, Trefzer T, Kahn NC, Schneider MA, Muley T, Winter H, Meister M, Veith C, Boots AW, Hennig BP, Kreuter M, Conrad C, Eils R. SARS-CoV-2 receptor ACE2 and TMPRSS2 are primarily expressed in bronchial transient secretory cells. *EMBO J* 2020: 39(10): e105114.

23. Muus C, Luecken MD, Eraslan G, Sikkema L, Waghray A, Heimberg G, Kobayashi Y, Vaishnav ED, Subramanian A, Smillie C, Jagadeesh KA, Duong ET, Fiskin E, Triglia ET, Ansari M, Cai P, Lin B, Buchanan J, Chen S, Shu J, Haber AL, Chung H, Montoro DT, Adams T, Aliee H, Allon SJ, Andrusivova Z, Angelidis I, Ashenberg O, Bassler K, Becavin C, Benhar I, Bergenstrahle J, Bergenstrahle L, Bolt L, Braun E, Bui LT, Callori S, Chaffin M, Chichelnitskiy E, Chiou J, Conlon TM, Cuoco MS, Cuomo ASE, Deprez M, Duclos G, Fine D, Fischer DS, Ghazanfar S, Gillich A, Giotti B, Gould J, Guo M, Gutierrez AJ, Habermann AC, Harvey T, He P, Hou X, Hu L, Hu Y, Jaiswal A, Ji L, Jiang P, Kapellos TS, Kuo CS, Larsson L, Leney-Greene MA, Lim K, Litvinukova M, Ludwig LS, Lukassen S, Luo W, Maatz H, Madissoon E, Mamanova L, Manakongtreecheep K, Leroy S, Mayr CH, Mbano IM, McAdams AM, Nabhan AN, Nyquist SK, Penland L, Poirion OB, Poli S, Qi C, Queen R, Reichart D, Rosas I, Schupp JC, Shea CV, Shi X, Sinha R, Sit RV, Slowikowski K, Slyper M, Smith NP, Sountoulidis A, Strunz M, Sullivan TB, Sun D, Talavera-Lopez C, Tan P, Tantivit J, Travaglini KJ, Tucker NR, Vernon KA, Wadsworth MH, Waldman J, Wang X, Xu K, Yan W, Zhao W, Ziegler CGK, Consortium NL, Human Cell Atlas Lung Biological N. Single-cell meta-analysis of SARS-CoV-2 entry genes across tissues and demographics. *Nat Med* 2021: 27(3): 546-559.

24. Zou X, Chen K, Zou J, Han P, Hao J, Han Z. Single-cell RNA-seq data analysis on the receptor ACE2 expression reveals the potential risk of different human organs vulnerable to 2019-nCoV infection. *Front Med* 2020: 14(2): 185-192.

25. Chu H, Chan JF, Wang Y, Yuen TT, Chai Y, Hou Y, Shuai H, Yang D, Hu B, Huang X, Zhang X, Cai JP, Zhou J, Yuan S, Kok KH, To KK, Chan IH, Zhang AJ, Sit KY, Au WK, Yuen KY. Comparative replication and immune activation profiles of SARS-CoV-2 and SARS-CoV in human lungs: an ex vivo study with implications for the pathogenesis of COVID-19. *Clin Infect Dis* 2020.

26. Hui KPY, Cheung MC, Perera R, Ng KC, Bui CHT, Ho JCW, Ng MMT, Kuok DIT, Shih KC, Tsao SW, Poon LLM, Peiris M, Nicholls JM, Chan MCW. Tropism, replication competence, and innate immune responses of the coronavirus SARS-CoV-2 in human respiratory tract and conjunctiva: an analysis in ex-vivo and in-vitro cultures. *Lancet Respir Med* 2020: 8(7): 687-695.

27. Grant RA, Morales-Nebreda L, Markov NS, Swaminathan S, Querrey M, Guzman ER, Abbott DA, Donnelly HK, Donayre A, Goldberg IA, Klug ZM, Borkowski N, Lu Z, Kihshen H, Politanska Y, Sichizya L, Kang M, Shilatifard A, Qi C, Lomasney JW, Argento AC, Kruser JM, Malsin ES, Pickens CO, Smith SB, Walter JM, Pawlowski AE, Schneider D, Nannapaneni P, Abdala-Valencia H, Bharat A, Gottardi CJ, Budinger GRS, Misharin AV, Singer BD, Wunderink RG, Investigators NSS. Circuits between infected macrophages and T cells in SARS-CoV-2 pneumonia. *Nature* 2021: 590(7847): 635-641.

28. Group RC, Horby P, Lim WS, Emberson JR, Mafham M, Bell JL, Linsell L, Staplin N, Brightling C, Ustianowski A, Elmahi E, Prudon B, Green C, Felton T, Chadwick D, Rege K, Fegan C, Chappell LC, Faust SN, Jaki T, Jeffery K, Montgomery A, Rowan K, Juszczak E, Baillie JK, Haynes R, Landray MJ. Dexamethasone in Hospitalized Patients with Covid-19. *N Engl J Med* 2021: 384(8): 693-704.

29. Horby P, Lim WS, Emberson JR, Mafham M, Bell JL, Linsell L, Staplin N, Brightling C, Ustianowski A, Elmahi E, Prudon B, Green C, Felton T, Chadwick D, Rege K, Fegan C, Chappell LC, Faust SN, Jaki T, Jeffery K, Montgomery A, Rowan K, Juszczak E, Baillie JK, Haynes R, Landray MJ. Dexamethasone in Hospitalized Patients with Covid-19 - Preliminary Report. *N Engl J Med* 2020.

30. Tomazini BM, Maia IS, Cavalcanti AB, Berwanger O, Rosa RG, Veiga VC, Avezum A, Lopes RD, Bueno FR, Silva M, Baldassare FP, Costa ELV, Moura RAB, Honorato MO, Costa AN, Damiani LP, Lisboa T, Kawano-Dourado L, Zampieri FG, Olivato GB, Righy C, Amendola CP, Roepke RML, Freitas DHM, Forte DN, Freitas FGR, Fernandes CCF, Melro LMG, Junior GFS, Morais DC, Zung S, Machado FR, Azevedo LCP, Investigators CC-BI. Effect of Dexamethasone on Days Alive and Ventilator-Free in Patients With Moderate or Severe Acute Respiratory Distress Syndrome and COVID-19: The CoDEX Randomized Clinical Trial. *JAMA* 2020: 324(13): 1307-1316.

31. Group CST, Munch MW, Myatra SN, Vijayaraghavan BKT, Saseedharan S, Benfield T, Wahlin RR, Rasmussen BS, Andreasen AS, Poulsen LM, Cioccari L, Khan MS, Kapadia F, Divatia JV, Brochner AC, Bestle MH, Helleberg M, Michelsen J, Padmanaban A, Bose N, Moller A, Borawake K, Kristiansen KT, Shukla U, Chew MS, Dixit S, Ulrik CS, Amin PR, Chawla R, Wamberg CA, Shah MS, Darfelt IS, Jorgensen VL, Smitt M, Granholm A, Kjaer MN, Moller MH, Meyhoff TS, Vesterlund GK, Hammond NE, Micallef S, Bassi A, John O, Jha A, Cronhjort M, Jakob SM, Gluud C, Lange T, Kadam V, Marcussen KV, Hollenberg J, Hedman A, Nielsen H, Schjorring OL, Jensen MQ, Leistner JW, Jonassen TB, Kristensen CM, Clapp EC, Hjortso CJS, Jensen TS, Halstad LS, Bak ERB, Zaabalawi R, Metcalf-Clausen M, Abdi S, Hatley EV, Aksnes TS, Gleipner-Andersen E, Alarcon AF, Yamin G, Heymowski A, Berggren A, La Cour K, Weihe S, Pind AH, Engstrom J, Jha V, Venkatesh B, Perner A. Effect of 12 mg vs 6 mg of Dexamethasone on the Number of Days Alive Without Life Support in Adults With COVID-19 and Severe Hypoxemia: The COVID STEROID 2 Randomized Trial. *JAMA* 2021: 326(18): 1807-1817.

32. Pfefferle S, Krahling V, Ditt V, Grywna K, Muhlberger E, Drosten C. Reverse genetic characterization of the natural genomic deletion in SARS-Coronavirus strain Frankfurt-1 open reading frame 7b reveals an attenuating function of the 7b protein in-vitro and in-vivo. *Virol J* 2009: 6: 131.

33. Muth D, Meyer B, Niemeyer D, Schroeder S, Osterrieder N, Muller MA, Drosten C. Transgene expression in the genome of Middle East respiratory syndrome coronavirus based on a novel reverse genetics system utilizing Red-mediated recombination cloning. *J Gen Virol* 2017: 98(10): 2461-2469.

34. Tosti L, Hang Y, Debnath O, Tiesmeyer S, Trefzer T, Steiger K, Ten FW, Lukassen S, Ballke S, Kuhl AA, Spieckermann S, Bottino R, Ishaque N, Weichert W, Kim SK, Eils R, Conrad C. Single nucleus and in situ RNA sequencing reveals cell topographies in the human pancreas. *Gastroenterology* 2020.

35. Osterrieder N, Bertzbach LD, Dietert K, Abdelgawad A, Vladimirova D, Kunec D, Hoffmann D, Beer M, Gruber AD, Trimpert J. Age-Dependent Progression of SARS-CoV-2 Infection in Syrian Hamsters. *Viruses* 2020: 12(7).

36. Legland D, Arganda-Carreras I, Andrey P. MorphoLibJ: integrated library and plugins for mathematical morphology with ImageJ. *Bioinformatics* 2016: 32(22): 3532-3534.

37. Contesso G, Mouriesse H. [Anatomopathologic consensus for defining the prognostic factors of breast cancers]. *Pathol Biol (Paris)* 1990: 38(8): 834-835.

38. Jackson CB, Farzan M, Chen B, Choe H. Mechanisms of SARS-CoV-2 entry into cells. *Nat Rev Mol Cell Biol* 2022: 23(1): 3-20.

39. Travaglini KJ, Nabhan AN, Penland L, Sinha R, Gillich A, Sit RV, Chang S, Conley SD, Mori Y, Seita J, Berry GJ, Shrager JB, Metzger RJ, Kuo CS, Neff N, Weissman IL, Quake SR, Krasnow MA. A molecular cell atlas of the human lung from single-cell RNA sequencing. *Nature* 2020: 587(7835): 619-625.

40. Gu Y, Cao J, Zhang X, Gao H, Wang Y, Wang J, He J, Jiang X, Zhang J, Shen G, Yang J, Zheng X, Hu G, Zhu Y, Du S, Zhu Y, Zhang R, Xu J, Lan F, Qu D, Xu G, Zhao Y, Gao D, Xie Y, Luo M, Lu Z. Receptome profiling identifies KREMEN1 and ASGR1 as alternative functional receptors of SARS-CoV-2. *Cell Res* 2022: 32(1): 24-37.

41. Nienhold R, Ciani Y, Koelzer VH, Tzankov A, Haslbauer JD, Menter T, Schwab N, Henkel M, Frank A, Zsikla V, Willi N, Kempf W, Hoyler T, Barbareschi M, Moch H, Tolnay M, Cathomas G, Demichelis F, Junt T, Mertz KD. Two distinct immunopathological profiles in autopsy lungs of COVID-19. *Nat Commun* 2020: 11(1): 5086.

42. Singh M, Bansal V, Feschotte C. A Single-Cell RNA Expression Map of Human Coronavirus Entry Factors. *Cell Rep* 2020: 32(12): 108175.

43. Ulrich H, Pillat MM. CD147 as a Target for COVID-19 Treatment: Suggested Effects of Azithromycin and Stem Cell Engagement. *Stem Cell Rev Rep* 2020: 16(3): 434-440.

44. Mizuiri S, Ohashi Y. ACE and ACE2 in kidney disease. *World J Nephrol* 2015: 4(1): 74-82.

45. Berg J, Zscheppang K, Fatykhova D, Tonnies M, Bauer TT, Schneider P, Neudecker J, Ruckert JC, Eggeling S, Schimek M, Gruber AD, Suttorp N, Hippenstiel S, Hocke AC. Tyk2 as a target for immune regulation in human viral/bacterial pneumonia. *Eur Respir J* 2017: 50(1).

46. Hocke AC, Becher A, Knepper J, Peter A, Holland G, Tonnies M, Bauer TT, Schneider P, Neudecker J, Muth D, Wendtner CM, Ruckert JC, Drosten C, Gruber AD, Laue M, Suttorp N, Hippenstiel S, Wolff T. Emerging human middle East respiratory syndrome coronavirus causes widespread infection and alveolar damage in human lungs. *Am J Respir Crit Care Med* 2013: 188(7): 882-886.

47. Weinheimer VK, Becher A, Tonnies M, Holland G, Knepper J, Bauer TT, Schneider P, Neudecker J, Ruckert JC, Szymanski K, Temmesfeld-Wollbrueck B, Gruber AD, Bannert N, Suttorp N, Hippenstiel S, Wolff T, Hocke AC. Influenza A viruses target type II pneumocytes in the human lung. *J Infect Dis* 2012: 206(11): 1685-1694.

48. Elezkurtaj S, Greuel S, Ihlow J, Michaelis E, Bischoff P, Kunze CA, Sinn BV, Gerhold M, Hauptmann K, Ingold-Heppner B, Miller F, Herbst H, Corman VM, Martin H, Heppner FL, Horst D. Causes of Death and Comorbidities in Patients with COVID-19. *medRxiv* 2020: 2020.2006.2015.20131540.

49. Alexandersen S, Chamings A, Bhatta TR. SARS-CoV-2 genomic and subgenomic RNAs in diagnostic samples are not an indicator of active replication. *Nat Commun* 2020: 11(1): 6059.

50. Delorey TM, Ziegler CGK, Heimberg G, Normand R, Yang Y, Segerstolpe A, Abbondanza D, Fleming SJ, Subramanian A, Montoro DT, Jagadeesh KA, Dey KK, Sen P, Slyper M, Pita-Juarez YH, Phillips D, Biermann J, Bloom-Ackermann Z, Barkas N, Ganna A, Gomez J, Melms JC, Katsyv I, Normandin E, Naderi P, Popov YV, Raju SS, Niezen S, Tsai LT, Siddle KJ, Sud M, Tran VM, Vellarikkal SK, Wang Y, Amir-Zilberstein L, Atri DS, Beechem J, Brook OR, Chen J, Divakar P, Dorceus P, Engreitz JM, Essene A, Fitzgerald DM, Fropf R, Gazal S, Gould J, Grzyb J, Harvey T, Hecht J, Hether T, Jane-Valbuena J, Leney-Greene M, Ma H, McCabe C, McLoughlin DE, Miller EM, Muus C, Niemi M, Padera R, Pan L, Pant D, Pe'er C, Pfiffner-Borges J, Pinto CJ, Plaisted J, Reeves J, Ross M, Rudy M, Rueckert EH, Siciliano M, Sturm A, Todres E, Waghray A, Warren S, Zhang S, Zollinger DR, Cosimi L, Gupta RM, Hacohen N, Hibshoosh H, Hide W, Price AL, Rajagopal J, Tata PR, Riedel S, Szabo G, Tickle TL, Ellinor PT, Hung D, Sabeti PC, Novak R, Rogers R, Ingber DE, Jiang ZG, Juric D, Babadi M, Farhi SL, Izar B, Stone JR, Vlachos IS, Solomon IH, Ashenberg O, Porter CBM, Li B, Shalek AK, Villani AC, Rozenblatt-Rosen O, Regev A. COVID-19 tissue atlases reveal SARS-CoV-2 pathology and cellular targets. *Nature* 2021: 595(7865): 107-113.

51. Fleming SJ, Marioni JC, Babadi M. CellBender remove-background: a deep generative model for unsupervised removal of background noise from scRNA-seq datasets. *bioRxiv* 2019: 791699.

52. Cantuti-Castelvetri L, Ojha R, Pedro LD, Djannatian M, Franz J, Kuivanen S, Kallio K, Kaya T, Anastasina M, Smura T, Levanov L, Szirovicza L, Tobi A, Kallio-Kokko H, Österlund P, Joensuu M, Meunier FA, Butcher S, Winkler MS, Mollenhauer B, Helenius A, Gokce O, Teesalu T, Hepojoki J, Vapalahti O, Stadelmann C, Balistreri G, Simons M. Neuropilin-1 facilitates SARS-CoV-2 cell entry and provides a possible pathway into the central nervous system. *bioRxiv* 2020: 2020.2006.2007.137802.

53. Daly JL, Simonetti B, Klein K, Chen KE, Williamson MK, Anton-Plagaro C, Shoemark DK, Simon-Gracia L, Bauer M, Hollandi R, Greber UF, Horvath P, Sessions RB, Helenius A, Hiscox JA, Teesalu T, Matthews DA, Davidson AD, Collins BM, Cullen PJ, Yamauchi Y. Neuropilin-1 is a host factor for SARS-CoV-2 infection. *Science* 2020: 370(6518): 861-865.

54. Raj VS, Mou H, Smits SL, Dekkers DH, Muller MA, Dijkman R, Muth D, Demmers JA, Zaki A, Fouchier RA, Thiel V, Drosten C, Rottier PJ, Osterhaus AD, Bosch BJ, Haagmans BL. Dipeptidyl peptidase 4 is a functional receptor for the emerging human coronavirus-EMC. *Nature* 2013: 495(7440): 251-254.

55. Bost P, Giladi A, Liu Y, Bendjelal Y, Xu G, David E, Blecher-Gonen R, Cohen M, Medaglia C, Li H, Deczkowska A, Zhang S, Schwikowski B, Zhang Z, Amit I. Host-Viral Infection Maps Reveal Signatures of Severe COVID-19 Patients. *Cell* 2020: 181(7): 1475-1488 e1412.

56. Morse C, Tabib T, Sembrat J, Buschur KL, Bittar HT, Valenzi E, Jiang Y, Kass DJ, Gibson K, Chen W, Mora A, Benos PV, Rojas M, Lafyatis R. Proliferating SPP1/MERTK-expressing macrophages in idiopathic pulmonary fibrosis. *Eur Respir J* 2019: 54(2).

57. Aibar S, Gonzalez-Blas CB, Moerman T, Huynh-Thu VA, Imrichova H, Hulselmans G, Rambow F, Marine JC, Geurts P, Aerts J, van den Oord J, Atak ZK, Wouters J, Aerts S. SCENIC: single-cell regulatory network inference and clustering. *Nat Methods* 2017: 14(11): 1083-1086.

58. Liao M, Liu Y, Yuan J, Wen Y, Xu G, Zhao J, Cheng L, Li J, Wang X, Wang F, Liu L, Amit I, Zhang S, Zhang Z. Single-cell landscape of bronchoalveolar immune cells in patients with COVID-19. *Nat Med* 2020: 26(6): 842-844.

59. Wendisch D, Dietrich O, Mari T, von Stillfried S, Ibarra IL, Mittermaier M, Mache C, Chua RL, Knoll R, Timm S, Brumhard S, Krammer T, Zauber H, Hiller AL, Pascual-Reguant A, Mothes R, Bulow RD, Schulze J, Leipold AM, Djudjaj S, Erhard F, Geffers R, Pott F, Kazmierski J, Radke J, Pergantis P, Bassler K, Conrad C, Aschenbrenner AC, Sawitzki B, Landthaler M, Wyler E, Horst D, Deutsche C-OI, Hippenstiel S, Hocke A, Heppner FL, Uhrig A, Garcia C, Machleidt F, Herold S, Elezkurtaj S, Thibeault C, Witzenrath M, Cochain C, Suttorp N, Drosten C, Goffinet C, Kurth F, Schultze JL, Radbruch H, Ochs M, Eils R, Muller-Redetzky H, Hauser AE, Luecken MD, Theis FJ, Conrad C, Wolff T, Boor P, Selbach M, Saliba AE, Sander LE. SARS-CoV-2 infection triggers profibrotic macrophage responses and lung fibrosis. *Cell* 2021: 184(26): 6243-6261 e6227.

60. Hofmann H, Pyrc K, van der Hoek L, Geier M, Berkhout B, Pohlmann S. Human coronavirus NL63 employs the severe acute respiratory syndrome coronavirus receptor for cellular entry. *Proc Natl Acad Sci U S A* 2005: 102(22): 7988-7993.

61. Aguiar JA, Tremblay BJ, Mansfield MJ, Woody O, Lobb B, Banerjee A, Chandiramohan A, Tiessen N, Cao Q, Dvorkin-Gheva A, Revill S, Miller MS, Carlsten C, Organ L, Joseph C, John A, Hanson P, Austin RC, McManus BM, Jenkins G, Mossman K, Ask K, Doxey AC, Hirota JA. Gene expression and in situ protein profiling of candidate SARS-CoV-2 receptors in human airway epithelial cells and lung tissue. *Eur Respir J* 2020: 56(3).

62. Onabajo OO, Banday AR, Yan W, Obajemu A, Stanifer ML, Santer DM, Florez-Vargas O, Piontkivska H, Vargas J, Kee C, Tyrrell DLJ, Mendoza JL, Boulant S, Prokunina-Olsson L. Interferons and viruses induce a novel primate-specific isoform dACE2 and not the SARS-CoV-2 receptor ACE2. *bioRxiv* 2020.

63. Garcia-Nicolas O, V'Kovski P, Zettl F, Zimmer G, Thiel V, Summerfield A. No Evidence for Human Monocyte-Derived Macrophage Infection and Antibody-Mediated Enhancement of SARS-CoV-2 Infection. *Front Cell Infect Microbiol* 2021: 11: 644574.

64. Jiang M, Kolehmainen P, Kakkola L, Maljanen S, Melen K, Smura T, Julkunen I, Osterlund P. SARS-CoV-2 Isolates Show Impaired Replication in Human Immune Cells but Differential Ability to Replicate and Induce Innate Immunity in Lung Epithelial Cells. *Microbiol Spectr* 2021: 9(1): e0077421.

65. Zheng J, Wang Y, Li K, Meyerholz DK, Allamargot C, Perlman S. Severe Acute Respiratory Syndrome Coronavirus 2-Induced Immune Activation and Death of Monocyte-Derived Human Macrophages and Dendritic Cells. *J Infect Dis* 2021: 223(5): 785-795.

66. Wang S, Yao X, Ma S, Ping Y, Fan Y, Sun S, He Z, Shi Y, Sun L, Xiao S, Song M, Cai J, Li J, Tang R, Zhao L, Wang C, Wang Q, Zhao L, Hu H, Liu X, Sun G, Chen L, Pan G, Chen H, Li Q, Zhang P, Xu Y, Feng H, Zhao GG, Wen T, Yang Y, Huang X, Li W, Liu Z, Wang H, Wu H, Hu B, Ren Y, Zhou Q, Qu J, Zhang W,

Liu GH, Bian XW. A single-cell transcriptomic landscape of the lungs of patients with COVID-19. *Nat Cell Biol* 2021: 23(12): 1314-1328.

67. Nouailles G, Wyler E, Pennitz P, Postmus D, Vladimirova D, Kazmierski J, Pott F, Dietert K, Muelleder M, Farztdinov V, Obermayer B, Wienhold SM, Andreotti S, Hoefler T, Sawitzki B, Drosten C, Sander LE, Suttorp N, Ralser M, Beule D, Gruber AD, Goffinet C, Landthaler M, Trimpert J, Witzenrath M. Temporal omics analysis in Syrian hamsters unravel cellular effector responses to moderate COVID-19. *Nat Commun* 2021: 12(1): 4869.

68. Cao X, Tian Y, Nguyen V, Zhang Y, Gao C, Yin R, Carver W, Fan D, Albrecht H, Cui T, Tan W. Spike Protein of SARS-CoV-2 Activates Macrophages and Contributes to Induction of Acute Lung Inflammations in Mice. *bioRxiv* 2020.

69. Hoepel W, Chen HJ, Geyer CE, Allahverdiyeva S, Manz XD, de Taeye SW, Aman J, Mes L, Steenhuis M, Griffith GR, Bonta PI, Brouwer PJM, Caniels TG, van der Straten K, Golebski K, Jonkers RE, Larsen MD, Linty F, Nouta J, van Roomen C, van Baarle F, van Drunen CM, Wolbink G, Vlaar APJ, de Bree GJ, Sanders RW, Willemsen L, Neele AE, van de Beek D, Rispens T, Wuhrer M, Bogaard HJ, van Gils MJ, Vidarsson G, de Winther M, den Dunnen J. High titers and low fucosylation of early human anti-SARS-CoV-2 IgG promote inflammation by alveolar macrophages. *Sci Transl Med* 2021: 13(596).

70. Lagger C, Ursu E, Equey A, Avelar RA, Pisco AO, Tacutu R, de Magalhães JP. scAgeCom: a murine atlas of age-related changes in intercellular communication inferred with the package scDiffCom. *bioRxiv* 2021: 2021.2008.2013.456238.

71. Biering SB, de Sousa FTG, Tjang LV, Pahmeier F, Ruan R, Blanc SF, Patel TS, Worthington CM, Glasner DR, Castillo-Rojas B, Servellita V, Lo NTN, Wong MP, Warnes CM, Sandoval DR, Clausen TM, Santos YA, Ortega V, Aguilar HC, Esko JD, Chui CY, Pak JE, Beatty PR, Harris E. SARS-CoV-2 Spike triggers barrier dysfunction and vascular leak via integrins and TGF-beta signaling. *bioRxiv* 2021.

72. Huntington KE, Carlsen L, So EY, Piesche M, Liang O, El-Deiry WS. Integrin/TGF-beta1 inhibitor GLPG-0187 blocks SARS-CoV-2 Delta and Omicron pseudovirus infection of airway epithelial cells which could attenuate disease severity. *medRxiv* 2022.

73. Perez-Garcia F, Martin-Vicente M, Rojas-Garcia RL, Castilla-Garcia L, Munoz-Gomez MJ, Hervas Fernandez I, Gonzalez Ventosa V, Vidal-Alcantara EJ, Cuadros-Gonzalez J, Bermejo-Martin JF, Resino S, Martinez I. High SARS-CoV-2 viral load and low CCL5 expression levels in the upper respiratory tract are associated with COVID-19 severity. *J Infect Dis* 2021.

74. Patterson BK, Seethamraju H, Dhody K, Corley MJ, Kazempour K, Lalezari JP, Pang AP, Sugai C, Francisco EB, Pise A, Rodrigues H, Ryou M, Wu HL, Webb GM, Park BS, Kelly S, Pourhassan N, Lelic A, Kdouh L, Herrera M, Hall E, Aklin E, Ndhlovu L, Sacha JB. Disruption of the CCL5/RANTES-CCR5 Pathway Restores Immune Homeostasis and Reduces Plasma Viral Load in Critical COVID-19. *medRxiv* 2020.

75. Campbell GR, To RK, Hanna J, Spector SA. SARS-CoV-2, SARS-CoV-1, and HIV-1 derived ssRNA sequences activate the NLRP3 inflammasome in human macrophages through a non-classical pathway. *iScience* 2021: 24(4): 102295.

76. Di Virgilio F, Dal Ben D, Sarti AC, Giuliani AL, Falzoni S. The P2X7 Receptor in Infection and Inflammation. *Immunity* 2017: 47(1): 15-31.

77. Rodrigues TS, de Sa KSG, Ishimoto AY, Becerra A, Oliveira S, Almeida L, Goncalves AV, Perucello DB, Andrade WA, Castro R, Veras FP, Toller-Kawahisa JE, Nascimento DC, de Lima MHF, Silva CMS, Caetite DB, Martins RB, Castro IA, Pontelli MC, de Barros FC, do Amaral NB, Giannini MC, Bonjorno LP, Lopes MIF, Santana RC, Vilar FC, Auxiliadora-Martins M, Luppino-Assad R, de Almeida SCL, de Oliveira FR, Batah SS, Siyuan L, Benatti MN, Cunha TM, Alves-Filho JC, Cunha FQ, Cunha LD, Frantz FG, Kohlsdorf T, Fabro AT, Arruda E, de Oliveira RDR, Louzada-Junior P, Zamboni DS. Inflammasomes are activated in response to SARS-CoV-2 infection and are associated with COVID-19 severity in patients. *J Exp Med* 2021: 218(3).

78. Zhou Y, Fei M, Zhang G, Liang WC, Lin W, Wu Y, Piskol R, Ridgway J, McNamara E, Huang H, Zhang J, Oh J, Patel JM, Jakubiak D, Lau J, Blackwood B, Bravo DD, Shi Y, Wang J, Hu HM, Lee WP, Jesudason R, Sangaraju D, Modrusan Z, Anderson KR, Warming S, Roose-Girma M, Yan M. Blockade of the Phagocytic Receptor MerTK on Tumor-Associated Macrophages Enhances P2X7R-Dependent STING Activation by Tumor-Derived cGAMP. *Immunity* 2020: 52(2): 357-373 e359.

79. Neufeldt CJ, Cerikan B, Cortese M, Frankish J, Lee JY, Plociennikowska A, Heigwer F, Prasad V, Joecks S, Burkart SS, Zander DY, Subramanian B, Gimi R, Padmanabhan S, Iyer R, Gendarme M, El Debs B, Halama N, Merle U, Boutros M, Binder M, Bartenschlager R. SARS-CoV-2 infection induces a pro-inflammatory cytokine response through cGAS-STING and NF-kappaB. *Commun Biol* 2022: 5(1): 45.

80. Di Domizio J, Gulen MF, Saidoune F, Thacker VV, Yatim A, Sharma K, Nass T, Guenova E, Schaller M, Conrad C, Goepfert C, De Leval L, von Garnier C, Berezowska S, Dubois A, Gilliet M, Ablasser A. The cGAS-STING pathway drives type I IFN immunopathology in COVID-19. *Nature* 2022.

81. Pan P, Shen M, Yu Z, Ge W, Chen K, Tian M, Xiao F, Wang Z, Wang J, Jia Y, Wang W, Wan P, Zhang J, Chen W, Lei Z, Chen X, Luo Z, Zhang Q, Xu M, Li G, Li Y, Wu J. SARS-CoV-2 N protein promotes NLRP3 inflammasome activation to induce hyperinflammation. *Nat Commun* 2021: 12(1): 4664.

82. DeDiego ML, Nieto-Torres JL, Regla-Nava JA, Jimenez-Guardeno JM, Fernandez-Delgado R, Fett C, Castano-Rodriguez C, Perlman S, Enjuanes L. Inhibition of NF-kappaB-mediated inflammation in severe acute respiratory syndrome coronavirus-infected mice increases survival. *J Virol* 2014: 88(2): 913-924.

83. Lee SM, Gai WW, Cheung TK, Peiris JS. Antiviral effect of a selective COX-2 inhibitor on H5N1 infection in vitro. *Antiviral Res* 2011: 91(3): 330-334.

84. Lee SM, Suk K, Lee WH. Myristoylated alanine-rich C kinase substrate (MARCKS) regulates the expression of proinflammatory cytokines in macrophages through activation of p38/JNK MAPK and NF-kappaB. *Cell Immunol* 2015: 296(2): 115-121.

85. Di Paolo NC, Shayakhmetov DM. Interleukin 1alpha and the inflammatory process. *Nat Immunol* 2016: 17(8): 906-913.

86. Cooper KM, Bennin DA, Huttenlocher A. The PCH family member proline-serine-threonine phosphatase-interacting protein 1 targets to the leukocyte uropod and regulates directed cell migration. *Mol Biol Cell* 2008: 19(8): 3180-3191.

87. Gally F, Kosmider B, Weaver MR, Pate KM, Hartshorn KL, Oberley-Deegan RE. FABP5 deficiency enhances susceptibility to H1N1 influenza A virus-induced lung inflammation. *Am J Physiol Lung Cell Mol Physiol* 2013: 305(1): L64-72.

88. Mittal M, Tiruppathi C, Nepal S, Zhao YY, Grzych D, Soni D, Prockop DJ, Malik AB. TNFalpha-stimulated gene-6 (TSG6) activates macrophage phenotype transition to prevent inflammatory lung injury. *Proc Natl Acad Sci U S A* 2016: 113(50): E8151-E8158.

89. Borella R, De Biasi S, Paolini A, Boraldi F, Lo Tartaro D, Mattioli M, Fidanza L, Neroni A, Caro-Maldonado A, Meschiari M, Franceschini E, Quaglino D, Guaraldi G, Bertoldi C, Sita M, Busani S, Girardis M, Mussini C, Cossarizza A, Gibellini L. Metabolic reprograming shapes neutrophil functions in severe COVID-19. *Eur J Immunol* 2021.

90. Evangelou K, Veroutis D, Paschalaki K, Foukas PG, Lagopati N, Dimitriou M, Papaspyropoulos A, Konda B, Hazapis O, Polyzou A, Havaki S, Kotsinas A, Kittas C, Tzioufas AG, de Leval L, Vassilakos D, Tsiodras S, Stripp BR, Papantonis A, Blandino G, Karakasiliotis I, Barnes PJ, Gorgoulis VG. Pulmonary infection by SARS-CoV-2 induces senescence accompanied by an inflammatory phenotype in severe COVID-19: possible implications for viral mutagenesis. *Eur Respir J* 2022.

91. Olivarria G, Lane TE. Evaluating the role of chemokines and chemokine receptors involved in coronavirus infection. *Expert Rev Clin Immunol* 2022: 18(1): 57-66.

92. Su CM, Wang L, Yoo D. Activation of NF-kappaB and induction of proinflammatory cytokine expressions mediated by ORF7a protein of SARS-CoV-2. *Sci Rep* 2021: 11(1): 13464.

93. Vora SM, Lieberman J, Wu H. Inflammasome activation at the crux of severe COVID-19. *Nat Rev Immunol* 2021: 21(11): 694-703.

94. Wong LR, Perlman S. Immune dysregulation and immunopathology induced by SARS-CoV-2 and related coronaviruses - are we our own worst enemy? *Nat Rev Immunol* 2022: 22(1): 47-56.

95. Loo J, Spittle DA, Newnham M. COVID-19, immunothrombosis and venous thromboembolism: biological mechanisms. *Thorax* 2021: 76(4): 412-420.

96. Perico L, Benigni A, Casiraghi F, Ng LFP, Renia L, Remuzzi G. Immunity, endothelial injury and complement-induced coagulopathy in COVID-19. *Nat Rev Nephrol* 2021: 17(1): 46-64.

97. Rotoli BM, Barilli A, Visigalli R, Ferrari F, Dall'Asta V. Endothelial Cell Activation by SARS-CoV-2 Spike S1 Protein: A Crosstalk between Endothelium and Innate Immune Cells. *Biomedicines* 2021: 9(9).

98. Zyla J, Marczyk M, Domaszewska T, Kaufmann SHE, Polanska J, Weiner J. Gene set enrichment for reproducible science: comparison of CERNO and eight other algorithms. *Bioinformatics* 2019: 35(24): 5146-5154.

Human lungs show limited permissiveness for SARS-CoV-2 due to scarce ACE2 levels but virus-induced expansion of inflammatory macrophages

Katja Hönzke, Benedikt Obermayer, Christin Mache, Diana Fathykova, Mirjana Kessler, Simon Dökel, Emanuel Wyler, Morris Baumgardt, Anna Löwa, Karen Hoffmann, Patrick Graff, Jessica Schulze, Maren Mieth, Katharina Hellwig, Zeynep Demir, Barbara Biere, Linda Brunotte, Angeles Mecate-Zambrano, Judith Hoppe, Melanie Dohmen, Christian Hinze, Sefer Elezkurtaj, Mario Tönnies, Torsten T. Bauer, Stephan Eggeling, Hong-Linh Tran, Paul Schneider, Jens Neudecker, Jens C. Rückert, Kai M. Schmidt-Ott, Jonas Busch, Frederick Klauschen, David Horst, Helena Radbruch, Josefine Radke, Frank Heppner, Victor M. Corman, Daniela Niemeyer, Marcel A. Müller, Christine Goffinet, Ronja Mothes, Anna Pascual-Reguant, Anja Erika Hauser, Dieter Beule, Markus Landthaler, Stephan Ludwig, Norbert Suttorp, Martin Witzenrath, Achim D. Gruber, Christian Drosten, Leif-Erik Sander, Thorsten Wolff, Stefan Hippenstiel, Andreas C. Hocke

Online data supplement

Methods

Cell cultures and lung tissue

All cell lines were incubated at 37°C and 5 % CO_2 in a humidified atmosphere. Vero (African green monkey, kidney), Calu-3 (human, lung), LLC-MK2 (Rhesus monkey, kidney epithelial) and CaCo-2 cells (homo sapiens, colon adenocarcinoma) were incubated in Dulbecco’s modified Eagle medium (Gibco) supplemented with 10 % fetal bovine serum (Capricorn Scientific), 1x non-essential amino acid solution (10x stock, Gibco) and 10 mM sodium pyruvate (Gibco). MDCKII (Dog, kidney) cells were incubated in Minimum Essential Medium (Gibco) supplemented with 10 % fetal bovine serum (Capricorn Scientific) and 2 mM L-glutamine (Life Technologies). For seeding and sub-cultivation, cells were washed with phosphate buffered saline (PBS) and detached using trypsin/EDTA solution (PAN-Biotech). Fresh lung explants were obtained from 25 patients suffering from lung carcinoma (1 case metastatic osteo-sarcoma), who underwent lung resection at local thoracic surgeries. Lung explants from healthy patients were obtained from the International Institute for the Advancement of Medicine (IIAM, Edison, NJ). Clinical data of donors are included in Table S1. The study was approved by the ethics committee at the Charité clinic (projects EA2/079/13) and Ärztekammer Westfalen-Lippe and of the Westfälischen Wilhelms-Universität (AZ: 2016-265-f-S). Written informed consent was obtained from all patients. Tumor-free peripheral lung tissue was dissected into small pieces by scalpel (0.5 x 0.5 x 0.5 mm, 1 - 2 mg) and incubated overnight in RPMI 1640 medium (Merck Biochrom) at 37°C with 5 % CO_2 to wash off clinically applied antibiotics as described [1-3].

Primary alveolar macrophages (AM) were isolated by repeated perfusion of the human lung tissue with HBSS as described before [4]. Injected liquid was carefully pressed out of the tissue, collected and centrifuged (340 g, 12 min, RT). AM were infected immediately after isolation or used for Lentiviral delivery of an ACE2 expression plasmid (BPS Bioscience). Cells were seeded in 12-well plates at 0.5 x 10^6 cells/well in RPMI 1640 medium (supplemented with 2 % FCS).

Human ACE2 (kindly provided by Stefan Pöhlmann, DPZ Göttingen) was cloned into pAD-CMV-V5-DEST using the Gateway cloning procedure by Invitrogen. The final expression clone was linearized by PacI-digestion and virus production was carried out in HER-911 helper cells. Purification was done by ultracentrifugation and the recombinant adenovirus (4 x 10^{13}cfu/ml) was used to transduce human lung tissue explants or AM 24 h before infection using TransDux™ MAX Lentivirus Transduction Reagent.

Lung organoids

For generation of adult stem cell-derived lung organoids, primary cells were isolated from healthy parts of distal lung tissue obtained from lung cancer patients undergoing tumor resection surgery. The tissue was chopped with scissors into small pieces and transferred to an enzyme mixture containing 500 U/mL collagenase I (Gibco), 5 U/mL dispase II (Gibco) and 1 U/mL DNase (Applichem) in HBSS supplemented with 10 µM Y-27632 dihydrochloride (Tocris). The minced tissue was incubated for 45-60 min in a shaking water bath at 37°C before being vigorously vortexed and passed through a sieve to remove undigested tissue residues. Subsequently, the cells were further filtered through 100, and 70 µm cell strainers. Cells were centrifuged (300 x g, 5 min), resuspended in red blood cell lysis buffer (Invitrogen) and incubated for 5 min at RT. Subsequently, cells were washed with ADF++ (Advanced DMEM/F12 (Invitrogen) with 10 mM HEPES (Invitrogen) and 1x GlutaMax (Invitrogen)) supplemented with 5% FCS (Capricorn Scientific).

For the generation of alveolar organoids, HTII-280+ cells were isolated using FACS. Therefore, cells were resuspended in 500 µl staining buffer (ADF++ with 1x N2 (Invitrogen), 1x B27 (Invitrogen), 5 mM nicotinamide (Sigma), 1.25 mM N-acetylcysteine (Sigma), and 10 µM Y-27632) and incubated with mouse anti-HTII-280 IgM antibody (Terrace Biotech, TB-27AHT2-280, 1:50) for 30 min on ice. Upon incubation, cells were washed with 2 ml ADF++ supplemented with 5% FCS, resuspended again in 500 µL staining buffer, and incubated for 30 min on ice with the secondary goat anti-mouse IgG (H+L) A488 antibody (Thermo Fisher, A-11017, 1:500). Control without primary but secondary antibody staining was kept in parallel. Subsequently, cells were washed with 2 ml ADF++ with 5% FCS and resuspended in DPBS (Gibco) supplemented with 10 µM Y-27632 dihydrochloride and 1x B27, before being passed through a 40 µm strainer into FACS tubes. Cell sorting was performed by the FACS Core facility using a BD FACSAriaTM II cell sorter (BD Biosciences). HTII-280 sorted cells used to generate alveolar organoids as well as unsorted cells used to generate bronchial organoids were seeded in Cultrex RGF BME (bio-techne) at a concentration of ~1000 cells/µL. After solidification of the gelatinous matrix, the following medium according to Sachs et al. [5] was added on top of the cultures to induce growth of lung organoids: ADF++ supplemented with 10 % R-spondin1 conditioned medium (produced as described previously [6] using the 293T HA Rspo1-Fc cell line), 1x B27 supplement (Invitrogen), 1 x Primocin antibiotic mix (Invivogen), 1.25 mM N-acetylcysteine (Sigma), 5 mM nicotinamid (Sigma), 0.5 µM SB202190 (Sigma), 1 µM SB431542 (Merck), 100 ng/µl human Noggin (Peprotech), 100 ng/µl human FGF10 (Peprotech) and 25 ng/ml human FGF7 (Peprotech). For alveolar organoids, the described medium was additionally supplemented with CHIR99021 (Sigma, 3 µM). Y-27632 dihydrochloride (10 µM, Tocris) was added only in the first week of culture. Organoids were kept in an incubator at 37°C, 5 % CO_2. Upon growth for 2-3 weeks, the organoids were expanded by enzymatic digestion. To do so organoids were released from Cultrex RGF BME (bio-techne) with cold ADF++, centrifuged (300 x g, 5 min), incubated in TrypLE Express Enzyme (Gibco) for ~5-6 min at 37°C and briefly vortexed. After washing with ADF++, cells were resuspended in Cultrex at a ratio of 1:4 to 1:6.

Lentiviral delivery of an ACE2 expression plasmid (BPS Bioscience) into bronchial organoids was based on a previous protocol [7]. In brief, organoids were collected with cold ADF++, pelleted and resuspended in TrypLE Express Enzyme (Gibco). After incubation for 10 min at 37°C, organoids were vortexed and passed 5-10 times through a P1000 pipette tip to completely break up the organoids. The cells were washed with ADF++ containing 10 µM Y-27632 dihydrochloride and after centrifugation resuspended in a small volume (~50 µL) organoid medium supplemented with 8 µg/ml polybrene (Santa Cruz). Upon transfer to a 48-well plate, virus was added to the cells (MOI 1) and the suspension mixed by pipetting. The plate was centrifuged for 60 min, 600 x g at 32°C. After incubation for another 4 h in the incubator (37°C), cells were collected in a microcentrifuge tube, pelleted, re-seeded in Cultrex and overlaid with organoid medium.

Virus strains

Infection experiments were carried out by two independent laboratories in Berlin (Robert Koch Institute and Charité) and one external collaboration partner (Wilhelms-University in Muenster). For infection experiments with SARS-CoV-2 (Munich 929 or BavPart1) [8] and rSARS-CoV (generated in the Drosten Lab by reverse genetics based on the SARS-CoV Frankfurt-1 strain, Accession Number FJ429166.1 [9]), the isolates were propagated in Vero E6 cells. The infection experiments at the Wilhelms-University in Muenster were performed with SARS-CoV-2 FI-200 isolate strain. rMERS-CoV (generated in the Drosten Lab by reverse genetics based on the MERS-CoV strain EMC/2012, Accession Number JX869059 [10]) was propagated in Vero B4 cells. HCoV-NL63 was propagated by growing the wild-type virus on Rhesus monkey kidney epithelial cells (LLC-MK2). Infection experiments were done in RPMI 1640 medium supplemented with 10 % (or 2 % for AM) fetal bovine serum and 2 mM L-glutamine at 37°C with 5 % CO_2 under biosafety level 3 conditions with enhanced respiratory personal protection equipment.

The human seasonal influenza H3N2 virus A/Panama/2007/1999 (Pan/99[H3N2]) (further referred to IAV) strain was propagated using MDCK cells as described [3, 4]. Infection experiments were done in RPMI 1640 medium supplemented with 0.3 % bovine serum albumin and 2 mM L-glutamine at 37°C with 5 % CO_2.

Kidney tissue

Kidney tissue was collected from tumor nephrectomies (ethics approval EA4/026/18) and cut into small pieces (max. 5 mm x 5 mm). Specimen were then stored for 24 h in RNAlater at 4°C and then put in -80°C until further processing and protein isolation.

Autopsy material

25 cases of patients that had died after COVID-19 disease were included. In all cases, SARS-CoV-2 infection was confirmed by PCR testing of material from nasal and pharyngeal swabs. In 22 cases, patients had been treated at Charité – Universitätsmedizin Berlin, while 3 cases were referred from Sana Klinikum Berlin. Autopsies were performed on the legal basis of §1 SRegG BE of the autopsy act of Berlin and §25(4) of the German Infection Protection Act. This study was approved by the Ethics Committee of the Charité (EA 1/144/13 and EA2/066/20) as well as by the Charité-BIH COVID-19 research board and was in compliance with the Declaration of Helsinki. For histopathology, representative tissue samples of lungs were fixed in 4 % buffered formalin, dehydrated, paraffin embedded and sectioned with a thickness of 4 µm. Paraffin sections were processed as described in section *in situ* hybridization as well as immunohistochemistry [11].

Infection experiments and infectious particle quantification

Calu-3 cells were either mock-infected with infection medium or challenged with SARS-CoV-2, rSARS-CoV, rMERS-CoV or IAV (MOI 0.1) for 1 h at 37°C. After infection, cells were washed two times with PBS and DMEM medium was added before incubation at 37°C, 5 % CO_2. Samples were taken at the indicated time points.

Lung tissue cultures were inoculated with control medium or 1 x 10^6 or 30 x 10^6 plaque-forming units (PFU) (as indicated) of SARS-CoV-2, rSARS-CoV, rMERS-CoV or IAV for 1 h at 37°C. Infection was done in a 200 µl volume of infection or control medium per 100 mg lung tissue. Excess virus was removed by two washing steps with PBS and RPMI Medium was added before incubation at 37°C, 5 % CO_2. Samples were taken at the indicated time points.

Mature human lung organoids were collected on ice to remove remaining matrix and broken up by repeated resuspension using a disposable syringe with needle (27G). Organoid fragments were either mock-infected with infection medium (Advanced DMEM/F12 with 10 mM HEPES and 1x GlutaMax) or challenged with SARS-CoV-2 (MOI 1) for 1 h at 37°C. After infection, organoids were washed two times with PBS and resuspended in Cultrex. After incubation at 37°C, 5 % CO_2 for 30 min organoid medium (as described above) was added.

AM were infected with control medium, SARS-CoV-2 or hCoV-NL63 (MOI 30) for 1 h at 37°C. Excess virus was removed by two washing steps with PBS and RPMI medium supplemented with 2% fetal bovine serum and 2 mM L-glutamine was added before incubation at 37°C, 5 % CO_2. Samples were taken at the indicated time points.

Infectious particles were quantified by plaque titration on Vero E6 cells for SARS-CoV-2 and rSARS-CoV, on VeroB4 cells for rMERS-CoV, on CaCo-2 cells for hCoV-NL63, and MDCKII cells for IAV. Briefly, cell monolayers were seeded in 24-well plates, incubated with virus-containing cell culture supernatants and overlaid with 1.2 % Avicel in appropriate medium. After 48 h (for IAV), 72 h (for SARS-CoV and SARS-CoV-2), 96 h (for MERS-CoV), or 120 h (for hCoV-NL63) cells were washed two times with PBS and plaques were fixed and visualized by staining with crystal violet.

IFN stimulation of lung tissue

Culture medium containing recombinant human IFNβ (100 U/ml) was injected into lung explants using a disposable syringe with needle (27G). Accordingly, control explants received control medium. The tissue was processed for RNA and protein analysis after additional 24 h or 96 h.

Isolation of total RNA, cDNA synthesis and qPCR

Human lung tissue explants were stored in RNAlater™ Stabilization Solution (ThermoFisher) at 4°C until further processing. For total RNA isolation the RNeasy Mini Kit (Qiagen) was used according to manufacturer`s instructions. Human lung tissue was transferred to Lysing Matrix D tubes (MP Biomedicals) in 500 µl RLT lysis buffer supplemented with β-mercaptoethanol. Tissue was lysed using FastPrep®-24 (MP Biomedicals) applying 4 rounds of tissue lysis at default settings (6 m/s, 30 s). Cells and organoids were directly lysed in 500 µl RLT lysis buffer supplemented with β-mercaptoethanol. Homogenates were centrifuged and RNA was purified from the supernatant. 0.5 µg RNA was reverse transcribed and quantitative PCR was performed using TaqMan assays on an ABI 7300 instrument. Viral genomes and the internal reference gene c-myc were measured as described elsewhere [12, 13]. Average Ct and ΔΔCq values were calculated according to Livak et al. [14].

Bulk RNA sequencing and analysis

RNA from infected samples was purified as described above. PolyA(+) RNA sequencing libraries were constructed using the NEBNext Ultra™ II Directional RNA Library Prep Kit for Illumina (New England Biolabs) according to the manufacturer’s instruction, with 9 PCR cycles in the amplification steps, and sequenced on a Nextseq 500 device using 1x76 cycles single-end sequencing.

Reads were mapped using STAR (version 2.7.3a) with lenient parameters to detect non-canonical splice junctions [15] (--outFilterType BySJout --outFilterMultimapNmax 20 --alignSJoverhangMin 8 --outSJfilterOverhangMin 12 12 12 12 --outSJfilterCountUniqueMin 1 1 1 1 --outSJfilterCountTotalMin 1 1 1 1 --outSJfilterDistToOtherSJmin 0 0 0 0 --outFilterMismatchNmax 999 --outFilterMismatchNoverReadLmax 0.04 --scoreGapNoncan -4 --scoreGapATAC -4 --chimOutType WithinBAM HardClip --chimScoreJunctionNonGTAG 0 --alignSJstitchMismatchNmax -1 -1 -1 -1 --alignIntronMin 20 --alignIntronMax 1000000 --alignMatesGapMax 1000000). Control samples were mapped against the GRCh38 genome, infected samples against GRCh38 combined with the IAV (DQ487333.1), MERS-CoV (NC_019843.3), SARS-CoV (NC_004718.3) or SARS-CoV-2 (NC_045512.2) genomes, respectively. Gene expression was quantified with 'feature Counts' (version 2.0.0) using the Gencode v33 reference combined with viral transcripts extracted from the GenBank records. Bulk RNA sequencing differential expression analysis was performed in R (version 3.5.1) with DESeq2 (version 1.22.1), building a combined model for all 4 viral treatments and the control, donor identity as covariate, and "normal" shrinkage. A heatmap was created using regularized log-transformed counts for all differential genes in one of the 4 comparisons (adj. p-value < 0.05), after removing systematic differences between donors with limma's 'removeBatchEffect' function. Sub-genomic reads in the samples infected with MERS-CoV, SARS-CoV or SARS-CoV-2 were detected by counting reads that originate in the 5' leader sequence (defined as the first 120 nt) and have exactly one gap of at least 10 nt more than 15nt away from the read ends.

Single-cell isolation and library preparation

Individual human lung tissue samples were minced and placed in digestion medium (500 U/ml collagenase, 1.5 U/ml dispase and 1 U/ml DNAse) for 1 h at 37°C. Cells were then filtered through a 70 µm strainer and enzymatic reaction was stopped by cold RPMI with 10 % fetal bovine serum and 1 % L-glutamine. Cells were washed with 50 ml cold RPMI with 10 % fetal bovine serum and 1 % L-glutamine and red blood cells were lysed using red blood cell lysis solution (MiltenyiBiotec). Finally, cells were filtered using a 40 µm Flowmi® Cell Strainer (Millipore) and re-suspended in PBS supplemented with 2 % fetal bovine serum at the concentration of 10,000 cells/µl for scRNA-Seq. AM were detached using a cell scraper, washed two times with PBS and fixed with methanol. After rehydration cells were filtered using a 40 µm Flowmi® Cell Strainer (Millipore) and re-suspended in PBS supplemented with

2 % fetal bovine serum at the concentration of 10,000 cells/µl for scRNA-Seq. The single-cell capturing and downstream library constructions were performed using the Chromium Single Cell 3′ V3.1 library preparation kit according to the manufacturer's protocol (10x Genomics). Full-length cDNA along with cell-barcode identifiers were PCR-amplified and sequencing libraries were prepared. The constructed libraries were either sequenced on the Nextseq 500 using 28 cycles for read 1.55 cycles for read 2, and 8 index cycles, or on the Novaseq 6000 S1 using 28 cycles for read 1, 64 cycles for read 2, and 8 index cycles, to a median depth of 36000 reads per cell.

Single-nucleus isolation and library preparation

Single-nuclei were isolated from snap-frozen autopsy samples as described before [16]. Briefly samples were homogenized with one stroke of "loose" pestle in citric-acid based buffer (sucrose 0.25 M, citric acid 25 mM, Hoechst 33342 1 µg/mL) using a glass dounce tissue grinder. The tissue was incubated on ice for 5 minutes and then homogenized with 5 more strokes. After further 5 minutes of incubation, tissue was homogenized with 3 strokes using the "loose" pestle and then 5 more strokes using the "tight" pestle. Homogenate was filtered through a 35-µm cell strainer and centrifuged for 5 minutes at 500 x g at 4°C. Supernatant was removed, nuclei were resuspended in of citric acid buffer and the centrifugation step was repeated. Nuclei were then resuspended in cold resuspension buffer (KCl 25 mM, MgCl2 3 mM, Tris-buffer 50 mM, RNaseIn 0.4 U/µL, DTT 1mM, SuperaseIn 0.4 U/µL, Hoechst 33342 1 µg/mL). Nuclei were counted, diluted to the desired concentration and immediately loaded on the 10X Chromium controller. The single-cell capturing and downstream library constructions were performed using the Chromium Single Cell 3′ V3.1 library preparation kit according to the manufacturer's protocol (10x Genomics). Full-length cDNA along with cell-barcode identifiers were PCR-amplified and sequencing libraries were prepared. The constructed libraries were either sequenced on a Nextseq 500 device, using 28 cycles for read 1, 55 cycles for read 2, and 8 index cycles, or on a Novaseq 6000 S1 flowcell using 28 cycles for read 1, 64 cycles for read 2, and 8 index cycles, to a median depth of 36000 reads per cell nucleus.

Single-cell and -nuclei RNA sequencing and analysis

The Cell Ranger Software Suite (Version 3.1.0) was used to process raw sequencing data with the GRCh38 reference for the control samples, and GRCh38 augmented by the IAV

(DQ487333.1), MERS-CoV (NC_019843.3), SARS-CoV (NC_004718.3), SARS-CoV-2 (NC_045512.2) or NL63-CoV (JX504050.1) respectively. Viral transcripts including 3'UTR sequences were extracted from the Genbank records and added to the Gencode v33 reference. We used CellBender [17] to remove background RNA and scrublet [18] to identify doublets. Single-cell RNA sequencing data analysis was performed in R (version 3.6.3) with Seurat (version 3.2.1). Cells with at least 500 and less than 5000 detected genes and less than 10% mitochondrial content were combined from each library and library depth (total number of UMIs) was regressed out when scaling data. For organoid and *ex vivo* AM data we additionally regressed out cell cycle scores calculated with Seurat's CellCycleScoring function. We then integrated samples from different donors using ‘IntegrateData’ for lung explant, autopsy, organoid and *ex vivo* AM data separately. After automated clustering, DoubletFinder [19] was used to again identify likely cell doublets, and cluster annotation was performed with Seurat's ‘TransferData’ workflow using the Human Lung Cell Atlas reference dataset, using only epithelial cells for the organoid data [20]. We finally combined explant and autopsy data in another round of data integration.

Differential gene expression was analyzed using DESeq2 [21] on aggregated "pseudobulk" counts for all cells from the same sample in a cluster, using "normal" shrinkage. For lung explants, we used a combined model for the viral treatments plus control with donor identity as covariate; for autopsy samples we compared acute or prolonged cases against the control, and for *ex vivo* AM data we analyzed mock and ACE2 samples separately, with combined models for the two viral treatments plus control, and donor and timepoint as covariates. Pathway analysis was performed using tmod [22] and the Hallmark, Reactome and Gene Ontology (BP) gene sets from MSigDB (version 7.2). Gene expression within pathways was quantified using Seurat's AddModuleScore function; z-scores were calculated for each pathway across clusters but separately for lung explant and autopsy data. Differential gene expression between virus-positive and virus-negative cells within infected lung explant samples was performed using cloglog regression as in Bost et al. [23]. Briefly, we binarized gene expression and built a generalized linear model with logarithmic library size as offset, donor identity as additional covariate and cloglog link function. We filtered all genes with significant intercept coefficient ($p < 0.05$) and used Benjamini-Hochberg p-value correction for the ‘infection’ coefficient. Changes in cellular composition were analyzed using a mixed-effects binomial model, comparing the number of cells with a certain label between conditions. Viral and subgenomic read percentages in *ex vivo* AM data were compared using a binomial model with timepoint as covariate. Intercellular signaling was analyzed with scDiffCom [24], comparing acute and prolonged autopsy cases against controls. We then selected signaling interactions differential between macrophages and T cells but few other cell types. AM-AT2 doublets were identified in lung explant scSeq data before removal of doublets predicted by DoubletFinder. We used cell type predictions based on the Human Lung Cell Atlas and classified cells with prediction scores > 0.05 for both AM and AT2 identity as AM-AT2 doublets. For the comparison of macrophage subtype expression profiles, we downloaded expression data for Delorey et al. [25] from the Broad Single Cell Portal and selected non-doublet nuclei with myeloid cluster identity; for Wendisch et al. [26] we obtained "BAL_macrophages.rds" from https://nubes.helmholtz-berlin.de/s/XrM8igTzFTFSoio and matched Ensembl gene ids to gene symbols; for Grant et al. [27] we obtained "GSE155249_supplement.h5ad.gz" from GEO, converted it into a Seurat object, and kept MoAM, Prolif. AM and TRAM clusters; and for Liao et al. [28] we downloaded h5 count matrices from GEO (GSE145926), filtered cells with less than 10% mitochondrial content, less than 50000 UMIs and at least 1000 but less than 6000 genes, regressed out library size when scaling data, integrated samples using `IntegrateData`, predicted cell types using the Human Lung Cell Atlas reference, selected monocytes and macrophages, performed another round of data integration followed by clustering, and assigned macrophage subcluster identity based on expression of marker genes in their Fig. S2E. We then determined variable genes in each dataset and used AverageExpression for all genes variable in at least 4 out of 6 datasets. We used limma (v3.42.4) to remove systematic technical variation between the different datasets and computed similarity from Pearson correlations between gene-wise z-scores. SCENIC analysis was performed separately for macrophages from lung explants and autopsy data. We used arboreto with the grnboost2 method and transcription factors from HGNC to generate an adjacency matrix, followed by pyscenic ctx with hg38 refseq motifs and pyscenic aucell. We then calculated regulon specificity scores for the macrophage subclusters as described in the pySCENIC tutorial. The distribution of reads across the viral genome was inspected using coverage tracks created with bedtools genomeCoverageBed on the bam files produced by CellRanger. Coverage values were normalized by the number of reads mapping to the viral genome divided by 10^6, smoothed with a moving average in a 10 nt window, and then averaged over different samples. SARS-CoV-2 and MERS-CoV were compared by linearly interpolating coverage values in 30000 evenly spaced positions.

Western blot

For extraction of proteins, human lung explants and human kidneys were transferred into Lysing Matrix D tubes with RIPA buffer (Thermo Fisher Scientific), containing 1 x complete protease inhibitor cocktail (Sigma-Aldrich). Tissue was disrupted in a FastPrep®-24 homogenizer applying 3 rounds of tissue lysis at default settings (6 m/s, 30 s).

Organoids were washed with PBS, pelleted, lysed with RIPA buffer containing 1 x complete protease inhibitor cocktail and resuspended using a disposable syringe with needle (27G) to ensure proper lysis. Calu-3 cells and AM were harvested on ice by scraping with RIPA lysis buffer. Cell debris was removed by centrifugation. Lysates were subjected to Western blot as described previously [29]. Briefly, protein extracts were separated on a 7.5 % Mini-PROTEAN® TGX™ Precast Protein Gel (Bio-Rad) and transferred to a PVDF membrane (Merck Millipore). Gels were loaded with 100 µg protein per lane. Membranes were blocked with Odyssey blocking buffer (LI-COR Inc.) and probed with antibodies against ACE2 and actin (as a loading control). For blocking/competition of ACE2 PA5-20046 antibody was combined with a five-fold excess of blocking peptide in a 500 µl volume of PBS, followed by 2 h incubation at room temperature. The antibody/peptide mixture was added into appropriate blocking buffer and incubated over night at 4°C. Proteins were detected by incubation with HRP-conjugated IgG antibodies and Amersham ECL Prime Western Blotting System (Cytiva) or Pierce ECL Western blotting Substrate (Thermo Fisher Scientific). The membranes from each experiment were exposed to Carestream Biomax Light Film (Sigma Aldrich) for 1 sec (Figure 3D, Figure S1C and S1D), 30 sec (Figure 1E and 1G) or 10 min (Figure S2C). Densitometric analysis was performed using ImageJ (Image processing and analysis in Java, open platform). The quantification was assessed as a ratio of each protein band relative to the lane's loading control.

Immunohistochemistry

Human lung tissue samples were fixed in 4 % paraformaldehyde for 48 h, embedded in paraffin and routinely processed for histology and immunofluorescence staining as described before [1, 4, 29]. Three different SARS-CoV-2 antibodies were tested with equal results (SARS-CoV-2 Nucleocapsid Antibody, Sino Biological; SARS-CoV-2 Spike Antibody, Sino Biological, SARS-CoV-2 Spike Protein, Novux Biologicals). For human lung tissue the SARS-CoV-2

Nucleocapsid Antibody was used and for the autopsy material, Calu-3 cells and the organoids the Novux Biologicals SARS-CoV-2 Spike Antibody. Primary antibodies detecting spike protein of SARS-CoV-2, MERS nucleocapsid, occludin and ACE2 were incubated overnight at 4°C, followed by labelling with corresponding secondary antibodies. For characterization of infected cells, the established cell markers HTII-280 (alveolar type II cells, AT2), EMP2 (alveolar type I cells, AT1) and CD68 (alveolar macrophages, AM) were used, followed by incubation with corresponding secondary antibodies. Nuclei were subsequently counterstained with DAPI (Sigma Aldrich). For ACE2 antibody specificity tests following antibodies were used: AF-933; PA5-20046; GTX101395; HPA000288 and ab15348, followed by incubation with corresponding secondary antibodies (Alexa Fluor 488-conjugated anti-mouse or anti-rabbit IgG (H+L)). For blocking/competition of ACE2 PA5-20046 antibody was combined with a five-fold excess of blocking peptide in a 500 µl volume of PBS, followed by 2 h incubation at room temperature. The antibody/peptide mixture was added into appropriate blocking buffer and incubated over night at 4°C. Immunofluorescence of human lung slices was analyzed by spectral confocal microscopy using a LSM 780 [(objectives: Plan Apochromat 63x/1.40 oil DIC M27 and Plan Apochromat 63x/1.40 oil DIC M27), Carl-Zeiss, Jena, Germany]. Based on a spectral image lambda stack, linear unmixing of tissue autofluorescence and overlapping spectra of fluorochromes were performed using ZEN 2012 software (Carl-Zeiss, Jena, Germany). To reveal lung and cell morphology, images were combined with Differential Interference Contrast (DIC). To count for ACE2- and HTII-280-positive cells representative fields of view, each lung slide was scanned (400x magnification, 5 x 5 tile scans [212.5 mm x 212.5 mm each tile], ca. 1,129 mm^2/lung). All image sets were acquired using optimal configuration regarding resolution and signal to noise ratio. Images were processed using ZEN 2012.

In situ hybridization

For RNA i*n situ* hybridization (ISH), tissues were immersion fixed for 24 h in 10 % neutral buffered formalin, pH 7.0, and embedded in paraffin. Cells were suspended in 37°C 1.5 % agarose, cooled to room temperature, and similarly formalin-fixed and paraffin-embedded. Paraffin sections were cut at 2 µm and mounted on adhesive glass slides.

ISH for the detection of SARS-CoV-2 and MERS-CoV was performed using the ViewRNA ISH Tissue Assay (Invitrogen by Thermo Fisher Scientific) following the manufacturer's instructions (MAN0018633 Rev.C.0) as described [30]. Probes were designed by the manufacturer (Life

Technologies by Thermo Fisher) based on the *N-gene* and *S-gene* RNA of SARS-CoV-2 (NCBI database NC_045512.2, nucleotides 28,274 to 29,533, assay ID: VPNKRHM) and the *N-gene* and *S-gene* RNA of MERS-CoV (NC_019843.3, nucleotides 28,566 to 29,807; Assay No. VPRWENG), respectively. Commercially available probes for the human housekeeper elongation-factor 1a (EF1a; Thermo Fisher) and Bacillus subtilis dihydrodipicolinate reductase (dapB; Thermo Fisher) were used as positive or negative controls (data not shown). In addition, slides were incubated with the Probe Set Diluent QT (ViewRNA ISH Tissue Assay, see above) without probe to control for unspecific background staining. Human lung tissues were incubated at 95°C for 10 min followed by protease QF (kit content) digestion for 20 min. Embedded cells were incubated at 95°C for 5 min followed by protease QF digestion for 10 min. Following the ISH procedure, slides were counterstained with hematoxylin for 45 s and mounted with Roti Mount Fluor-Care DAPI (Carl Roth).

Fluorescence RNA ISH was performed to localize mRNA encoding angiotensin converting enzyme-2 (ACE2) and transmembrane protease, serine subtype 2 (TMPRSS2) using the RNAscope Multiplex Fluorescent Reagent Kit v2 (Advanced Cell Diagnostics, Bio-Techne) following the manufacturer’s instructions. Slides were incubated with commercially available probes for ACE2 (probe Hs-ACE2-C2; Advanced Cell Diagnostics) or TMPRSS2 (probe Hs-TMPRSS2-C2). The 3-plex positive control probe detecting the human cyclosporine-binding protein PIPB (for channel two) and the 3-plex negative control probe detecting dapB (as above, all three channels) were also included. Human lung tissues and agarose embedded cells were incubated using standard (15 min heat, 30 min protease) or mild conditions (15 min heat, 15 min protease), respectively, as described in the manufacturer´s guide. Slides were counterstained with DAPI for 30 s and mounted with Fluoromount-G (Invitrogen).

Slides of *ex vivo* human lung tissue and autopsy material used for ISH were entirely scanned using an Axio Scan Z1 Slidescanner (Zeiss) at 20x magnification [NA: 0.8] in bright field mode. Representative areas were chosen and depicted.

Image segmentation

From each COVID-19 (n = 4) and NON-COVID-19 (n = 4) HE-stained tissue slide, two regions of interest (15000 x 15000 and 20000 x 20000 pixel / 19360000 µm^2 and 10890000 µm^2, in total 30.25 mm^2) were extracted and the number of cell nuclei was determined. Cell nuclei were separated from background by manual thresholding of hue and brightness channels in an HSB representation of the colored microscopy images. Cell nuclei were separated from each other by morphological filtering and distance transform watershed using the MorphoLibJ-Plugin [31]of Fiji [32].

Multiplexed histology

Cryopreserved human tissue was cut in 5 µm sections on cover slides coated with 3-aminopropyltriethoxysilane (APES) using a MH560 cryotome. Tissue sections were fixed for 10 minutes with 2% paraformaldehyde, permeabilized with 0,2% Triton X-100 in PBS for 10 min at room temperature and blocked with 10% goat serum and 1% BSA in PBS for 20 minutes. A fluid chamber was created using "press-to-seal" silicone sheets with a 10mm circular cut-out, which was attached to the cover slip surrounding the sample.

The acquisition of multiplexed histology images was performed as previously published [33, 34] using a modified Toponome Image Cycler® MM3 (TIC) originally produced by MelTec GmbH & Co.KG Magdeburg, Germany [35]. This robotic microscopic system consists of 3 main components: (1) an inverted widefield (epi)fluorescence microscope Leica DM IRE2 equipped with a CMOS camera and a motor-controlled XY-stage, (2) CAVRO XL3000 Pipette/Diluter (Tecan GmbH, Crailsheim, Germany), and (3) a software MelTec TIC-Control for controlling microscope and pipetting system and for synchronized image acquisition. A multiplexed histology run is performed as a sequence of iterative cycles, each consisting of four steps: (i) automated pipetting of the fluorescence-coupled staining antibody onto the tissue section, incubation and subsequent washing; (ii) auto-focusing based on the cross-correlation of phase contrast images and acquisition of the fluorescence images 3-D stack (+/- 5 z-steps) in the according channels; (iii) photo-bleaching of the fluorophore; and (iv) a second auto-focusing step followed by the acquisition of a post-bleaching fluorescence image 3D stack (+/- 5 z-steps). Used antibodies are: DAPI (Roche, Cat# 10236276001), CCR2-PE (Miltenyi Biotec, Cat# 130-118-338), CXCR3-PE (Miltenyi Biotec, Cat# 130-101-379), CD68-PE (Miltenyi Biotec, Cat# 130-118-486), HLA-DR, DP, DQ-PE (Miltenyi Biotec, Cat# 130-120-715), C1q-FITC (Miltenyi Biotec, Cat# F0254), MRP14-PE (Miltenyi Biotec, Cat# 130-114-516).

Image pre-processing was conducted as previously described [34]. In short, all acquired images were aligned by cross-correlation of the phase-contrast images. Afterwards, background elimination and illumination correction of the fluorescence images was performed by subtracting the bleaching image in each cycle and focal plane from the according fluorescence image obtained in the same cycle [35] in order to remove tissue autofluorescence and potential residual signal from the previous cycle. The “Extended Depth of Field” algorithm was applied on the 3D fluorescence stack in each cycle [36]. Images normalization was performed in Fiji by a rolling ball algorithm and fluorescence intensities were scaled to the full intensity range (16 bit => 216).

Statistical analysis

GraphPad Prism 6 software was used for the statistical analysis. Data are presented as mean ± SEM of at least three donors within independent experiments. One-way ANOVA with non-parametric Friedmann test was used to compare all groups in Figure 1F and G and Figure 3A, B and C. For comparisons between two groups in Figure 1E the Mann-Whitney U test or Kruskal-Wallis H test was used. Significances are represented as *$p < 0.05$, **$p < 0.01$, or ***$p < 0.001$.

Supplementary figure legends

Figure S1

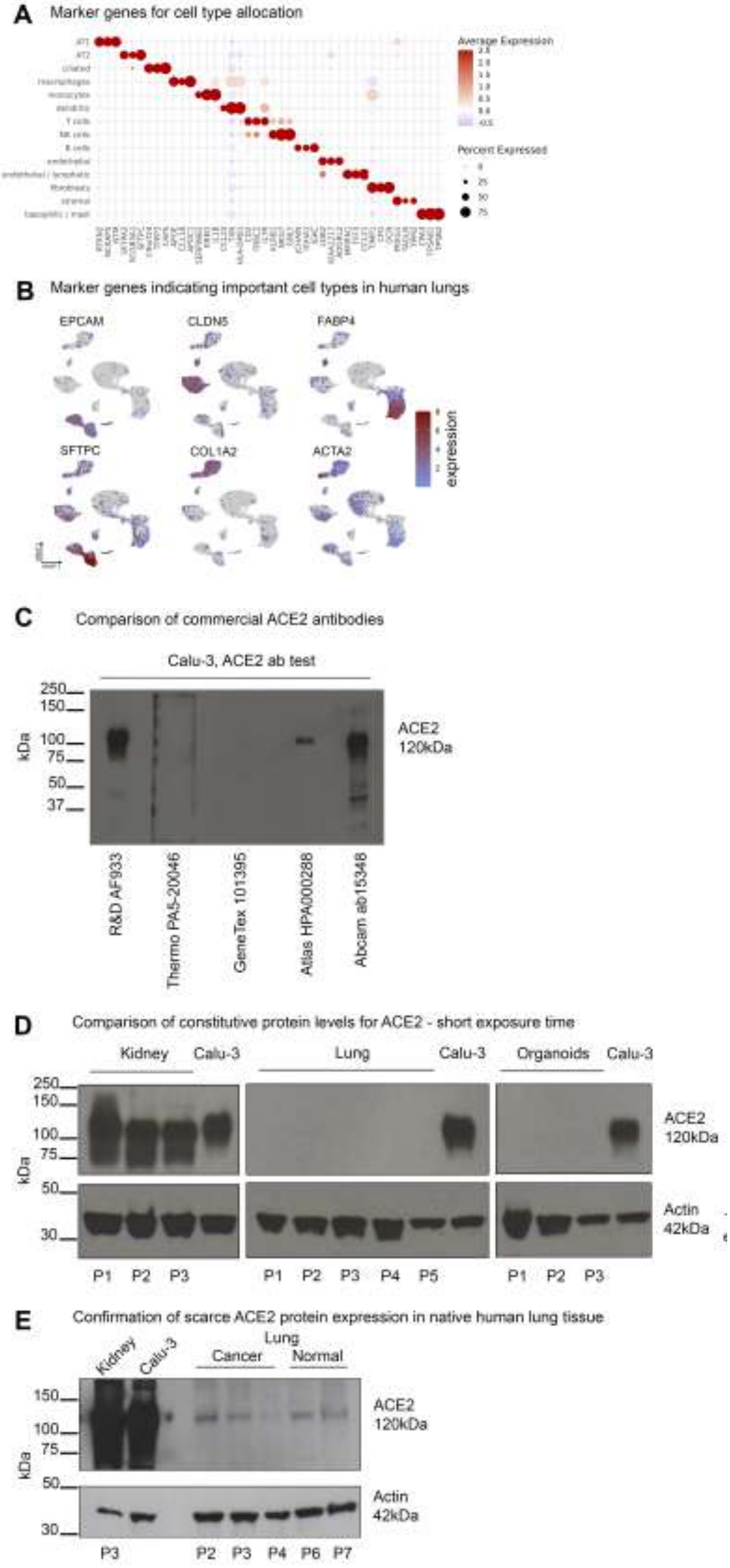

Figure S1. Cell marker genes, ACE2 antibody evaluation and western blotting

(A) Marker gene expression for cell type assignment in single-cell and single-nucleus RNA sequencing data of human lung tissue and autopsy material.

(B) Detailed view of *EPCAM* (epithelium), *CLDN5* (endothelium), *FABP4* (AM), *SFTPC* (AT2), *COL1A2* (fibroblasts) and *ACTA2* (smooth muscle cells) gene expression for corresponding cell cluster validation.

(C) Analysis of ACE2 expression by Western blot using 5 different commercial antibodies demonstrating R&D AF933 as most sensitive and specific antibody which was used for all Western blotting and immunohistochemistry analysis. Other antibodies showed either smeary bands or were insensitive until negative.

(D) Short exposure time of the membrane (1 sec) for detection of ACE2 expression by Western blot revealed no signal in human lungs and organoids. Protein lysates from human kidneys (3 donors), human lungs (5 donors), human lung organoids (3 donors) and Calu-3 cells were used. β-Actin served as loading control.

(E) Analysis of ACE2 expression by Western blot. Shown are protein lysates from human kidney (1 donors), Calu-3 cells, human lung tissue explants from cancer patients (2 donors) and “normal” human lung tissue from transplant lungs, which were originally dedicated for transplantation (2 donors). β-Actin served as loading control.

Figure S2

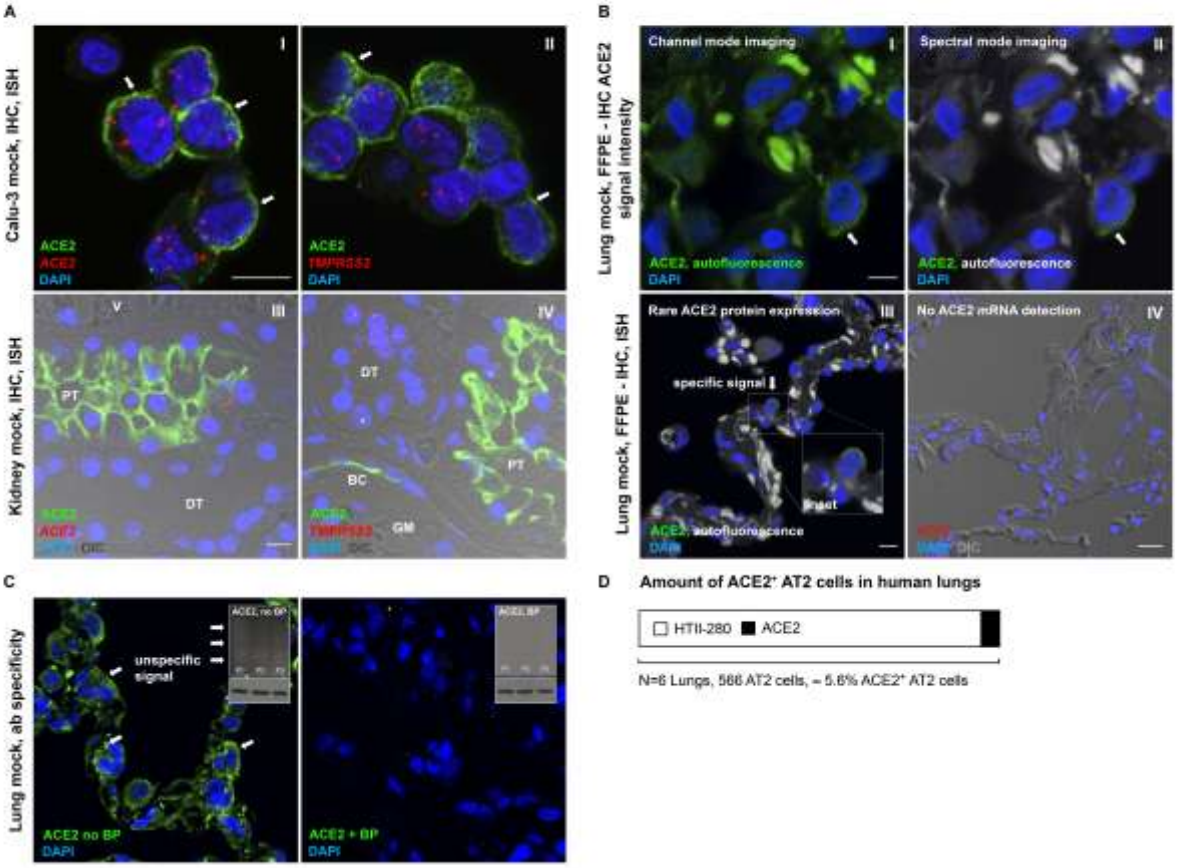

Figure S2. ACE2 antibody validation, specificity testing and determination of ACE2 in human lungs

Immunohistochemistry and *in situ* hybridization were analyzed in human lung tissue by spectral microscopy and linear unmixing.

(A) Panel I and II show Calu-3 cells, III and IV human kidneys, both embedded in paraffin. ACE2 immunostaining (green) and *in situ* hybridization (red) (panel I) and ACE2 immunostaining (green) and *TMPRSS2 in situ* hybridization (red) (panel II) in Calu-3 cells depict specific signals. ACE2 immunostaining (green) and *in situ* hybridization (red, panel III) in human kidneys demonstrate coherent expression in cells of the proximal tubuli (PT), whereas vessels (V) and distal tubuli (DT) are negative. Panel IV shows again ACE2 immunostaining (green, PT) and *TMPRSS2 in situ* hybridization (red) revealing that *TMPRSS2* is present in DT but not PT. Slight positive signal for ACE2 in squamous epithelium of the Bowman's capsule (BC) around the glomeruli (GM). Cell nuclei are visualized by DAPI stain (blue), scale bars 10 µm.

(B) Conventional, threshold based confocal microscopy of ACE2 immunostaining (green, panel I, II and III) and *in situ* hybridization (red) (panel IV) in human lung tissue. Panel I shows channel mode imaging with autofluorescence in green of the lung collagen backbone. Panel II shows the spectral mode imaging with the autofluorescence in white. Panel II shows weak ACE2 expression and panel IV no expression. ACE2-positive cells are marked by white arrows. Cell nuclei are visualized by DAPI stain (blue). Scale bar 5 µm for panel I and II and 10 µm for panel III and IV.

C) Immunostaining of ACE2 using the Thermo PA5-20046 antibody in human lung tissue. The left panel shows the unspecific antibody binding and the Western blot of 3 donor lungs a smeary expression pattern with multiple banding. The right panel shows the completely abolished ACE2 immunofluorescence and Western blot signal by use of a blocking peptide. Cell nuclei are visualized by DAPI stain (blue).

D) Cancer lungs (explants, n = 3) as well as non-cancer lungs (transplants, n = 3) were stained and spectrally unmixed for ACE2 and HTII-280 (AT2 marker). Representative ‘fields of view‘ for each lung slide were scanned (400x magnification, 5 x 5 tile scans [212.5 mm x 212.5 mm each tile], ca. 1,129 mm^2/lung) and counted for ACE2 (Alexa488) and HTII-280 (Alexa633) positive AT2 cells. A total of 566 cells were counted of which 30 were positive for ACE2 (approx. 5.6 %).

Figure S3

A Lung tissue, viral replication external validation

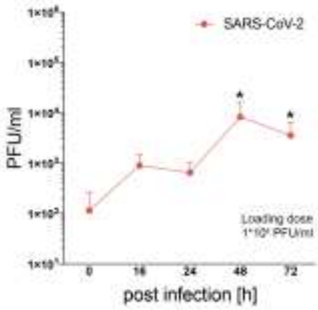

B Cell type clustering of alveolar and bronchial organoids

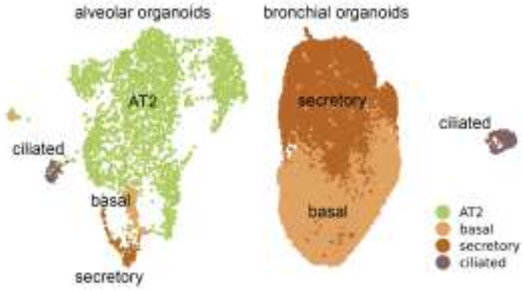

C Prototypic cell markers for organoid phenotyping

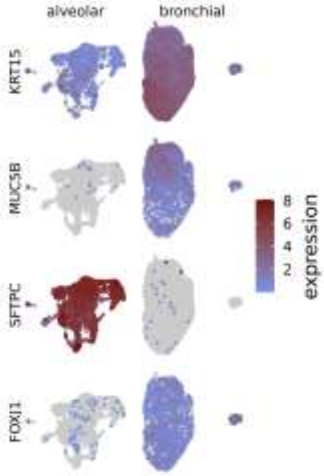

D Critical factors for SARS-CoV-2 infection in human alveolar and bronchial organoids

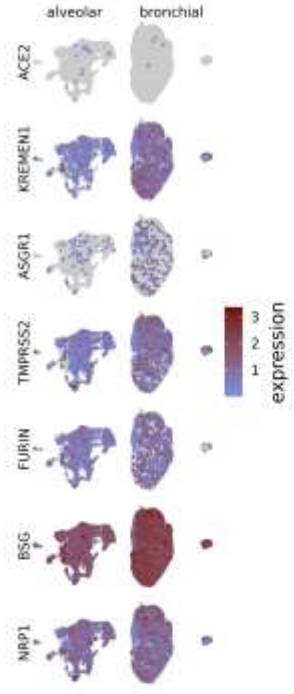

E Percentage cell types, virus- and ACE2-positve cells in alveolar and bronchial organoids

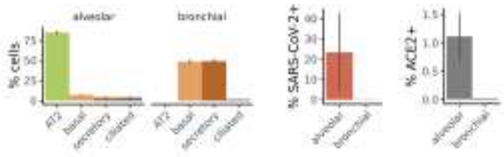

F ACE2 expression in bronchial and alveolar organoids

Figure S3. Independent external validation of low SARS-CoV-2 replication in human lungs

(A) Human lung tissue explants were infected in an external, completely independent validation experiment with SARS-CoV-2 (red) at $1*10^6$ PFU and viral replication was measured after 0 h, 16 h, 24 h, 48 h and 72 h showing a comparable result as Figures 3A and B.

(B) Annotation of cell clusters from scSeq data of human alveolar (2905 cells in 6 samples) and bronchial organoids (23473 cells in 4 samples), respectively.

(C) Marker gene expression for major cell types in (B).

(D) Expression of *ACE2*, *KREMEN*, *ASGR1*, *TMPRSS2*, *FURIN*, *CD147/BSG* and *NRP1* in alveolar and bronchial organoids.

(E) Quantification of major cell types in (B), *ACE2*-positive and SARS-CoV-2-positive cells.

(F) ACE2 immunostaining (green) in human bronchial wt organoids (left panel), $ACE2^+$ bronchial organoids (middle panel) and alveolar wildtype organoids (right panel). Cell nuclei are visualized by DAPI stain (blue), scale bars 20 µm.

Data are represented as mean ± SEM, * $p < 0.01$.

Figure S4

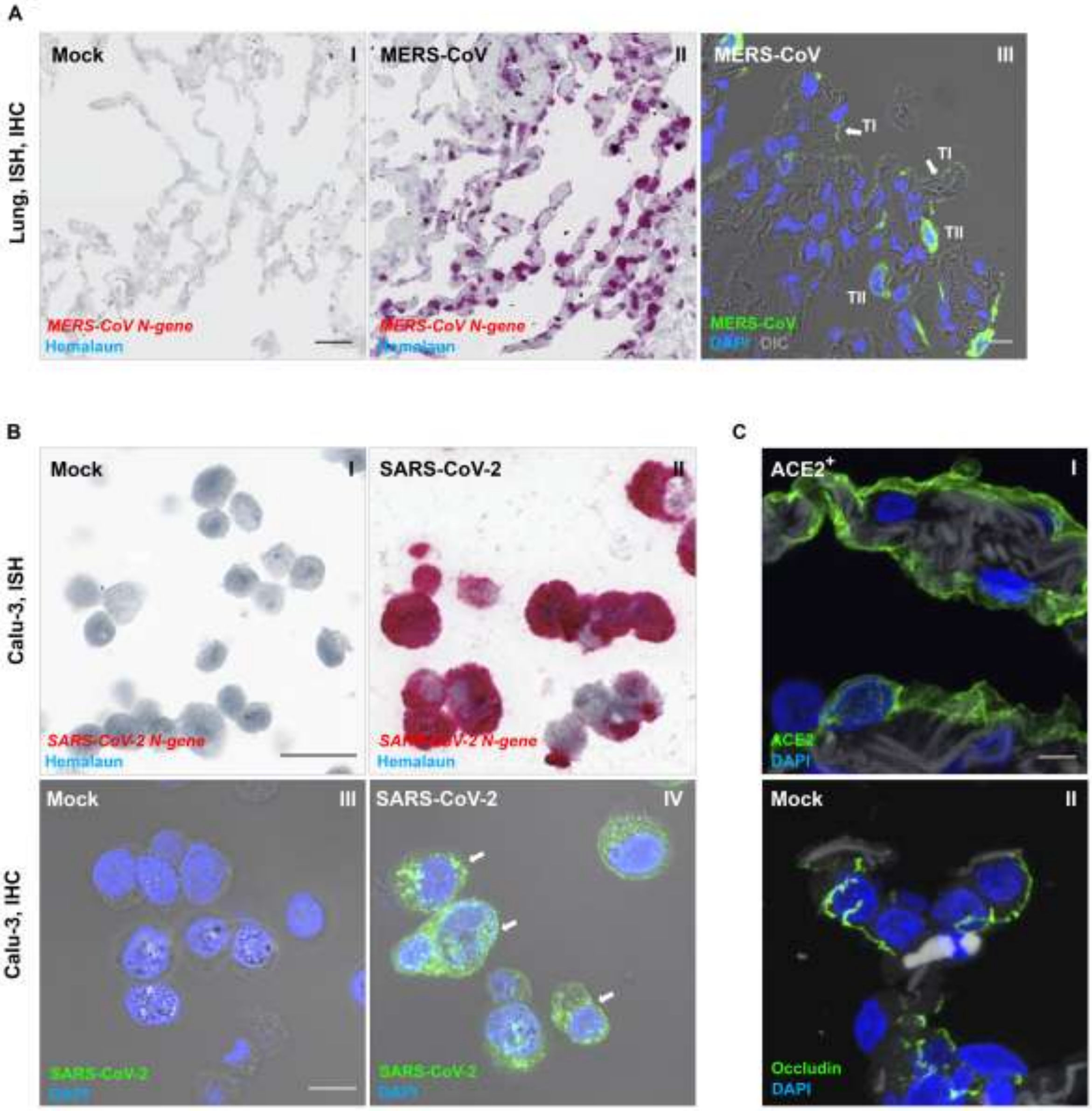

Figure S4. Abundant detection of MERS-CoV infected human lungs; positive and negative control stainings for *in situ* hybridization and immunohistochemistry in Calu-3, expression of ACE2 after adenoviral transduction, and occludin control staining

(A) *In situ* hybridization for *N-gene* of MERS-CoV (red) in mock-infected (panel I) and MERS-CoV infected ($1*10^6$ PFU, panel II) human lung tissue showing the strong permissiveness for the virus. Cell nuclei are visualized by Hemalaun stain (blue). Immunostaining of MERS-CoV (green) infected ($1*10^6$ PFU, panel III) human lung tissue confirming the results from panel II.

Arrows indicate AT1 (TI), AT2 cells are marked by TII. Cell nuclei are visualized by DAPI stain (blue), scale bar 10 µm.

(B) *In situ* hybridization for *N-gene* of SARS-CoV-2 (red) in mock-infected (panel I) and SARS-CoV-2 infected (MOI 1, panel II) in paraffin embedded Calu-3 cells. Cell nuclei are visualized by Hemalaun stain (blue). Immunostaining of SARS-CoV-2 (green) in mock-infected (panel III) and SARS-CoV-2 infected (MOI 1, panel IV) Calu-3 cells. Arrows indicate SARS-CoV-2-positive cells. Cell nuclei are visualized by DAPI stain (blue), scale bar 10 µm.

(C) Immunostaining of ACE2 (panel I, green) in lung explants transduced recombinant adenovirus expressing human ACE2. Panel II showed expression of occludin (green) in control lung explants. Cell nuclei are visualized by DAPI stain (blue), scale bar 5 µm.

Figure S5

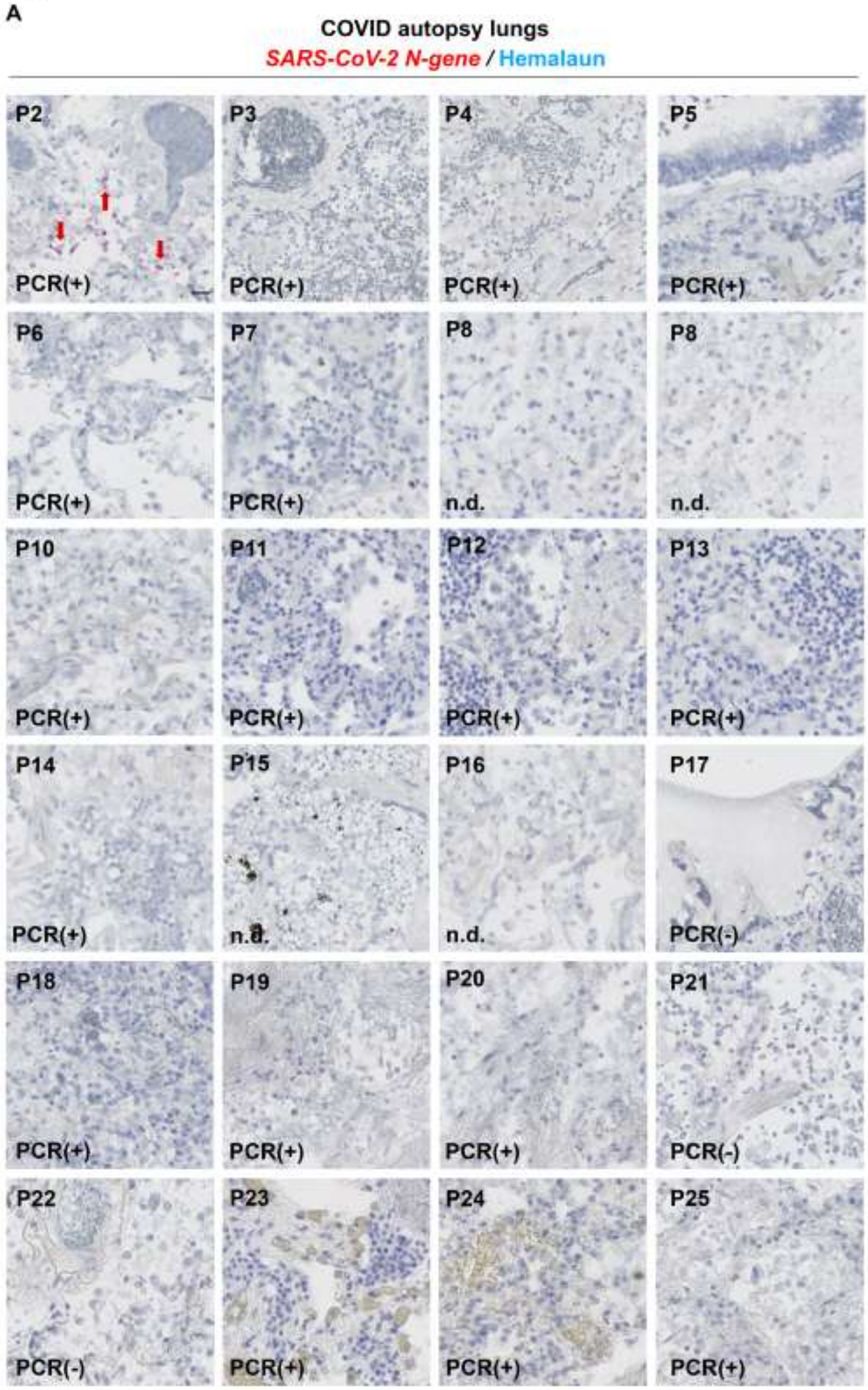
A
COVID autopsy lungs
SARS-CoV-2 N-gene / Hemalaun
P2
PCR(+)
P3
PCR(+)
P4
PCR(+)
P5
PCR(+)
P6
PCR(+)
P7
PCR(+)
P8
n.d.
P8
n.d.
P10
PCR(+)
P11
PCR(+)
P12
PCR(+)
P13
PCR(+)
P14
PCR(+)
P15
n.d.
P16
n.d.
P17
PCR(-)
P18
PCR(+)
P19
PCR(+)
P20
PCR(+)
P21
PCR(-)
P22
PCR(-)
P23
PCR(+)
P24
PCR(+)
P25
PCR(+)

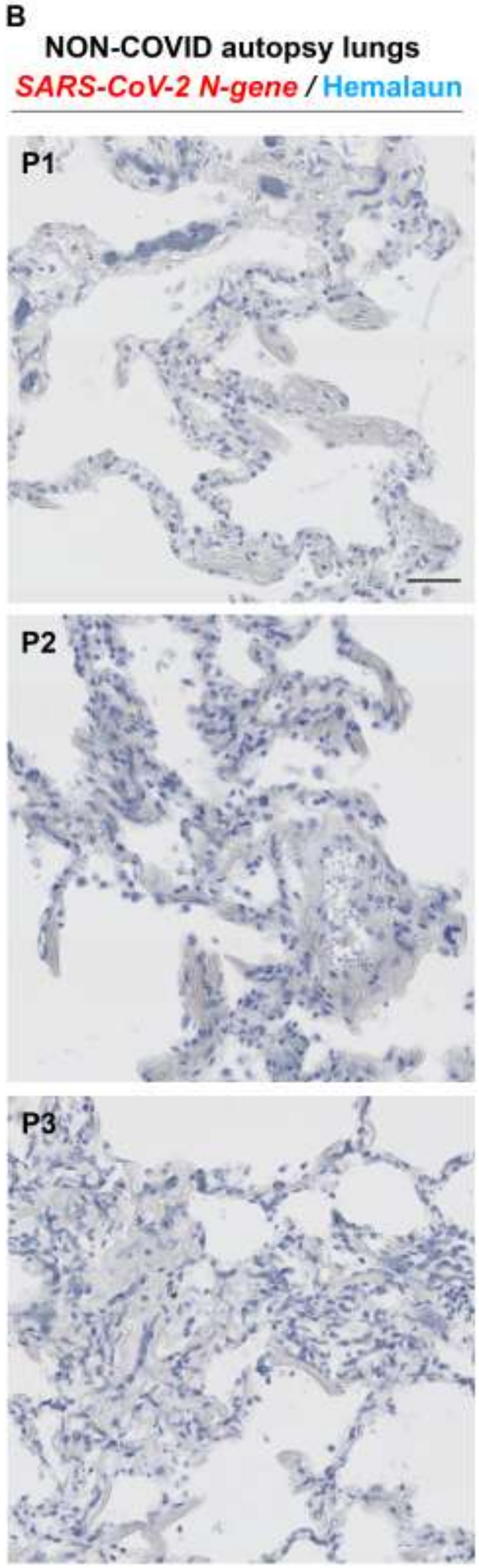
B
NON-COVID autopsy lungs
SARS-CoV-2 N-gene / Hemalaun
P1
P2
P3

C

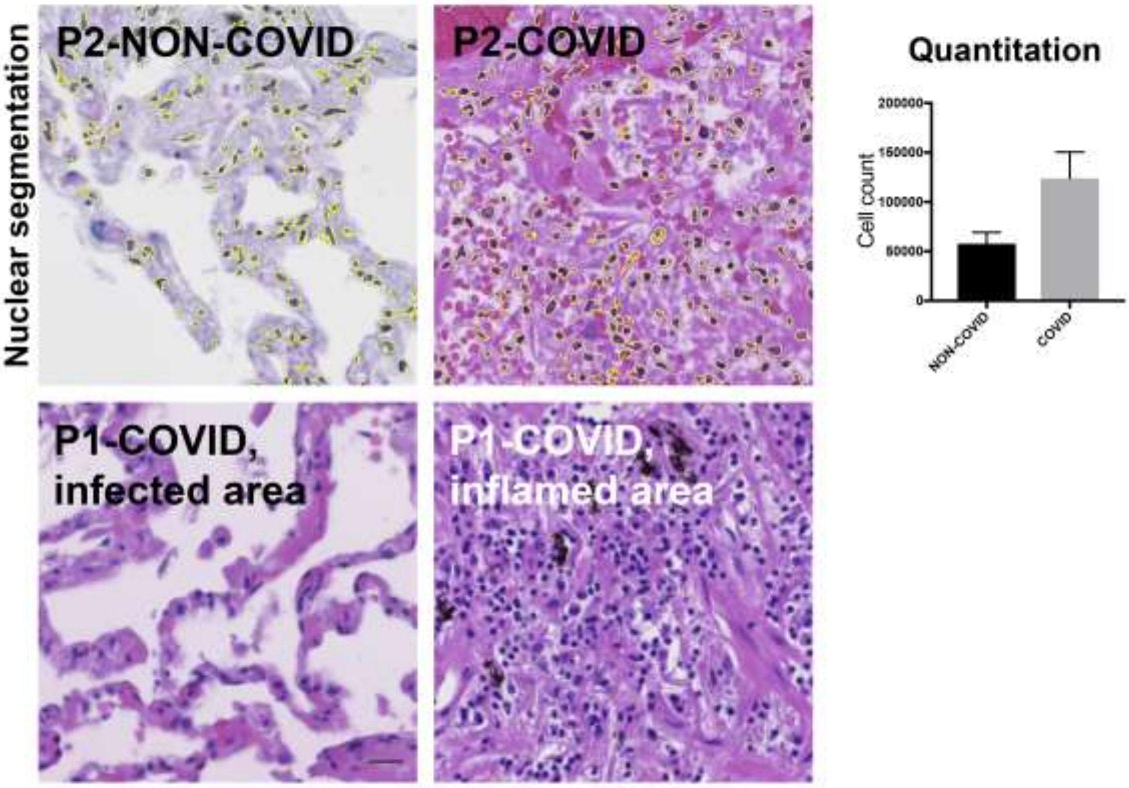
Nuclear segmentation
P2-NON-COVID
P2-COVID
P1-COVID,
infected area
P1-COVID,
inflamed area
Quantitation
Cell count
200000
150000
100000
50000
0
NON-COVID
COVID

D

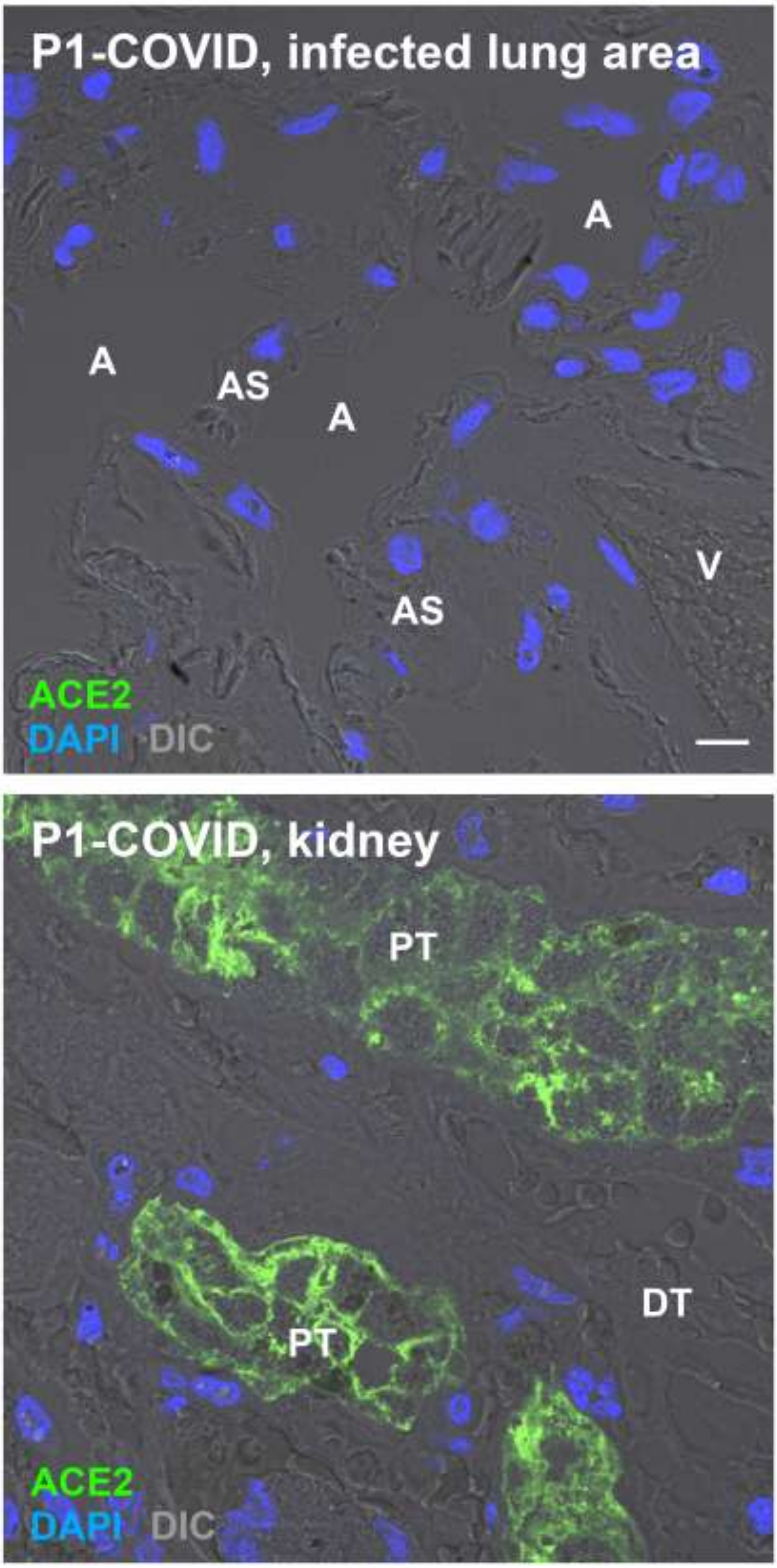
P1-COVID, infected lung area
A
A
AS
A
AS
V
ACE2
DAPI DIC
P1-COVID, kidney
PT
DT
PT
ACE2
DAPI DIC

Figure S5. ***In situ*** **hybridization of SARS-CoV-2 COVID-19 autopsy lungs and control tissue**

(A) *In situ* hybridization for *N-gene* of SARS-CoV-2 (red) in COVID-19 autopsy lungs (Patients P2 – P25 of which 17 were virus-positive qPCR). Positive virus detection could just be found in 1 further case (P2), all others remained negative. Red arrows indicate SARS-CoV-2-positive cells in P2. Cell nuclei are visualized by Hemalaun stain (blue), scale bar 20 µm.

(B) *In situ* hybridization of SARS-CoV-2 in NON-COVID autopsy control lungs. Cell nuclei are visualized by Hemalaun stain (blue), scale bar 50 µm.

(C) Nuclear segmentation of HE-stained autopsy lungs (4x NON-COVID / 4x COVID) in the upper panels demonstrate that a strong increase of inflammatory cells. The determined nucleus borders are illustrated by yellow lines in the top row. The lower left panel shows a SARS-CoV-2-infected area of COVID-19 case patient 1 (P1) as depicted in Figure 5A and B with conspicuous absent adjacent inflammation whereas other regions show strong inflammation as recognized (lower right panel). Cell nuclei are visualized by Hemalaun stain (blue), scale bar 20 µm.

(D) Immunohistochemistry of ACE2 in the infected areas of the autopsy lung samples compared to kidney tissue was analyzed by spectral microscopy and linear unmixing. The upper panel shows the infected lung area (AS: alveolar septs; A: alveolar space, V: Vessel) of COVID-19 patient 1 (P1) demonstrated in Figure 5A and B. The lower panel shows kidney tissue from the same patient. ACE2 (green) was stained on for both tissues on the same slide. Whereas kidney tissue shows again high expression of ACE2 (green) in proximal tubules (PT) and no staining in distal tubules (DT), no staining for ACE2 could be revealed in the lung tissue, even by doubling of the laser power for fluorescence excitation. Cell nuclei are visualized by DAPI stain (blue), scale bar 10 µm.

Figure S6

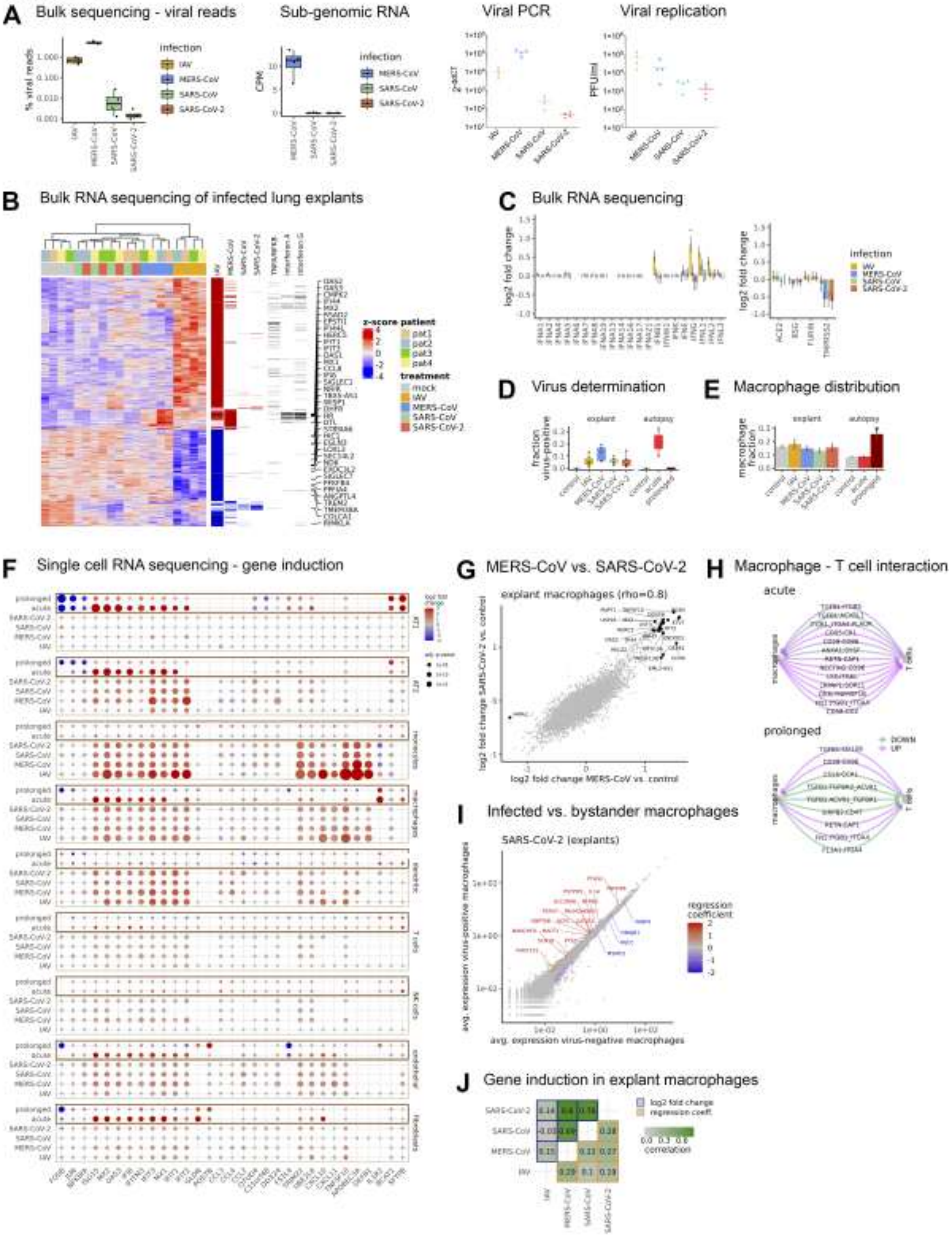
A
Bulk sequencing - viral reads
% viral reads
infection
IAV
MERS-CoV
SARS-CoV
SARS-CoV-2
Sub-genomic RNA
CPM
Viral PCR
2^-ddCT
Viral replication
PFU/ml
B
Bulk RNA sequencing of infected lung explants
z-score patient
pat1
pat2
pat3
pat4
treatment
mock
IAV
MERS-CoV
SARS-CoV
SARS-CoV-2
C
Bulk RNA sequencing
log2 fold change
ACE2
BSG
FURIN
TMPRSS2
D
Virus determination
fraction virus-positive
explant
autopsy
control
acute
prolonged
E
Macrophage distribution
macrophage fraction
F
Single cell RNA sequencing - gene induction
prolonged
acute
AT1
AT2
monocytes
macrophages
dendritic
T cells
NK cells
endothelial
fibroblasts
G
MERS-CoV vs. SARS-CoV-2
explant macrophages (rho=0.8)
log2 fold change SARS-CoV-2 vs. control
log2 fold change MERS-CoV vs. control
H
Macrophage - T cell interaction
acute
prolonged
macrophages
T cells
DOWN
UP
I
Infected vs. bystander macrophages
SARS-CoV-2 (explants)
avg. expression virus-positive macrophages
avg. expression virus-negative macrophages
regression coefficient
J
Gene induction in explant macrophages
log2 fold change
regression coeff.
correlation
0.14
0.6
0.76
-0.03
0.69
0.28
0.25
0.21
0.27
0.29
0.1
0.28
IAV
MERS-CoV
SARS-CoV
SARS-CoV-2

Figure S6. Bulk and single-cell RNA sequencing indicates low permissiveness for SARS-CoV-2 and uptake

(A) Human lung tissue explants were infected with IAV H3N2 (orange), MERS-CoV (blue), SARS-CoV (green) and SARS-CoV-2 (red) at $1*10^6$ PFU. Shown are percentage of reads mapping to the respective viral genome, subgenomic RNAs as counts per million (CPM), as well as viral reads in qPCR and viral replication in PFU units.

(B) Heatmap of regularized log-transformed expression values after removing inter-patient variability for 2969 genes differentially expressed in any of the 4 comparisons (adj. p-value < 0.05). Up- and down-regulated genes are indicated by red or blue bars, genes within selected Hallmark pathways are indicated by black bars, and top 20 up- or down-regulated genes are highlighted.

(C) Estimated log2 fold changes for interferon pathway genes (left) or *ACE2*, *BSG*, *FURIN* and *TMPRSS2* (right) in human lung tissue infected with IAV H3N2 (orange), MERS-CoV (blue), SARS-CoV (green) and SARS-CoV-2 (red). Error bars are standard errors computed by DESeq2, * adj. p-value < 0.05.

(D) Fraction of virus-positive cells in single-cell and single-nucleus data from lung tissue explants or COVID-19 autopsy material.

(E) Proportion of macrophages in single-cell and single-nucleus data from lung tissue explants or COVID-19 autopsy material. P-value from mixed-effects binomial model. * p < 0.05.

(F) Dot plot of selected differentially expressed genes (adj. p-value < 0.05) in infected lung explants or COVID-19 autopsy data compared to the respective controls in major cell types of the human lung. Border marks autopsy samples.

(G) Scatter plot of log2 fold changes for SARS-CoV-2-infected lung explant macrophages or MERS-CoV-infected lung explant macrophages, compared against control. Top 15 genes (adj. p-value < 0.01) are highlighted, and Spearman correlation is indicated.

(H) Differential receptor-ligand signaling interactions specific to T cells and macrophages when comparing acute and prolonged autopsy samples against controls using scDiffCom.

(I) Scatter plot of average gene expression in virus-positive vs. virus-negative lung explant macrophages infected with SARS-CoV-2. Color scale indicates regression coefficient from cloglog regression, top 20 genes (adj. p-value < 0.01) are highlighted.

(J) Correlations of log2 fold changes (blue) from comparing infected lung explant macrophages against control macrophages, and of regression coefficients (orange) when comparing virus-positive against virus-negative explant macrophages. Color scale and text indicate Spearman correlation.

Figure S7

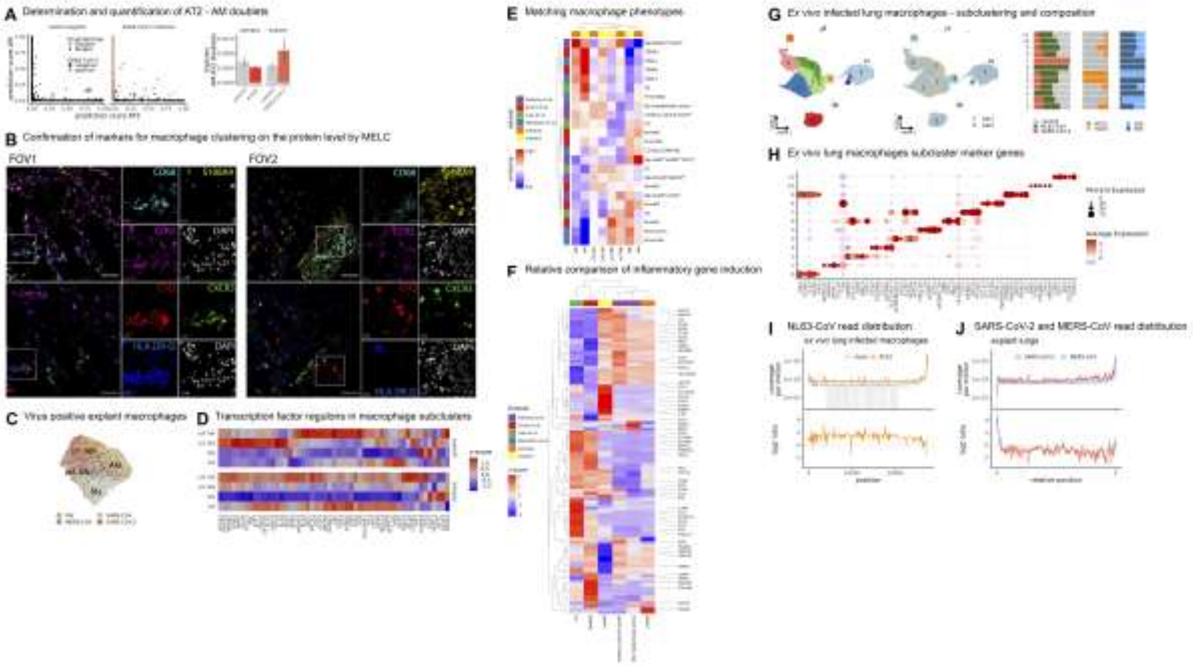

Figure S7. Single-cell RNA sequencing reveals inflammatory induction of alveolar macrophages (AM) by SARS-CoV-2

(A) Putative AM-AT2 doublets in lung explant scSeq data. Left panel: scatter plot of cell type prediction scores using the Human Lung Cell Atlas reference together with doublet prediction scores from DoubletFinder. Color indicates presence of SARS-CoV-2 RNA. Right panel: quantification of doublets with prediction scores for AM and AT2 identify both > 0.05.

(B) Immunofluorescence images depicting CD68 (cyan), S100A9 (yellow), CCR2 (magenta), DAPI (white), C1Q (red), CXCR3 (green) and HLA-DR/DP/DQ (blue), in two representative fields of view (FOV) acquired in post-mortem lung tissue of a SARS-CoV2-infected donor (11 days of disease duration). Scale bar 100 µm. Single channels are shown only for a region of interest in each FOV marked as a white square. Scale bar 20 µm.

(C) Virus-positive cells in macrophages from lung tissue explants infected with IAV H3N2 (yellow), SARS-CoV (green), MERS-CoV (blue), and SARS-CoV-2 (red).

(D) Transcription factor regulons from a SCENIC analysis in lung explant and autopsy macrophages. Top 20 regulons with the highest specificity scores are included, AUC values are averaged across cells and z-scores are computed for explant and autopsy data separately.

(E) Comparison of average gene expression profiles in macrophage subclusters from explant and autopsy data with macrophage subtypes described in Delorey et al., Grant et al., Liao et al., and Wendisch et al. [25-28].

(F) Heatmap of average gene expression profiles for top 100 variable genes among selected macrophage subclusters from (E).

(G) Clustering of isolated lung macrophages infected *ex vivo* with SARS-CoV-2 or NL63-CoV, under mock treatment or ACE2 overexpression, and for two timepoints and two donors. Left panel: UMAP embedding colored by cluster identity; middle panel: UMAP colored by donor identity; right panel: subcluster composition for the different experimental conditions.

(H) Top 5 marker genes for the clusters in (C).

(I) Distribution of reads mapping to the NL63-CoV genome for *ex vivo* infected AM under mock treatment or ACE2 overexpression. Top panel: coverage per million mapped reads smoothed with 10 nt moving average. Shaded area indicates mean ± SEM across replicates. Bottom panel: log2 ratio between ACE2 and mock conditions.

(J) Distribution of reads mapping to the viral genome for lung explants infected with MERS-CoV or SARS-CoV-2, respectively. Top panel: smoothed coverage per million mapped reads smoothed with 10 nt moving average, genomic position is scaled to a common coordinate system. Shaded area indicates mean ± SEM across replicates. Bottom panel: log2 ratio between MERS-CoV and SARS-CoV-2 read coverage.

Table S1. Meta-data of donors for human lung tissue used for ACE2 Determination and virus infection

Lung tissue used for infection was free of tumor and taken from unaffected areas which were histologically considered as “normal”. Concurrent medication from groups AT1-receptor antagonists and ACE-inhibitors were marked bold. Neither for ACE2 protein expression (Figures 1 and 2) nor for SARS-CoV or SARS-CoV-2 replication (Figure 3) could any correlation be drawn to age, sex, co-morbidities, or concurrent medication.

Abbreviations: AC: adenocarcinoma; AI: autoimmune; ASS: acetylsalicyl acid (aspirin); BC: bronchial carcinoma; HLP: hyperlipoproteinemia; HL: hyperlipidemia; IDDM: insulin dependent diabetes mellitus; NSCLC: non-small cell lung cancer; RA: rheumatoid arthritis.

sex	**age**	**smoking**	**primary diagnosis**	**secondary diagnoses**	**concurrent medication**	**pfu load (SARS-CoV-2)**	**log fold change (SARS-CoV-2)**	**ID**
Figure 1E, S1D (Lungs)								
m	70	n.d.	NSCLC, squamous cell carcinoma	Atrioventricular block Hypertensive & coronary heart disease Chronic kidney failure Hyperparathyroidism Hypercholesterolaemia IDDM II Sigmoid colon cancer	Allopurinol Aspirin Atorvastatin **Candesartan** Cholecalciferol Forxiga Jardiance Metformin Pantoprazole Plavix	n.a.	n.a.	P1
f	82	no	Squamous cell carcinoma	none	none	n.a.	n.a.	P2
m	70	yes	NSCLC	Hypacusis *post* meningitis Lung emphysema	Aspirin Atorvastatin	n.a.	n.a.	P3

				Peripheral artery disease				
m	76	yes	Squamous cell carcinoma	Aortic aneurysm Arterial hypertension Coronary heart disease IDDM II Myocardial infarction Renal arterial stenosis	Aspirin Atorvastatin Bisoprolol **Ramipril**	n.a.	n.a.	P4
m	36	yes	AC	Bechterew's disease	Palexia Lorazepam	n.a.	n.a.	P5
f	68	no	healthy control	Cerebrovascular stroke		n.a.	n.a.	P6
f	68	no	healthy control	Cerebrovascular stroke		n.a.	n.a.	P7
Figure 1D, F and G								
m	73	no	AC	Carotid stenosis Colon cancer Hypertension	Aspirin Atozet Cholecalciferol **Ramipril**	n.a.	n.a.	P1
f	81	no	NSCLC	Arterial hypertension Atrio-ventricular block Depression Dissociative aphonia Hyperlipidemia IDDM II Trans-ischemic attacks	Aspirin Insulin **Losartan** Metformin Metoprolol Nadroparin Pantoprazole Torasemid	n.a.	n.a.	P2
f	60	no	Large cell carcinoma	Asthma Chronic gastritis Hypothyroidism	Cholecalciferol L-thyroxine Pantoprazole	n.a.	n.a.	P3
-	-	-	-	**See P1 in Figure 1E**	-	-	-	P4
f	82	yes	AC	Anaemia Aortic valve stenosis	Atorvastatin **Candesartan**	n.a.	n.a.	P5

				Arrhythmia Arterial hypertension Asthma Cardiomyopathy Cataract Depression Lipometabolic disorder Polyneuropathy	Cholecalciferol Citalopram Diltiazem Ferrosanol Flecainid Pantoprazole Pregabalin Symbicort Zopiclon			
m	69	yes	NSCLC	Arterial hypertension Myocardial infarction Stroke Vocal cord carcinoma	Aspirin Amlodipin Bisoprolol Fumarat **Ramipril** Simvastatin	n.a.	n.a.	P6
Figure 3A and C, Figure 6								
m	61	yes	BC	Hypertension Gut cancer	**Candesartan** Nebivolol	1x10^6	0.8 log	P1
m	59	yes	BC	Hyperlipoproteinemia Hypertension	Atorvastatin Lercanidipin **Ramipril**	1x10^6	1.1 log	P2
f	57	no	BC	Breast cancer Asthma	Beclometason Formoterol L-thyroxine	1x10^6	2.0 log	P3
f	67	yes	BC	AI-thyreoiditis Hypertension Rheumatoid arthritis	Aspirin Bisoprolol L-thyroxine Torasemide	1x10^6	1.7 log	P4
f	70	yes	BC	Atherosclercosis Atrial fibrillation Breast cancer Gastritis Hyperlipidemia Hypertension Myocardial infarction	Atorvastatin Clopidogrel Diltiazem Gabapentin Pantozol Ramipril Torasemide	1x10^6	0.7 log	P5

Figure 1B, C, 3B and Figure 7, S7								
-	-	-	-	**See P2 in Figure 1D**	-	30x10^6	n.d.	P1
m	79	yes	NSCLC	Arterial hypertension Benign prostate Hypermetabolic thyroid Hyperplasia	Brimica **Candesartan** Amlodipin Finasterid Tamsulosin Pantoprazol	30x10^6	0.4 log	P2
m	85	no	Squamous cell carcinoma	Arterial hypertension Chronic kidney failure	Hydrochlorothiazide Losartan Torasemide	30x10^6	0.2 log	P3
w	67	yes	NSCLC	COPD Coronary heart disease Osteoporosis	Aspirin Pantoprazol **Ramipril** Salbutamol Umeclidinium~Vilanterol	30x10^6	1.0 log	P4
w	42	yes	AC	Hyperthyreodism	Folic acid Pantoprazol Olanzapin Thiamazol	30x10^6	0.5 log	P5
Figure S3								
m	63	no	Osteo-sarcoma	Arterial hypertension Metastatic osteosarcoma	Rosuvastatin Pregabalin Tamsulosin	1x10^6	2.3 log	P1
m	69	no	AC	Cardiomyopathy Cardiac insufficiency Chronic kidney failure Mitral regurgitation Parox. atrial tachycardia Pulmonary hypertonia	Bisoprolol Entresto Eplerenon Glyceroltrinitrat Rivaroxaban Simvastatin Torasemide	1x10^6	1.8 log	P2

w	61	no	AC	COPD Uveitis	Aciclovir Prednisolon	1x10^6	2.0 log	P3
Figure 4, S4								
w	64	yes	AC	COPD	-	1x10^6	n.a.	P1
m	84	no	AC	Descending colon carcinoma IDDM	Actrapid Sitagliptin Insulin Simvastatin Valsartan	1x10^6	n.a.	P2
w	74	no	AC	Arterial hypertension Breast cancer Coronary heart disease Hyperthyroidism	ASS Atorvastatin Metoprolol **Ramipril**	1x10^6	n.a.	P3

Abbreviations: AC: adenocarcinoma; AI: autoimmune; ASS: acetylsalicyl acid (aspirin); BC: bronchial carcinoma; COPD: chronic obstructive pulmonary disease; IDDM: insulin dependent diabetes mellitus; NSCLC: non-small cell lung cancer; RA: rheumatoid arthritis.

Table S2. Meta-data of donors for COVID-19 autopsy lungs used for single-nucleus sequencing

Abbreviations: ALS: amyotrophic lateral sclerosis; ARDS: acute respiratory distress syndrome; CHD: coronary heart disease; COPD: chronic obstructive pulmonary disease; LAE: left atrial enlargement; LV: left ventricular; MOF: multi-organ failure.

sex	age	smoking history	Cause of death	secondary diagnoses	PMI	Disease duration	Category	ID
Figures 1, S2, 6, S6, 7 and S7								
m	76	yes	COVID-19	Atherosclerosis Diffuse alveolar damage Hypertension Ischemic cardiomyopathy Sepsis	30h	14d	acute	P1
m	81	no	COVID-19	Aortic aneurysm	3d	11d	acute	P2

				Atrial fibrillation Cardiac amyloidosis Diabetes mellitus Hypertension LV failure Sepsis				
m	62	yes	COVID-19	ARDS CHD Cardiac failure Diffuse pulmonary bleeding Hypertension Obesity Pulmonary edema Sepsis	10h	19d	prolonged	P3
f	68	no	COVID-19	COPD Focal abscessing pneumonia Hypertension Obesity Pulmonary superinfection Septic shock	16h	34d	prolonged	P4
m	75	no	COVID-19	ARDS Hypertension Obesity Obstructive sleep apnoea Septic MOF	6h	10weeks	prolonged	P5
m	77	no	COVID-19	Acute liver and renal failure Cholangitis Gastric bleeding Polyneuropathy Sepsis	38h	≥12weeks	prolonged	P6
m	77	no	Pulmonary embolism	ALS, LAE	1d	-	control	P7

f	68	no	Cerebro-vascular stroke	-	1d	-	control	P8

Abbreviations: ALS: Aayotrophic lateral sclerosis; ARDS: acute respiratory distress syndrome; CHD: coronary heart disease; COPD: chronic obstructive pulmonary disease; LAE: left atrial enlargement; LV: left ventricular; MOF: multi-organ failure.

Table S3. Cell type marker genes in single-cell RNA sequencing data of human lung tissue

Marker genes for the clusters shown in Fig. 1B. p_val and p_val_adj are unadjusted and adjusted (Bonferroni) p-values, pct.1 and pct.2 are fraction of cells expressing a gene in the respective cluster and all other cells, avg_logFC is the log fold change for the average expression between a cluster and all other cells.

Table S4. Differential expression analysis of Bulk RNA sequencing data

Differential expression analysis of bulk RNA sequencing data for human lung tissue infected with IAV, MERS-CoV, SARS-CoV and SARS-CoV-2. Sheets 1-4 contain DESeq2 output (padj < 0.05; with "normal" shrinkage) when comparing each virus against the control.

Table S5. Differential expression analysis of human lung single-cell and single-nucleus RNA sequencing data

Differential expression analysis of single-cell and single-nucleus RNA sequencing data for human lung explants infected with IAV, MERS-CoV, SARS-CoV or SARS-CoV-2, or autopsy material from acute and prolonged COVID-19 cases. Sheets 1 contains DESeq2 output using a pseudobulk strategy to compare gene expression in each cell type for infected samples against control explant samples. Sheet 2 contains DESeq2 output when comparing COVID-19 autopsy data against control autopsy data.

Table S6. Differential expression analysis of human lung single-cell RNA sequencing data

Differential expression analysis using cloglog regression of single-cell RNA sequencing data for virus-positive against virus-negative lung explant macrophages.

Table S7. Differential expression analysis of *ex vivo* alveolar macrophages single-cell RNA sequencing data

Differential expression analysis of single-cell RNA sequencing data for human lung macrophages infected with SARS-CoV-2 or NL63-CoV. Sheet 1 contains DESeq2 output for infected samples against control samples under mock treatment, sheet 2 contains similar DESeq2 output under ACE2 overexpression. Sheet 3 contains results of a pathway enrichment analysis with tmod.

References

1. Hocke AC, Becher A, Knepper J, Peter A, Holland G, Tonnies M, Bauer TT, Schneider P, Neudecker J, Muth D, Wendtner CM, Ruckert JC, Drosten C, Gruber AD, Laue M, Suttorp N, Hippenstiel S, Wolff T. Emerging human middle East respiratory syndrome coronavirus causes widespread infection and alveolar damage in human lungs. *Am J Respir Crit Care Med* 2013: 188(7): 882-886.
2. Szymanski KV, Toennies M, Becher A, Fatykhova D, N'Guessan PD, Gutbier B, Klauschen F, Neuschaefer-Rube F, Schneider P, Rueckert J, Neudecker J, Bauer TT, Dalhoff K, Dromann D, Gruber AD, Kershaw O, Temmesfeld-Wollbrueck B, Suttorp N, Hippenstiel S, Hocke AC. Streptococcus pneumoniae-induced regulation of cyclooxygenase-2 in human lung tissue. *Eur Respir J* 2012: 40(6): 1458-1467.
3. Weinheimer VK, Becher A, Tonnies M, Holland G, Knepper J, Bauer TT, Schneider P, Neudecker J, Ruckert JC, Szymanski K, Temmesfeld-Wollbrueck B, Gruber AD, Bannert N, Suttorp N, Hippenstiel S, Wolff T, Hocke AC. Influenza A viruses target type II pneumocytes in the human lung. *J Infect Dis* 2012: 206(11): 1685-1694.
4. Berg J, Zscheppang K, Fatykhova D, Tonnies M, Bauer TT, Schneider P, Neudecker J, Ruckert JC, Eggeling S, Schimek M, Gruber AD, Suttorp N, Hippenstiel S, Hocke AC. Tyk2 as a target for immune regulation in human viral/bacterial pneumonia. *Eur Respir J* 2017: 50(1).
5. Sachs N, Papaspyropoulos A, Zomer-van Ommen DD, Heo I, Bottinger L, Klay D, Weeber F, Huelsz-Prince G, Iakobachvili N, Amatngalim GD, de Ligt J, van Hoeck A, Proost N, Viveen MC, Lyubimova A, Teeven L, Derakhshan S, Korving J, Begthel H, Dekkers JF, Kumawat K, Ramos E, van Oosterhout MF, Offerhaus GJ, Wiener DJ, Olimpio EP, Dijkstra KK, Smit EF, van der Linden M, Jaksani S, van de Ven M, Jonkers J, Rios AC, Voest EE, van Moorsel CH, van der Ent CK, Cuppen E, van Oudenaarden A, Coenjaerts FE, Meyaard L, Bont LJ, Peters PJ, Tans SJ, van Zon JS, Boj SF, Vries RG, Beekman JM, Clevers H. Long-term expanding human airway organoids for disease modeling. *EMBO J* 2019: 38(4).
6. Hoffmann K, Berger H, Kulbe H, Thillainadarasan S, Mollenkopf HJ, Zemojtel T, Taube E, Darb-Esfahani S, Mangler M, Sehouli J, Chekerov R, Braicu EI, Meyer TF, Kessler M. Stable expansion of high-grade serous ovarian cancer organoids requires a low-Wnt environment. *EMBO J* 2020: 39(6): e104013.
7. Drost J, Artegiani B, Clevers H. The Generation of Organoids for Studying Wnt Signaling. *Methods Mol Biol* 2016: 1481: 141-159.
8. Hoffmann M, Kleine-Weber H, Schroeder S, Kruger N, Herrler T, Erichsen S, Schiergens TS, Herrler G, Wu NH, Nitsche A, Muller MA, Drosten C, Pohlmann S. SARS-CoV-2 Cell Entry Depends on ACE2 and TMPRSS2 and Is Blocked by a Clinically Proven Protease Inhibitor. *Cell* 2020: 181(2): 271-280 e278.
9. Pfefferle S, Krahling V, Ditt V, Grywna K, Muhlberger E, Drosten C. Reverse genetic characterization of the natural genomic deletion in SARS-Coronavirus strain Frankfurt-1 open reading frame 7b reveals an attenuating function of the 7b protein in-vitro and in-vivo. *Virol J* 2009: 6: 131.
10. Muth D, Meyer B, Niemeyer D, Schroeder S, Osterrieder N, Muller MA, Drosten C. Transgene expression in the genome of Middle East respiratory syndrome coronavirus based on a novel reverse genetics system utilizing Red-mediated recombination cloning. *J Gen Virol* 2017: 98(10): 2461-2469.

11. Kurth F, Roennefarth M, Thibeault C, Corman VM, Muller-Redetzky H, Mittermaier M, Ruwwe-Glosenkamp C, Heim KM, Krannich A, Zvorc S, Schmidt S, Kretzler L, Dang-Heine C, Rose M, Hummel M, Hocke A, Hubner RH, Opitz B, Mall MA, Rohmel J, Landmesser U, Pieske B, Knauss S, Endres M, Spranger J, Mockenhaupt FP, Tacke F, Treskatsch S, Angermair S, Siegmund B, Spies C, Weber-Carstens S, Eckardt KU, Schurmann D, Uhrig A, Stegemann MS, Zoller T, Drosten C, Suttorp N, Witzenrath M, Hippenstiel S, von Kalle C, Sander LE. Studying the pathophysiology of coronavirus disease 2019: a protocol for the Berlin prospective COVID-19 patient cohort (Pa-COVID-19). *Infection* 2020: 48(4): 619-626.

12. Corman VM, Muller MA, Costabel U, Timm J, Binger T, Meyer B, Kreher P, Lattwein E, Eschbach-Bludau M, Nitsche A, Bleicker T, Landt O, Schweiger B, Drexler JF, Osterhaus AD, Haagmans BL, Dittmer U, Bonin F, Wolff T, Drosten C. Assays for laboratory confirmation of novel human coronavirus (hCoV-EMC) infections. *Euro Surveill* 2012: 17(49).

13. Nitsche A, Schweiger B, Ellerbrok H, Niedrig M, Pauli G. SARS coronavirus detection. *Emerg Infect Dis* 2004: 10(7): 1300-1303.

14. Livak KJ, Schmittgen TD. Analysis of relative gene expression data using real-time quantitative PCR and the 2(-Delta Delta C(T)) Method. *Methods* 2001: 25(4): 402-408.

15. Kim D, Lee JY, Yang JS, Kim JW, Kim VN, Chang H. The Architecture of SARS-CoV-2 Transcriptome. *Cell* 2020: 181(4): 914-921 e910.

16. Tosti L, Hang Y, Debnath O, Tiesmeyer S, Trefzer T, Steiger K, Ten FW, Lukassen S, Ballke S, Kuhl AA, Spieckermann S, Bottino R, Ishaque N, Weichert W, Kim SK, Eils R, Conrad C. Single nucleus and in situ RNA sequencing reveals cell topographies in the human pancreas. *Gastroenterology* 2020.

17. Fleming SJ, Marioni JC, Babadi M. CellBender remove-background: a deep generative model for unsupervised removal of background noise from scRNA-seq datasets. *bioRxiv* 2019: 791699.

18. Wolock SL, Lopez R, Klein AM. Scrublet: Computational Identification of Cell Doublets in Single-Cell Transcriptomic Data. *Cell Syst* 2019: 8(4): 281-291 e289.

19. McGinnis CS, Murrow LM, Gartner ZJ. DoubletFinder: Doublet Detection in Single-Cell RNA Sequencing Data Using Artificial Nearest Neighbors. *Cell Syst* 2019: 8(4): 329-337 e324.

20. Travaglini KJ, Nabhan AN, Penland L, Sinha R, Gillich A, Sit RV, Chang S, Conley SD, Mori Y, Seita J, Berry GJ, Shrager JB, Metzger RJ, Kuo CS, Neff N, Weissman IL, Quake SR, Krasnow MA. A molecular cell atlas of the human lung from single-cell RNA sequencing. *Nature* 2020: 587(7835): 619-625.

21. Love MI, Huber W, Anders S. Moderated estimation of fold change and dispersion for RNA-seq data with DESeq2. *Genome Biol* 2014: 15(12): 550.

22. Zyla J, Marczyk M, Domaszewska T, Kaufmann SHE, Polanska J, Weiner J. Gene set enrichment for reproducible science: comparison of CERNO and eight other algorithms. *Bioinformatics* 2019: 35(24): 5146-5154.

23. Bost P, Giladi A, Liu Y, Bendjelal Y, Xu G, David E, Blecher-Gonen R, Cohen M, Medaglia C, Li H, Deczkowska A, Zhang S, Schwikowski B, Zhang Z, Amit I. Host-Viral Infection Maps Reveal Signatures of Severe COVID-19 Patients. *Cell* 2020: 181(7): 1475-1488 e1412.

24. Lagger C, Ursu E, Equey A, Avelar RA, Pisco AO, Tacutu R, de Magalhães JP. scAgeCom: a murine atlas of age-related changes in intercellular communication inferred with the package scDiffCom. *bioRxiv* 2021: 2021.2008.2013.456238.

25. Delorey TM, Ziegler CGK, Heimberg G, Normand R, Yang Y, Segerstolpe A, Abbondanza D, Fleming SJ, Subramanian A, Montoro DT, Jagadeesh KA, Dey KK, Sen P, Slyper M, Pita-Juarez YH, Phillips D, Biermann J, Bloom-Ackermann Z, Barkas N, Ganna A, Gomez J, Melms JC, Katsyv I, Normandin E, Naderi P, Popov YV, Raju SS, Niezen S, Tsai LT, Siddle KJ, Sud M, Tran VM, Vellarikkal SK, Wang Y, Amir-Zilberstein L, Atri DS, Beechem J, Brook OR, Chen J, Divakar P, Dorceus P, Engreitz JM, Essene A, Fitzgerald DM, Fropf R, Gazal S, Gould J, Grzyb J, Harvey T, Hecht J, Hether T, Jane-Valbuena J, Leney-Greene M, Ma H, McCabe C, McLoughlin DE, Miller EM, Muus C, Niemi M, Padera R, Pan L, Pant D, Pe'er C, Pfiffner-Borges J, Pinto CJ, Plaisted J, Reeves J, Ross M, Rudy M, Rueckert EH, Siciliano M, Sturm A, Todres E, Waghray A, Warren S, Zhang S, Zollinger DR, Cosimi L, Gupta RM, Hacohen N, Hibshoosh H, Hide W, Price AL, Rajagopal J, Tata PR, Riedel S, Szabo G, Tickle TL, Ellinor PT, Hung D, Sabeti PC, Novak R, Rogers R, Ingber DE, Jiang ZG, Juric D, Babadi M, Farhi SL, Izar B,

Stone JR, Vlachos IS, Solomon IH, Ashenberg O, Porter CBM, Li B, Shalek AK, Villani AC, Rozenblatt-Rosen O, Regev A. COVID-19 tissue atlases reveal SARS-CoV-2 pathology and cellular targets. *Nature* 2021: 595(7865): 107-113.

26. Wendisch D, Dietrich O, Mari T, von Stillfried S, Ibarra IL, Mittermaier M, Mache C, Chua RL, Knoll R, Timm S, Brumhard S, Krammer T, Zauber H, Hiller AL, Pascual-Reguant A, Mothes R, Bulow RD, Schulze J, Leipold AM, Djudjaj S, Erhard F, Geffers R, Pott F, Kazmierski J, Radke J, Pergantis P, Bassler K, Conrad C, Aschenbrenner AC, Sawitzki B, Landthaler M, Wyler E, Horst D, Deutsche C-OI, Hippenstiel S, Hocke A, Heppner FL, Uhrig A, Garcia C, Machleidt F, Herold S, Elezkurtaj S, Thibeault C, Witzenrath M, Cochain C, Suttorp N, Drosten C, Goffinet C, Kurth F, Schultze JL, Radbruch H, Ochs M, Eils R, Muller-Redetzky H, Hauser AE, Luecken MD, Theis FJ, Conrad C, Wolff T, Boor P, Selbach M, Saliba AE, Sander LE. SARS-CoV-2 infection triggers profibrotic macrophage responses and lung fibrosis. *Cell* 2021: 184(26): 6243-6261 e6227.

27. Grant RA, Morales-Nebreda L, Markov NS, Swaminathan S, Querrey M, Guzman ER, Abbott DA, Donnelly HK, Donayre A, Goldberg IA, Klug ZM, Borkowski N, Lu Z, Kihshen H, Politanska Y, Sichizya L, Kang M, Shilatifard A, Qi C, Lomasney JW, Argento AC, Kruser JM, Malsin ES, Pickens CO, Smith SB, Walter JM, Pawlowski AE, Schneider D, Nannapaneni P, Abdala-Valencia H, Bharat A, Gottardi CJ, Budinger GRS, Misharin AV, Singer BD, Wunderink RG, Investigators NSS. Circuits between infected macrophages and T cells in SARS-CoV-2 pneumonia. *Nature* 2021: 590(7847): 635-641.

28. Liao M, Liu Y, Yuan J, Wen Y, Xu G, Zhao J, Cheng L, Li J, Wang X, Wang F, Liu L, Amit I, Zhang S, Zhang Z. Single-cell landscape of bronchoalveolar immune cells in patients with COVID-19. *Nat Med* 2020: 26(6): 842-844.

29. Peter A, Fatykhova D, Kershaw O, Gruber AD, Rueckert J, Neudecker J, Toennies M, Bauer TT, Schneider P, Schimek M, Eggeling S, Suttorp N, Hocke AC, Hippenstiel S. Localization and pneumococcal alteration of junction proteins in the human alveolar-capillary compartment. *Histochem Cell Biol* 2017: 147(6): 707-719.

30. Osterrieder N, Bertzbach LD, Dietert K, Abdelgawad A, Vladimirova D, Kunec D, Hoffmann D, Beer M, Gruber AD, Trimpert J. Age-Dependent Progression of SARS-CoV-2 Infection in Syrian Hamsters. *Viruses* 2020: 12(7).

31. Legland D, Arganda-Carreras I, Andrey P. MorphoLibJ: integrated library and plugins for mathematical morphology with ImageJ. *Bioinformatics* 2016: 32(22): 3532-3534.

32. Contesso G, Mouriesse H. [Anatomopathologic consensus for defining the prognostic factors of breast cancers]. *Pathol Biol (Paris)* 1990: 38(8): 834-835.

33. Holzwarth K, Kohler R, Philipsen L, Tokoyoda K, Ladyhina V, Wahlby C, Niesner RA, Hauser AE. Multiplexed fluorescence microscopy reveals heterogeneity among stromal cells in mouse bone marrow sections. *Cytometry A* 2018: 93(9): 876-888.

34. Pascual-Reguant A, Kohler R, Mothes R, Bauherr S, Hernandez DC, Uecker R, Holzwarth K, Kotsch K, Seidl M, Philipsen L, Muller W, Romagnani C, Niesner R, Hauser AE. Multiplexed histology analyses for the phenotypic and spatial characterization of human innate lymphoid cells. *Nat Commun* 2021: 12(1): 1737.

35. Schubert W, Bonnekoh B, Pommer AJ, Philipsen L, Bockelmann R, Malykh Y, Gollnick H, Friedenberger M, Bode M, Dress AW. Analyzing proteome topology and function by automated multidimensional fluorescence microscopy. *Nat Biotechnol* 2006: 24(10): 1270-1278.

36. Pertuz S, Puig D, Garcia MA, Fusiello A. Generation of all-in-focus images by noise-robust selective fusion of limited depth-of-field images. *IEEE Trans Image Process* 2013: 22(3): 1242-1251.